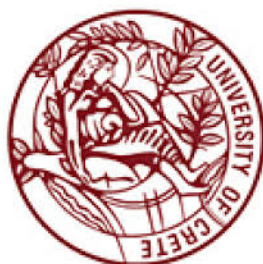# DYNAMICS AND KINETICS IN SOFT MATTER SYSTEMS:

EFFECT OF LIGHT AND SHEAR IN CONCENTRATED POLYDIENE SOLUTIONS AND COLLOIDAL SUSPENSIONS

ANDREAS PAMVOUXOGLOU

DOCTORAL DISSERTATION

UNIVERSITY OF CRETE

DEPARTMENT OF MATERIALS SCIENCE AND TECHNOLOGY

HERAKLION   2014

i

Committee:

George Fytas[1,2,3] (Supervisor)

George Petekidis[1,2] (Supervisor)

Benoit Loppinet[1] (Supervisor)

Dimitris Vlassopoulos[1,2]

Stergios Pispas[4]

Ulrich Jonas[5]

Apostolos Rizos[6]

1. Institute of Electronic and Laser (IESL), Foundation for Research and Technology (FORTH), Heraklion, Crete, Greece
2. Department of Materials Science and Technology, University of Crete, Heraklion, Crete, Greece
3. Max Planck Institute for Polymer research, Mainz, Germany
4. National Hellenic Research Foundation (NHRF), Athens, Greece
5. Department of Chemistry – Biology, University of Siegen, Siegen, Germany
6. Department of Chemistry, University of Crete, Heraklion, Crete, Greece

Acknowledgements

First I would like to thank my supervisors Prof. George Petekidis, Dr. Benoit Loppinet and Prof. George Fytas for never-ending encouragement, support and interest in my work. I would like also to thank Dr. Stergios Pispas and Prof. Kohji Ohno for the samples used during my thesis.

I cannot forget the assistance which was provided to me from Dr. Dennis Kurzbach and his supervisor Prof. Dariush Hinderberger for the EPR experiment performed in Mainz Institute (MPIP, Germany).

It has been a great opportunity to have scientific discussions with fellow scientists in the laboratory. Over the years great discussions have been had with the people from the Polymer lab and especially with Dr. Andreas Poulos, Dr. Nick Koumakis and Dr. Manos Anyfantakis. I would like to thank especially Manos for the infinite discussions and his kind hospitality I had during my trip in Mainz. Without him many things would be impossible.

I would like also to truly thank the members of the committee for their evaluation of this thesis and especially those who are travelling to Crete in order to attend my defense.

As a final note I would like to thank my parents Niko and Nassia, my brother Alexandro and my sister Georgia for million reasons that are not necessary to mention here. Finally I would like to thank Olga for the infinite support in my effort to complete this thesis and for many other reasons.

Abstract

This thesis is concerned with the study of two projects related with mechanical and optical forces in soft matter systems. In the first part, the effect of light irradiation in polydiene solutions was examined. Specifically the characterization of the light-induced fibers and the effect of light in more complicated polydiene-based systems were studied. We show that upon irradiation radicals are formed, which crosslink the material, creating fibers. We also revealed that by changing the sample's parameter (temperature, solvent and microstructure) we affect the kinetics of pattern formation. More specifically multiblock (diblock, triblock) copolymers in selective solvents, open new routes to patterning due to rich phase diagram.

In the second part, we report on the structure and dynamics in suspensions of soft colloidal core-shell particles up to the glass regime. Particles with different chain molecular weight grafted on a hard core were used to investigate the effect of softness. In the liquid regime due to the high refractive index mismatch between particle-solvent, we used 3D Dynamic Light Scattering. We demonstrate that the dynamics of the system can be interpreted with permeable spherical particles model, varying only one parameter, the hydrodynamic penetration depth x. In the glass regime the system is strongly non-ergodic and ages with time. Using Multispeckle Dynamic Light scattering (MSDLS) we found a glass-crystal re-entrant transition, independent of particle's softness. The effect of softness upon shear was also investigated through rheology. A series of linear (dynamic frequency sweep), nonlinear (dynamic strain sweep, LAOS, flow curves) and transient (start-up) experiments were performed, demonstrating clearly the effect of softness.

Περίληψη

Η παρούσα διδακτορική διατριβή πραγματεύεται την μελέτη δύο διαφορετικών θεμάτων που σχετίζονται με μηχανικές και οπτικές δυνάμεις στην περιοχή της χαλαρής ύλης. Στο πρώτο μέρος αναφέρεται η επίδραση της ακτινοβολίας του φωτός σε διαλύματα πολυδιενίων. Ειδικότερα ο χαρακτηρισμός των ινών που δημιουργούνται υπό την επίδραση του φωτός καθώς και η επίδραση του φωτός σε πολύπλοκα συστήματα που περιέχουν πολυδιένεια. Παρατηρήσαμε ότι υπό την επίδραση ακτινοβολίας δημιουργούνται ελεύθερες ρίζες, οι οποίες δικτυώνουν το υλικό δημιουργώντας ίνες. Επίσης παρατηρήσαμε ότι αλλάζοντας διάφορες παραμέτρους του δείγματος (θερμοκρασία, διαλύτης και μικροδομή) επηρεάζεται η κινητική της δομής που δημιουργείται. Πιο συγκεκριμένα πολυσυσταδικά συμπολυμερή (δυσυσταδικά, τρισυσταδικά) σε επιλεγμένους διαλύτες, μας δίνουν νέες κατευθύνσεις στην δημιουργία δομών, γεγονός που οφείλεται στο πολύπλοκο διάγραμμα φάσης.

Στο δεύτερο μέρος, αναφερόμαστε στις δομικές και δυναμικές ιδιότητες αιωρημάτων μαλακών κολλοειδών διασπορών τύπου πυρήνα-κελύφους (core-shell) σε συγκεντρώσεις μέχρι την υαλώδη περιοχή (glass regime). Στην παρούσα μελέτη χρησιμοποιήθηκαν σωματίδια με διαφορετικό μοριακό βάρος αλυσίδας χημικά δεμένης με των πυρήνα, προκειμένου να μελετηθεί η επίδραση της «μαλακότητας» (softness). Στην υγρή περιοχή λόγω της μεγάλης διαφοράς του δείκτη διάθλασης μεταξύ σωματιδίου-διαλύτη, χρησιμοποιήθηκε η τεχνική 3D δυναμική σκέδαση φωτός, για την εξάλειψη της πολλαπλής σκέδασης. Αποδείξαμε ότι η δυναμική των συστημάτων συγκλίνει με την θεωρία πορωδών σφαιρών, μεταβάλλοντας μια παράμετρο, το υδροδυναμικό βάθος διείσδυσης. Στην υαλώδη περιοχή τα συστήματα παρουσιάζουν μη εργοδική συμπεριφορά και η δυναμική αλλάζει με τη πάροδο του χρόνου. Στην περίπτωση αυτή τα συστήματα χαρακτηρίστηκαν με φασματοσκοπία συσχέτισης φωτονίων πολλαπλών περιοχών συμφωνίας (MSDLS) όπου ανεξαρτήτως της μαλακότητας των σωματιδίων παρατηρήθηκε μετάβαση από την υαλώδη στην κρυσταλλική περιοχή. Επιπρόσθετα, μέσω ρεολογικών μετρήσεων, μελετήθηκε η επίδραση της μαλακότητας υπό διάτμηση. Πιο συγκεκριμένα διεξήχθησαν πειράματα στην γραμμική (dynamic frequency sweep), στην μη-γραμμική

(dynamic strain sweep, LAOS, flow curves) και «μεταβατικά» (transient) (start-up) πειράματα.

Contents

Foreword

In the past three decades, soft condensed matter has emerged as a field of research dealing with the structure and properties relation of a wide range of materials, mostly based on polymers and colloids. Those materials are characterized by broad distribution of length and time scales and relatively weak interparticle forces (soft). As a result they are often very responsive to the application of external fields. This is especially true for the application of mechanical fields, with very rich viscoelastic behavior, and complex nonlinear responses, but also in some cases for the application of optical fields. This Ph.D. thesis consist of two parts dealing with two aspects of such systems. In the first part (chapter 1-2), I present a study of characterizing and understanding the anomalous response of polydienes solutions to laser light irradiation. In the second part (chapter 3-5), I report on the structure, dynamics and rheology of a specific type of soft colloids, i.e. core-shell particles. The thesis is organized as follow:

In chapter 1, a clear demonstration of the characterization of the written material upon irradiation will be discussed. Using different spectroscopic (EPR, Raman) and mechanical (swelling, rheology) techniques, the stable and insoluble pattern formed was characterized, proposing a plausible scenario for the mechanism.

In chapter 2 we will report results concerning the kinetics of the refractive index change followed by red laser irradiation. By changing sample's parameters (temperature, solvent, microstructure) we will try to elucidate the possible coupling between light-matter and to explore/extend the effect to more complicated systems.

In chapter 3 we present experiments of colloidal core-shell particles in the liquid regime. 3DDLS was applied due to strong multiple scattering. Structure and dynamics of the three systems were compared with hard and permeable sphere theory. It was found that by changing a single parameter, the hydrodynamic penetration depth x, we were able to describe well the dynamics of the system as a function of the volume fraction for all systems studied.

In chapter 4 we present extended ageing measurements in the glass regime, where the systems have non-stationary dynamics with time. By monitoring the evolution of the slowest relaxation time through MSDLS, a re-entrant glass-crystal transition was observed.

In the final chapter (chapter 5), we studied the effect of particle's softness on the rheological properties. We focused on measuring and understanding the linear and nonlinear properties of the soft core-shell particles glasses. The rheology and yielding behavior has been examined by linear (dynamic frequency sweep), nonlinear (dynamic strain sweep, LAOS, flow curves) and transient (start-up) experiments and relaxation.

Part I

Laser-induced pattern formation in polydiene solutions

Soft matter and optical fields

The response of soft matter systems to optical field has recently attracted renewed attention as it was realized that the ease to respond to external field of such systems make them good potential material for nonlinear optic response, when the response lead to a local change of the refractive index. The defining property for Soft Matter Nonlinear optics will be a change in the refractive index upon light irradiation related to some mesoscopic degree of freedom of the system, for example concentration in mixtures, orientation in liquid crystals. The precise coupling between the optical field and the material refractive index can be many. Three main categories can be mentioned optical forces (mostly radiation pressure), thermal effects (as a result of light absorption by the material) and photo-induced chemistry (photorefractive material).

The present work is about a special case of optical responses of polydienes solutions submitted to laser light irradiation that was discovered ~15 years ago in the lab. Upon laser irradiation a light-polymer coupling was revealed, that eventually led to the formation of material pattern and optical waveguides. Despite similarities with other systems where the light-material coupling and the pattern formation mechanisms are well elucidated, the basic coupling between the light field and the material cannot simply be explained in the polydienes solutions.

In the next part I quickly review the cases of refractive index-optical field coupling commonly used in what has recently emerged as soft matter nonlinear optics and show some similarities with the effects we observe, yet none can fully explain the coupling between light-matter.

Optical forces in solution

A dielectric particle suspended in a dielectric medium is irradiated by light is sub-mitted to a force. The optical forces can eventually lead to the particle being trapped in the optical fields. The phenomenon has been developed into the widely used tech-niques of laser trapping. For particles much smaller than the wavelength of the light (Rayleigh regime), the photon pressure exerted on a Rayleigh particle is expressed as fol-lows:

$$F = \frac{1}{2}\alpha \nabla \vec{E}^2 + \alpha \frac{\partial}{\partial t (\vec{E} \times \vec{B})}$$

(1)

where $\vec{E}$ and $\vec{B}$ are the electric field strength and magnetic flux density, respectively, a is the polarizability of the particle. The first term in equation 1 is an electrostatic force acting on the dipole in the inhomogeneous electric field, and is called the gradient force (F_{grad}):

$$F = -\frac{n}{2}\alpha \nabla E^2 = -\frac{n_0^3 r^3}{2}\left(\frac{m^2 - 1}{m^2 - 2}\right)\nabla E^2$$

(2)

where r is the radius of the particles m the ratio of refractive index of the particle n to the one of the dispersing medium n_0 . For particles of index of refraction larger than that of the continuous medium ($n > n_0$), the polarizability is positive, resulting in a gradient force which attracts the particle to the high intensity region (focus). The second term, derived from the change in the direction of the Poynting vector, is called scattering force (F_{scat}), which pushes particles along the beam direction is given by F_{scat}

$$F_{scat} = \frac{I_0}{c}\frac{128\pi^5 r^6}{3\lambda^4}\left(\frac{m^2 - 1}{m^2 - 2}\right)^2 n_0$$

(3)

where $I_0 = E^2$ is the laser intensity. Note that for a particle to be optically trapped, F_{grad} has to be larger than F_{scat}, as depicted schematically in figure 1.
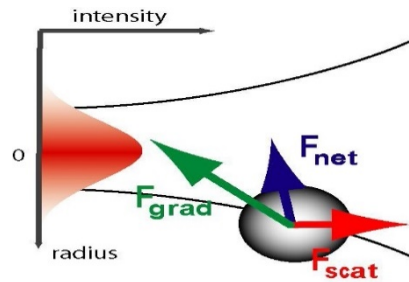
Figure 1: Schematic showing the optical forces acting on a particle suspended in a dielectric liquid.

Isotropic particles are subjected to forces induced by light intensity gradients, thus moving in the region with higher or lower intensity, depending on the refractive difference between particles n_p and solvent n_o *(Boyd 2008).* If $n_p > n_o$, the gradient force moves the particles within the higher intensity region of the laser beam (Man, Fardad et al. 2013). This electrostrictive forces results in a self-focusing due to refractive index change which can eventually lead to optical wave guiding. This was first realized and investigated by Ashkin and coworkers (Ashkin, Dziedzic et al. 1982).

Recently, Conti et al. (Conti, Ruocco et al. 2005) proposed a novel general approach to stationary self-focusing, linking the electrostrictive nonlocal response of soft matter with the spatial distribution of the particles. By developing a theory they were able to predict propagation of two-dimensional waveguides. By fixing the input waist and the incident power in order to find the appearance of a soliton, they could directly measure the fractal dimension of the aggregates.

In a recent publication Nemirovsky et al. (Nemirovski, Szameit et al. 2011) showed that radiation pressure can induce flow in nano-suspensions via drag forces, even with small particles' size (~ 1.6 nm diameter). The light-induced flux of nanoparticles leads to regions with higher concentration which changes the refractive index and focuses (or defocuses) the optical beam, creating a pattern. When the contrast is positive ($n_p > n_{fluid}$), narrow straight-line filments formed in the beam, which are thin and intense, due to self-focusing. When the contrast is negative ($n_p < n_{fluid}$) the beam undergoes self-defocusing, creating filaments that are wider and less intense.

A recent development is the mixing of particles that have refractive index larger and lower than the dispersing solvent. Man et al. (Man, Fardad et al. 2013) introduced that by

judiciously mixing particles both positive and negative polarizabillities they can fine tune the nonlinear response. They specifically observe robust propagation and enhanced transmition of an optical beam when traversing Teflon (PTFE) suspension (negative contrast) as a compared to that in a typical positive contrast (Polystyrene (PS)) suspension. This light penetration in the strong scattering solution was attributed to the interplay between optical forces and self-activated transparency effect in absence of thermal effects. They experimentally observe an enhancement of the transmission in pure PTFE suspensions, a case of self-induced transparency (figure 2).
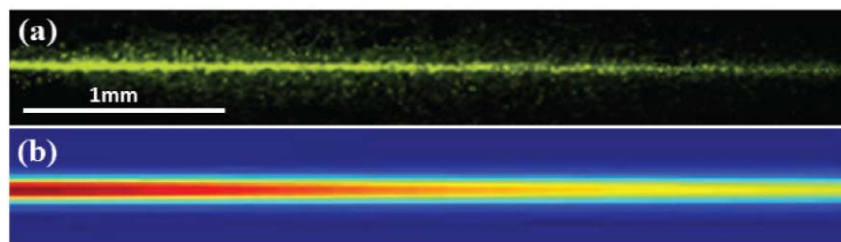
Figure 2: Self-trapped beam propagation through a PTFE nanosuspension: (a) experimental results, (b) theoretical model

Recently Sugiyama and co-workers (Sugiyama, Yuyama et al. 2012) reported spatiotemporally control of nucleation and growth by laser trapping in a number of different systems studied. In their work they first report the laser trapping of individual nanoparticles by using a specific laser trapping system. A 1064 nm near-infrared (NIR) continuous-wave (CW) laser was used as a trapping system with adjustable power. The samples used were poly(N-isopropylacrylamide) together with a pyrene label in order to monitor morphological and fluorescent changes. The sample solutions were transparent in the visible-region, but overtone bands from OH vibrations in solvents like water and alcohols, absorb at 1064 nm. Moreover at the same work, authors studied the laser trapping in linear polymers and they reported that can be trapped and associated with each other. The volume found to be increased resulting in a stronger gradient force and eventually the whole focal volume is filled by the polymers. This is the first study which reports laser trapping due to scattering forces only.

Light-induced thermal effect

Another way to locally affect refractive index by application of light is due to creation of temperature gradient. Molecules drift along temperature gradients, an effect called the Soret effect, or thermodiffusion. In an isotropic binary fluid mixture with nonuniform concentration and temperature, the mass flow j_m of the one component contains both a contribution stemming from the concentration and one from the temperature gradient:

$$\vec{j_m} = -\rho D \nabla c - \rho c(1-c)D_T \nabla T \tag{5}$$

where D is the collective diffusion coefficient, D_T the thermal diffusion coefficient, ρ the mass density, and c the concentration of the component. In a stationary state, $j_m = 0$ and the Soret coefficient S_T is given by the ratio of D_T to D. S_T can be positive or negative. In the first case, solute molecules move towards the cold region, and when $S_T < 0$, motion of the solute towards the hot region occurs.

Thermodiffusion (Soret) has recently been used to produce local spatial patterns in solutions. The possibilities offered by such an approach is illustrated by the example from Duhr et al. (Duhr and Braun 2006). The authors manipulate the DNA concentration by changing the temperature within the bulk solution. By increasing the temperature 2K due to absorption they created a pattern "DNA" using infrared laser scanning microscope. In an overall cooled chamber at 3°C, DNA accumulates towards the heated letters "DNA" (negative Soret coefficient), whereas at room temperature DNA is thermophobic (positive Soret coefficient) with DNA molecules to move to the colder regions. As a result, the local concentration of DNA molecules decreases and a spatial pattern consisting of lower-concentration letters is formed in the aqueous solution. The temperature pattern 'DNA' was written into the solution film with an infrared laser scanning microscope, as shown in figure 3:

9
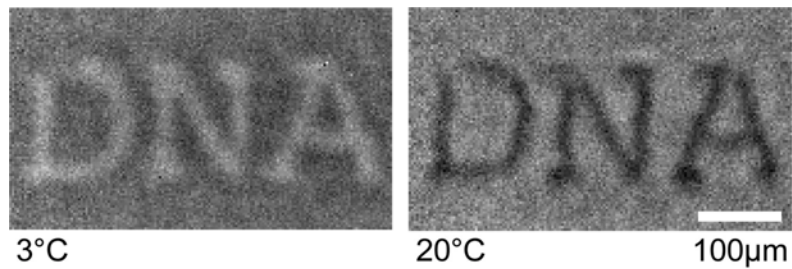
Figure 3: A thin water film is heated by 2K along the letters ''DNA'' with an infrared laser. For a cooled chamber at 3°C, fluorescently tagged DNA accumulates at the warm letters. However, at room temperature, DNA moves into the cold, showing reduced fluorescence.

Laser heating by a few Kelvin can generate arbitrary flow pattern of liquids, which can move and trap molecules down to nanometer scale. Another example of the use of microscopic temperature changes induced by laser irradiation is from Voit et al. (Voit, Krekhov et al. 2005, Voit, Krekhov et al. 2007), where the patterning arise from phase separation or mixing. The authors employed a focused laser beam of λ=515 nm to create patterns in a critical polymer blend of poly (dimethyl siloxane) / poly (ethyl methyl siloxane). The blend was transparent and addition of dye which absorbs at the laser wavelength was used to create optical heating. The patterns were formed in both the homogenous and the phase separated region, a few degrees above and below the critical temperature. A representative pattern demonstrated by these authors is shown in Figure 4:

Figure 4: The word 'Bayreuth' as written by repeatedly scanning the laser across the surface of the poly (dimethyl siloxane) / poly (ethyl methyl siloxane) critical polymer blend.

It is interesting to highlight than even in transparent medium temperature change can become relevant, if like here the systems is close to phase separation of mixing. A particularly impressive demonstration of how minute temperature changes induced by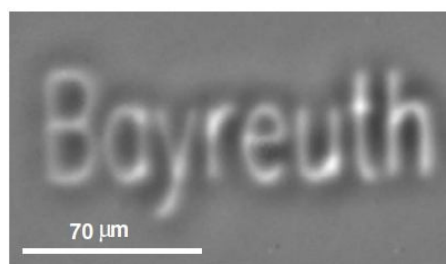 laser in transparent material can become relevant is given by Delville et al (Delville, Lalaude et al. 1994) reported on the phase separation and droplet nucleation induced by laser radiation (λ = 514 nm) in a quaternary mixture of water, n-dodecane, SDS and n-pentanol. This mixture, in the particular composition used, forms a micellar solution (water droplets in oil, with a diameter of 8 nm) at room temperature. The system is close to a demixing temperature (20 °C), such that a very small increase in micellar concentration induces a liquid-liquid phase separation towards a lower micellar concentration phase. The efficiency of the weakly focused laser beam as an osmotic piston for driving a phase separation in this liquid mixture was shown. The nucleation droplets created, are trapped (due to electrostriction) in the light beam owing to their high positive polarizability. The droplets act like spherical lenses and in turn self-focus the beam (Delville, Lalaude et al. 1999). The quench in composition in this case was confirmed to be due to thermodiffusion. The authors calculated the laser-induced temperature variation for the particular system, given a beam waist of 5 μm and a power of P = 100 mW, to be about $4.4*10^{-2}$ °C. This ΔT is enough to cause a concentration change of the order of 10^{-3} in the beam centre, explaining the laser induced phase separation by the Soret effect. The electrostrictive contribution was calculated to be one order of magnitude less than the thermo-diffusive contribution, due to the very small polarizability of the micelles.

Photorefractive polymers

Photochemistry is another way to affect locally the refractive index, through light induced chemical changes. In photorefractive materials, an exposure to light of appropriate wavelength could produce a permanent increase which will lead to an increase of the refractive index. The beam can be self-trapped along the irradiation axis (Kewitsch and Yariv 1996). Dorkenoo et al. (Dorkenoo, Crégut et al. 2002) investigated the condition of self-written propagation in bulk photopolymerizable materials. By varying the beam power, they

were able to tune the number of channel waveguides created. The authors also reported that the growth of the multi or single channel depends on the duration of the input light. The same group proposed an experimental and theoretical study on the optimization of self-written waveguide formation inside a photopolymerizable material (Dorkenoo, Gillot et al. 2004). In their work they discuss the effect of light intensity and the evolution of the refractive index upon irradiation. They end-up with a model which by calculating the V value, they were able to propagate a single or multimode waveguides on a few centimeters.

In a recent paper Jacobsen and coworkers (Jacobsen, Barvosa-Carter et al. 2007) proposed a micro-scale truss structure formed from self-propagating photopolymer waveguide. In contrast to existing lithographic techniques, this self-propagating effect enables the formation of three-dimensional open structures. By varying the angle of the incident beam they were able to control the geometry and the mechanical properties of the cellular structure (figure 5).
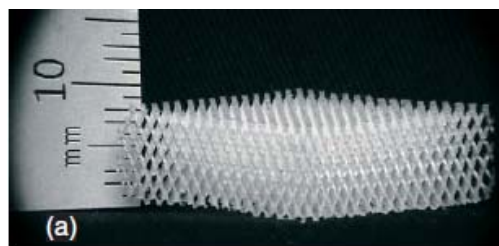
Figure 5: Open-cellular micro-truss structures formed from a 3D pattern of interconnected self-propagating polymer waveguides. The polymer micro-truss structure is 7.8 mm thick.

Light – Polydiene effect

An "anomalous" phenomenon of Soft Matter response by applying red laser was recently reported in polydiene solutions. Upon red laser irradiation, the initial Gaussian profile of the transmitted beam changed dramatically with time and eventually widens, forming a rich diffraction pattern. Simultaneously with the beam opening, a smooth trace of light at scattering angle of 90° was observed, which its intensity was increasing with time, as had been observed through a CCD camera. A string like structure were observed (Sigel, Fytas et al. 2002, Anyfantakis, Fytas et al. 2010).
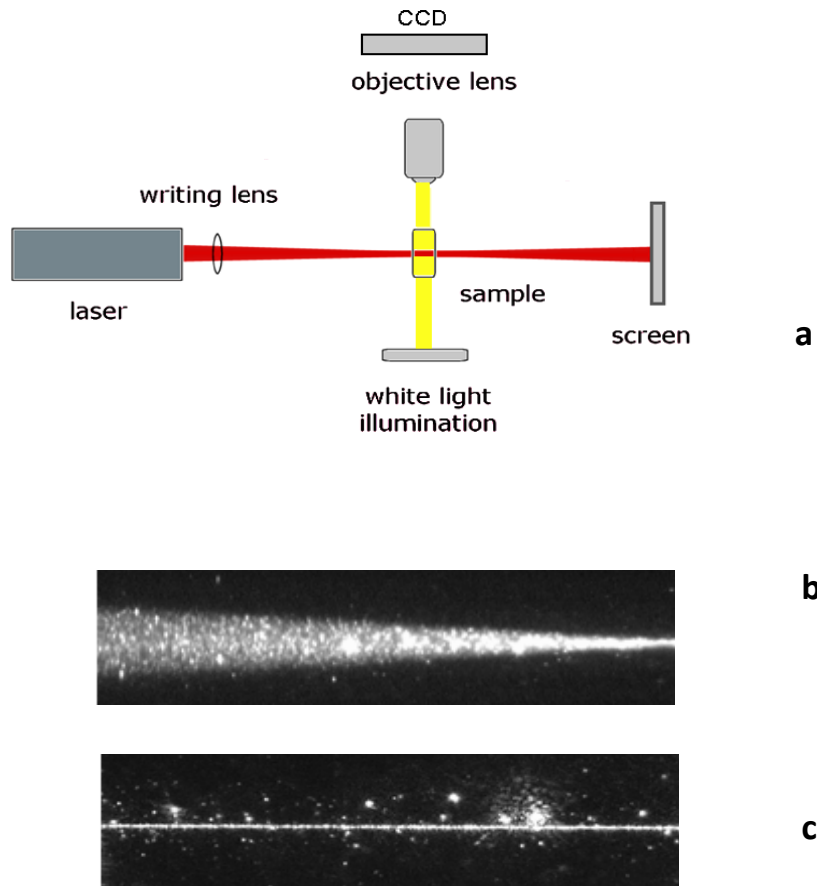
Figure 6 a: A schematic of the experimental setup for creating and simultaneously imaging the light-induced patterns. **b:**   Image of the scattered intensity at 90° **c:** Image of the increased scattered intensity as the phenomenon evolves.

A light-induced filament that is written along the propagation direction of the laser beam is optically detected due to the refractive index difference between the formed structure and the background solution. The diameter of the filament is approximately 10 µm, while its length is limited by the cell size (~ few mm). This effect was also utilized to write holographic gratings (Loppinet, Somma et al. 2005).
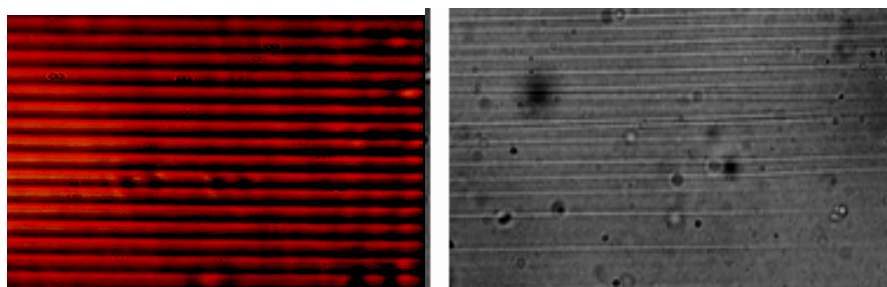
Figure 7: A spatial periodic pattern corresponding to the grating planes is recorded by a microscope/CCD camera system. To create the pattern, the main beam of a red (647 nm) laser was divided into two beams, which fully overlap in the sample forming the optical grating (left), or by focusing through a cylindrical lens to create 2D filament array.

In a later Letter from this group (Anyfantakis, Loppinet et al. 2008) we reported in detail the properties of the filaments formed, utilized by phase contrast microscopy experiments. Filament formation speeds up with increasing power and its growth rate Γ was found to exhibit a nearly linear increase with P. The study continued with the use of light sheet illumination led to formation of multifilament followed by using a cylindrical lens, which have similar behavior with the single ones.

A detailed study in the kinetics of the concentration optical nonlinearity in polydiene solutions were carried out (Anyfantakis, Loppinet et al. 2013). Phase contrast microscopy experiments allowed quantifying the concentration change upon laser irradiation. The growth of kinetics was studied by varying polymer molecular weight M, concentration, solvent and polymer microstructure.

In-depth study of the effect in good solvents were also established from Anyfantakis et al (Anyfantakis, Koniger et al. 2012) were they uncovered also the reverse effect. Depending on the solvent environment, macromolecules are either effectively attracted or repelled by visible laser light independently of the optical contrast. They showed a clear wavelength dependence on the kinetics. In particular they presented cases of pattern with refractive index lower that the average refractive index of the material, which is against an electrostrictive mechanism. Depending on the conditions (material and irradiation) light application can give rise to a large number of light propagation and material patterning effect.

Experimental Investigation of long time irradiation was also reported by Anyfantakis et al. (Anyfantakis, Fytas et al. 2010). The single fibril formation was found to not reach steady state over a long time, led to complex multi-fibril patterns at very long irradiation times. The reversibility of the laser-induced matter organization depends on the irradiation time; at time scales comparable to the inverse of the formation rate, the written structures can be redissolved in the solution whereas for long irradiation times insoluble patterns were observed.

The study of the unexpected light-matter interaction was studied in polydiene-containing diblock poly(Styrene-Isoprene) copolymers dispersed in two selective solvents of each block (Anyfantakis, Loppinet et al. 2012). In the transparent case were the sample was dispersed in hexane (good solvent for PI) forming micelles, copolymer-rich fibers were formed similar to the homopolymer solutions in the same solvent. In the presence of ethyl-acetate (good solvent for polystyrene) the sample is turbid and self-induced transparency was observed. They claimed that optical forces are not expected to be responsive at the intensities utilized. Moreover light-induced thermal effects are not expected in the non-absorbing dispersions, since thermal lensing was not observed.

Motivation and goals

The anomalous behavior of pattern formation in non-absorbing polydiene solutions upon red-laser irradiation, could open a new class of materials for soft-matter non-linear optics and optical manipulation. However, despite the clear experimental observations, the origin of the possible light-matter interactions has not yet been revealed. Even though there are similarities with optical, thermal and photorefractive materials, none of them are able to explain fully the effect we observed.

The scattering forces for optical "manipulation" in a semidilute polyisoprene solution in heptane is expected to be weak. Taking an average polymer blob size ~8 nm, polarizability $\alpha_{blob} = 5.77*10^{-36}$ Cm/V, the refractive index $n_o = 1.39$ and the squared electric field $E^2 = 3.68*10^{11}$ V^2/m^2, the gradient potential force calculated through:

$$U_{grad} = \frac{1}{2} n_o \alpha_{blob} E^2 \qquad (4)$$

gives $U_{grad} \sim 10^{-24}$ Joules, which is $K_B T/2700$ at room temperature. This energy is much lower than $K_B T$ and is not expected to disturb thermal equilibrium distribution.

In order to check for possible relation with thermophoresis, a solution of polyisoprene (M_w=1090 kg/mole) in heptane was prepared at concentration of 10% wt. The calculated Soret coefficient is S_T = 0.143 K^{-1}. The fact that S_T is positive mans that the polymer move to the colder regions i.e. The local concentration in polyisoprene in the irradiated volume is expected to decrease , which is the opposite from what we observe through phase contrast microscopy.

In photorefractive polymers the key for polymerization is either specific compounds that are attached in the polymer and absorb at specific wavelengths or the polymer itself absorbs at that specific wavelength. Polyisoprene (or polybutadiene) absorb at much lower wavelength such as UV (Golub and Stephens 1967, Adam, Lacoste et al. 1991, dos Santos, Suarez et al. 2005) or stronger radiations like γ-rays (Golub 1958). They can absorb through a photochemical reaction in the visible region by adding nitroso- compounds in the chain (Rabek 1967), which are not present in our polymers.

The goal of the present work is to further establish the phenomenology for the observed effect and to identify possible coupling between polydienes and light. Towards this direction, a characterization of the material upon irradiation and pattern formation will be performed, to uncover possible molecular modifications due to laser irradiation. The effect of varying physical parameters (temperature, chemistry and architecture) on the kinetics of formation and the obtained pattern as observed by microscopy will be reported in order to discover possible perspectives and open new routes to patterning in complex systems.

$$U_{grad} = \frac{1}{2} n_o \alpha_{blob} E^2$$

References

Adam, C., J. Lacoste and J. Lemaire (1991). "Photo-oxidation of polyisoprene." Polymer Degradation and Stability **32**(1): 51-69.

Anyfantakis, M., G. Fytas, C. Mantzaridis, S. Pispas, H. J. Butt and B. Loppinet (2010). "Experimental investigation of long time irradiation in polydiene solutions: reversibility and instabilities." Journal of Optics **12**(12): 124013.

Anyfantakis, M., A. Koniger, S. Pispas, W. Kohler, H.-J. Butt, B. Loppinet and G. Fytas (2012). "Versatile light actuated matter manipulation in transparent non-dilute polymer solutions." Soft Matter **8**(8): 2382-2384.

Anyfantakis, M., B. Loppinet, G. Fytas, C. Mantzaridis, S. Pispas and H.-J. Butt (2012). "Self-induced transparency in diblock copolymer dispersions." Optics Letters **37**(13): 2487-2489.

Anyfantakis, M., B. Loppinet, G. Fytas and S. Pispas (2008). "Optical spatial solitons and modulation instabilities in transparent entangled polymer solutions." Optics Letters **33**(23): 2839-2841.

Anyfantakis, M., B. Loppinet, A. Pamvouxoglou, G. Fytas, S. Pispas and C. Mantzaridis (2013). "Kinetics of the concentration optical nonlinearity in polydiene solutions." in preparation.

Ashkin, A., J. M. Dziedzic and P. W. Smith (1982). "Continuous-wave self-focusing and self-trapping of light in artificial Kerr media." Optics Letters **7**(6): 276-278.

Boyd, R. W. (2008). Nonlinear Optics. Burlington, Academic Press.

Conti, C., G. Ruocco and S. Trillo (2005). "Optical Spatial Solitons in Soft Matter." Physical Review Letters **95**(18): 183902.

Delville, J. P., C. Lalaude, S. Buil and A. Ducasse (1999). "Late stage kinetics of a phase separation induced by a cw laser wave in binary liquid mixtures." Physical Review E **59**(5): 5804-5818.

Delville, J. P., C. Lalaude, E. Freysz and A. Ducasse (1994). "Phase separation and droplet nucleation induced by an optical piston." Physical Review E **49**(5): 4145-4148.

Dorkenoo, K., O. Crégut, L. Mager, F. Gillot, C. Carre and A. Fort (2002). "Quasi-solitonic behavior of self-written waveguides created by photopolymerization." Optics Letters **27**(20): 1782-1784.

Dorkenoo, K. D., F. Gillot, O. Crégut, Y. Sonnefraud, A. Fort and H. Leblond (2004). "Control of the Refractive Index in Photopolymerizable Materials for (2+1)D Solitary Wave Guide Formation." Physical Review Letters **93**(14): 143905.

dos Santos, K. A. M., P. A. Z. Suarez and J. C. Rubim (2005). "Photo-degradation of synthetic and natural polyisoprenes at specific UV radiations." Polymer Degradation and Stability **90**(1): 34-43.

Duhr, S. and D. Braun (2006). "Why molecules move along a temperature gradient." Proceedings of the National Academy of Sciences **103**(52): 19678-19682.

Golub, M. A. (1958). "The radiation induced cis-trans isomerization of polybutadiene." Journal American Chemical Society **80**: 1794-1798.

Golub, M. A. and C. L. Stephens (1967). "Photoisomerization of polybutadiene." Journal of Polymer Science Part C: Polymer Symposia **16**(2): 765-779.

Jacobsen, A. J., W. Barvosa-Carter and S. Nutt (2007). "Micro-scale Truss Structures formed from Self-Propagating Photopolymer Waveguides." Advanced Materials **19**(22): 3892-3896.

Kewitsch, A. S. and A. Yariv (1996). "Self-focusing and self-trapping of optical beams upon photopolymerization." Optics Letters **21**(1): 24-26.

Loppinet, B., E. Somma, N. Vainos and G. Fytas (2005). "Reversible Holographic Grating Formation in Polymer Solutions." Journal of the American Chemical Society **127**(27): 9678-9679.

Man, W., S. Fardad, Z. Zhang, J. Prakash, M. Lau, P. Zhang, M. Heinrich, D. N. Christodoulides and Z. Chen (2013). "Engineered optical nonlinearities and enhanced light transmission in soft-matter systems with tunable polarizabilities." submitted.

Nemirovski, Y., A. Szameit and M. Segev (2011). Nonlinear dynamics of light, fluid, and nano-particles: light-induced flow and beam collapse through radiation pressure. CLEO:2011 - Laser Applications to Photonic Applications, Baltimore, Maryland, Optical Society of America.

Rabek, J. F. (1967). "Photodegradation of cis-1,4-polyisoprene in solution sensitized by the addition of nitroso compounds in the presence of visible light." Journal of Polymer Science Part C: Polymer Symposia **16**(2): 949-963.

Sigel, R., G. Fytas, N. Vainos, S. Pispas and N. Hadjichristidis (2002). "Pattern Formation in Homogeneous Polymer Solutions Induced by a Continuous-Wave Visible Laser." Science **297**(5578): 67-70.

Sugiyama, T., K.-i. Yuyama and H. Masuhara (2012). "Laser Trapping Chemistry: From Polymer Assembly to Amino Acid Crystallization." Accounts of Chemical Research **45**(11): 1946-1954.

Voit, A., A. Krekhov, W. Enge, L. Kramer and W. Köhler (2005). "Thermal Patterning of a Critical Polymer Blend." Physical Review Letters **94**(21): 214501.

Voit, A., A. Krekhov and W. Köhler (2007). "Laser-induced structures in a polymer blend in the vicinity of the phase boundary." Physical Review E **76**(1): 011808.

Chapter 1 Molecular Characterization on Fibers formed upon red Laser irradiation

1.1 – Introduction

Previous studied revealed that the polydienes solutions can, upon irradiation, become partially insoluble in the good solvent for the initial material. It obviously points towards some changes in the material as a consequence of the irradiation and the writing process. In this part, we report attempts to characterize those changes by various spectroscopic techniques in order to gain a better understanding of the mechanism at work.

Micro-Raman was used to elucidate possible changes in the vibrational spectra. In order to explore the possible appearance of free radicals under the irradiation by laser light, Electron Paramagnetic Resonance (EPR) experiments were carried out, for solutions under irradiation. The solvent dependence on the radical formation was studied, to elucidate any relation with the differences in kinetics that had been measured by with phase-contrast microscopy experiments. Rheology and swelling experiments were also done to try to characterize the crosslinked material. A discussion of a possible scenario will be presented in the final part of the chapter.

1.2 – Materials and Techniques

1.2.1 – Materials

The samples consisted of cis-1,4 polyisoprene (PI), trans-polyisoprene and cis-1,4 polybutadiene (PB), having molecular weights of 1090, 400 and 390 kg/mol. The samples were dispersed in good solvents for polydienes. For EPR experiments the use of cis-1,4 PI was necessary due to the existence of the tertiary part next to the C=C bond. Five solutions were prepared in different solvents heptane, cyxlohexane, toluene, decahydronapthalene

(decalin) and tetrahydrofuran (THF) all at a concentration c=0.105g/mL. For RAMAN experiments cis-PI and cis-PB were prepared in tetradecane and carbon tetrachloride (CCl$_4$) also at c=10-15% wt. (We there used less volatile solvent in order to reduce evaporation effects). Trans-PI (obtained from (Aldrich) is highly crystallin . it was dispersed in hot cyclohexane 60oC with c=10% wt and let cool to room temperature.

1.2.2 – Extraction method

To allow characterization of the irradiated material, several methods were developed in order to extract the insoluble part it with as little as possible disturbance. The first method used was based on centrifugation. The samples were first irradiated with defocused beam for long period in multiple location in order to achieve "massive" writing. The sample was then diluted with the solvent used placed in a centrifuge cell and thereafter spinned down in a centrifuge for several hours. The undissolved material eventually sedimented down in the bottom of the centrifuge cell. The efficiency of this method was very low, probably due to the small density difference between written and unwritten material, despite the large formed insoluble structures (up to hundreds of microns). In a second method, a sample drop was placed on top of a transparent substrate and the laser irradiation was done from below, as recently reported (Athanasekos, Vasileiadis et al. 2012). The absence of sealing and the large area of contact between the sample and air severely limited the irradiation time. Moreover the irradiated material was difficult to extract from the glass substrate. Calcium fluoride substrates were used to limit Raman vibration bands in the wavenumber range we are interested in (1000-1800 cm^{-1}). A third method used for Raman experiments is described below and schematically depicted in figure 1.1. The initial solution was first placed in a homemade cell with removable top and bottom glass slide windows. After the irradiation of the sample for two hours with a focused beam (beam width ~28 μm), the bottom and top windows were removed and the rest of the cell was immersed and rinsed in hexane for several hours. The soluble polymer fraction

20

dispersed inside the solvent bath and. some of the irradiated material was found to remain stacked between the two side windows (entrance-exit windows) in the cell. The sample was then dried at room temperature). A picture of the extracted bundle obtained is shown figure 1.2 right, together with the typical pictures of solution after irradiation and before extraction (1.2left). The length of the bundle is controlled by the cell size, i.e 4mm and the adhesion on the entrance and exit windows to the formation of a tree-like structure upon drying (1.2 right).
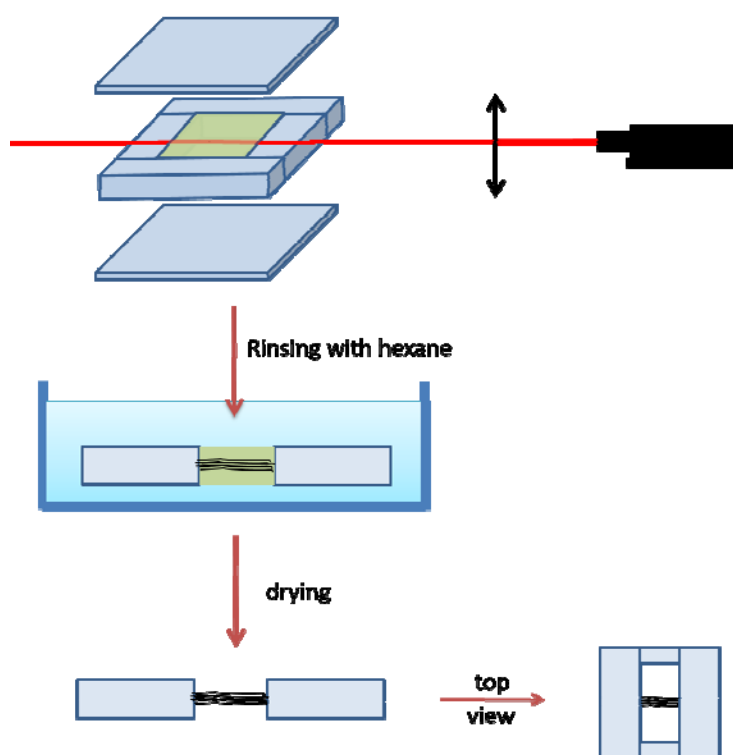

Figure 1.1: Extraction process of materials.

Apart from bundle structures, independent single fibers were also extracted. The single fibers are extracted in small amounts probably during the rinsing process. The single fibers could nicely be imaged by , Scanning Electron Microscopy (SEM). Figure 1.3 shows SEM pictures from the single fibers obtained from the process described above. To do so, fibers were placed in a microscope glass and sputtered with 5 nm gold coating. The fibers formed have a very homogeneous circular cross-section with average 3.8 µm diameter. This is in good agreement with microscopy pictures in the dry state (~5µm) shown in figure 1.4.

In the phase contrast microscopy the solvent-swollen fibers formed were measured to be around 10 μm diameter. Interestingly, the observed fibers looked similar to polybutadienes fibers obtained by electrospinning and UV curing (Choi, Hong et al. 2006).

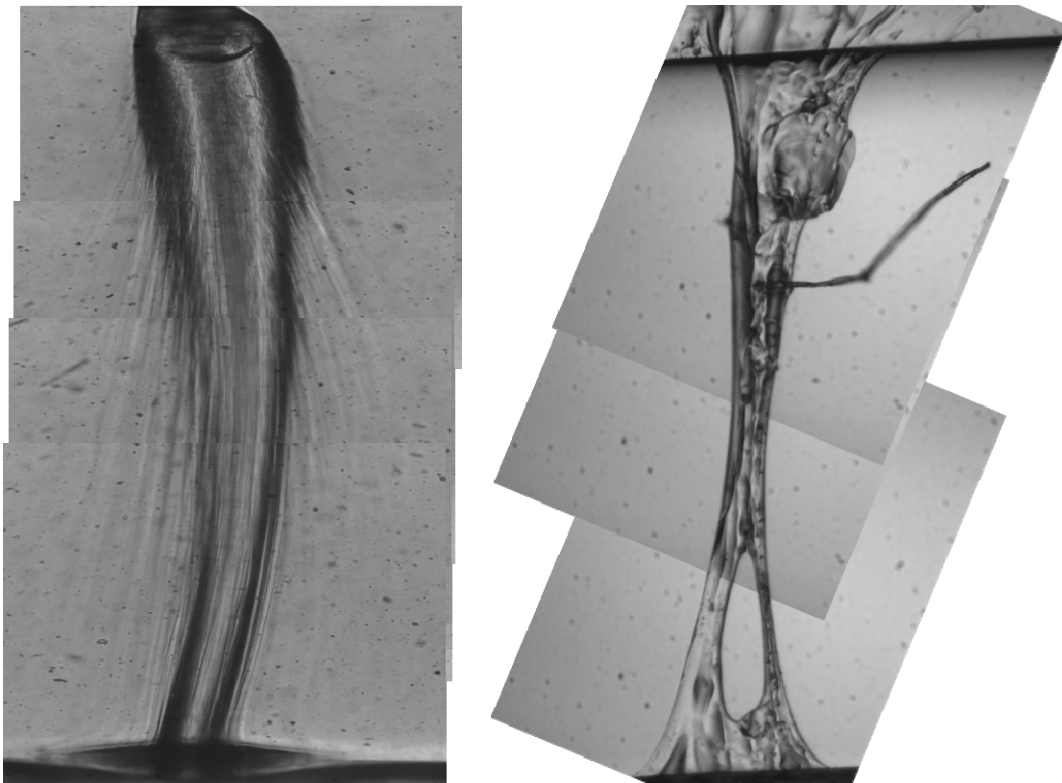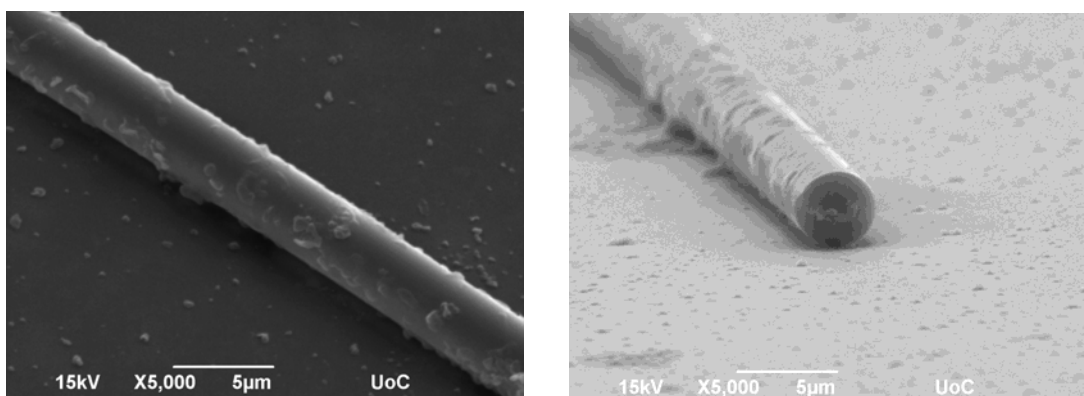
Figure 1.2: Microscopy pictures of the written polybutadiene in solution (left) and extracted (right)

Another examples of extracted material is shown in Figure 1.4. The length of the written material is limited only due to the cell size (~6mm).
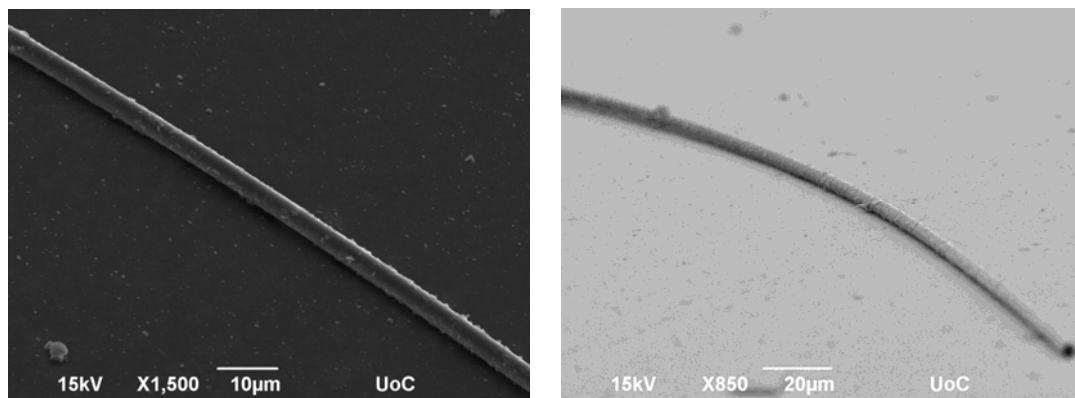
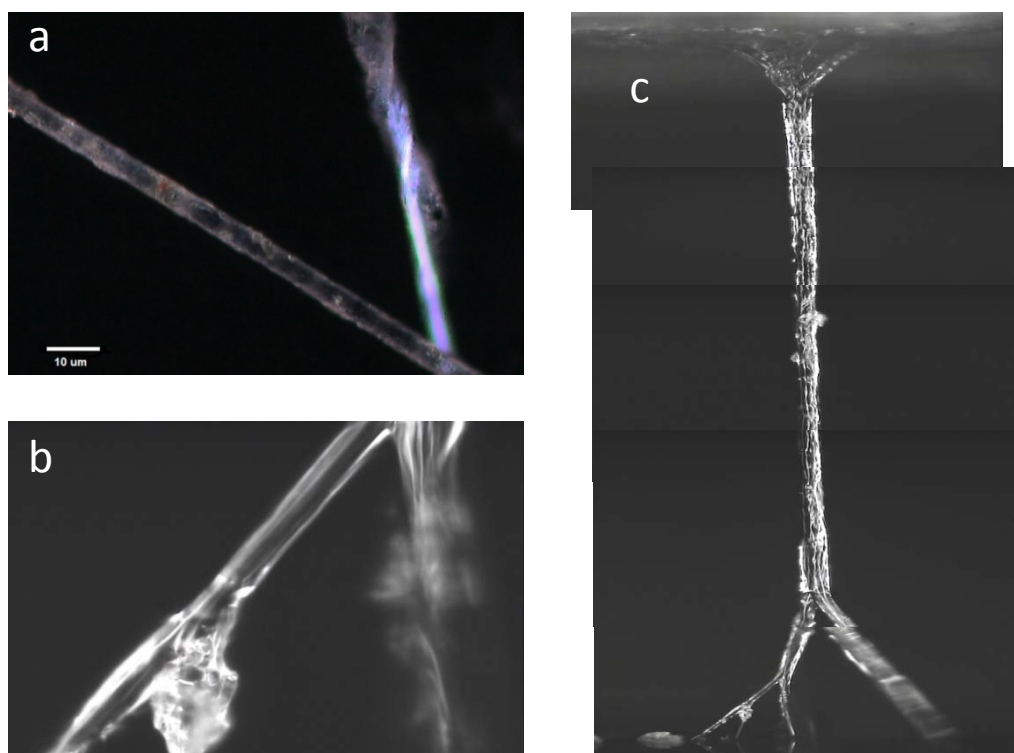**Figure 1.3:** SEM pictures of the extracted written polybutadiene

Figure 1.4: Microscopy pictures of the extracted written polybutadiene

1.2.3 Micro-Raman spectroscopy

Micro-Raman spectroscopy was used in order to check possible local changes in the molecular vibration spectrum during the irradiation process. Two commercial micro-Raman spectrometers were used, one mobile micro-Raman, one confocal Raman.

A mobile Raman Spectrometer (HE 785, Horiba – Jobin Yvon, France) was used, based on a semiconductor diode laser source emitting at 786 nm, fiber-optic coupled to a compact optical-probe head, bearing the necessary optics for sample excitation and signal collection.

The focusing lens can be chosen from a set of microscope objectives with different magnifications: for the experiments considered here, 20x (0.2 NA) and 50x (0.4 NA) objectives were used. Collection of the Raman scattering signal is provided by the same objective which delivers the backscattered light through an edge filter to a second optical fiber connected to a spectrograph that was coupled to a Peltier-cooled CCD detector (Horiba Synapse). This setup performs measurements in the range of 50-3200 cm^{-1}, with a spectral resolution of 4 cm^{-1} and a maximum power on the sample of 50 mW.

The confocal Raman used during this study (Nicolet Almega XR Raman spectrometer) is shown in figure 1.5. A laser beam (λ = 780 nm, P = 15 mW) is focused on a micron-sized spot in the sample through a microscope objective of high numerical aperture. Back-scattered light is collected and collimated by the same objective lens. The Rayleigh line is blocked by an appropriate notch filter. The different frequency components of the inelastically scattered light are dispersed in a monochromator, whose entrance slit is replaced with a pinhole. A CCD detector is placed in its exit focal plane so that the whole Raman spectrum is recorded. Due to the confocal scheme, only light from the focus can penetrate through the pinhole; light from other depths in the sample is efficiently blocked. As a consequence, out-of-focus regions do not blur the signal, but are dark. A schematic representation of a typical micro-Raman setup is shown in figure 1.5:

Raman experiments were performed both in solution and in extracted material. In solution Raman spectra were measured by imaging the irradiated material in the solution cell used for the laser irradiation. An un-irradiated material spectrum was measured very close to the written pattern in order to be used as a reference.
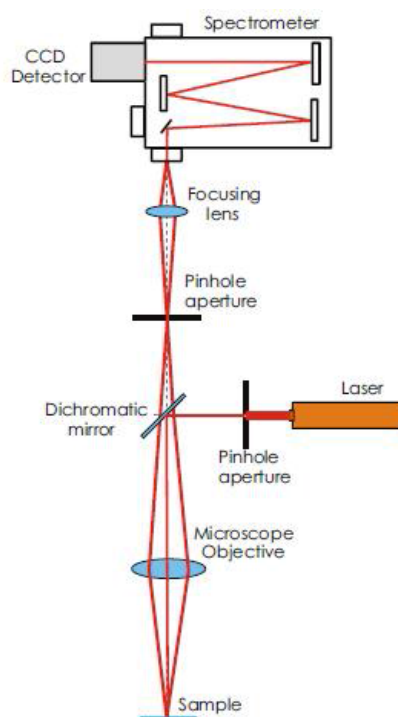
Figure 1.5 : Schematic representation of a typical micro-Raman setup

1.2.4 – Techniques– Electron Paramagnetic Resonance (EPR) for free radical detection and characterization

Electron paramagnetic resonance (EPR) or electron spin resonance (ESR) spectroscopy is a technique for studying systems which have at least one unpaired electron in their composition. The principle behind this technique is the interaction between the unpaired electron spin with an external magnetic field. When subjected to an external uniform magnetic field, the absorption of electromagnetic radiation by molecules with unpaired electrons gives rise to transitions between energy levels that are degenerate in

absence of the field, but become split in its presence, the splitting being proportional to the field strength (Zeeman effect see appendix). The transitions between these levels are evidenced by subjecting the system to another magnetic field (an oscillating one, and perpendicularly oriented with respect to the uniform field) if a resonance condition is satisfied. The existence of at least one unpaired electron is crucial, and since most stable molecules exist in singlet state (having all their electrons paired), the applicability of EPR techniques is reduced. This limitation may be viewed as an advantage, since it allows the study of specific molecules enclosed in otherwise EPR silent materials, provided the life-time of the unpaired electron is long enough. It is particularly well suited for detecting possible long-live free radical that would appear under irradiation.

Unlike most traditional techniques, in EPR spectroscopy the radiation frequency is held constant while the magnetic field is varied in order to obtain the absorption spectrum. When an electron is placed within an applied field, B_o, the two possible spin states of the electron have different energies. The lower energy state occurs when the magnetic moment of the electron is aligned against the magnetic field and a higher energy state occurs where m is aligned against the magnetic field. The two states are labelled by the projection of the electron spin, M_s, on the direction of the magnetic field, where $M_s = -1/2$ is the parallel state and $M_s = +1/2$ is the antiparallel state.
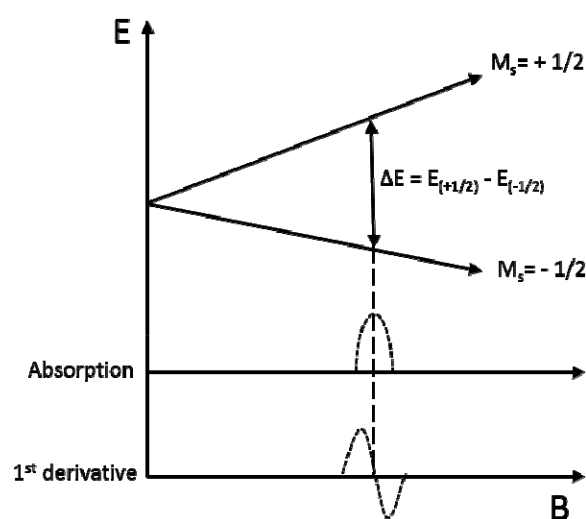

Figure 1.6: Energy levels for an electron spin ($M_s = \pm 1/2$) in an applied magnetic field. Absorption and 1st derivative of the absorbed microwave radiation.

Like most spectroscopic techniques, when radiation is absorbed, a spectrum is produced similar to figure 1.3. In the EPR spectrometers a phase-sensitive detector is used which results in the absorption signal being presented as the first derivative. The absorption maximum corresponds to the point where the spectrum passes through zero, which also determines the centre of the signal.

In order to perform is-situ experiments, a EPR sprectrometer with the necessary window was required. Therefore experiments were performed in MPIP Mainz under the supervision of Dariush Hinderberger. The modifications were originally developed to reveal nanoinhomogeneities in the structure and reactivity of thermoresponsive PNiPAM hydrogels (Junk, Jonas et al. 2008). Figure 1.7 shows the modified EPR together with the optical setup for irradiating the sample. Experiments were performed using a Magnettech miniscope MS 200 EPR spectrometer. The frequency of the EPR was locked at 9.38 GHz and sweeps of 6 mT were performed from 332 mT to 338mT. The sweep time was one minute, with the accumulation of several sweeps needed due to very low signals.

The laser for "in-vivo" experiments was a Diode Pumped Solid State (DPSS) with λ=670 nm and power P=300 mW. A convex lens of f=200mm was placed at a distance of 330 mm from the cell, with the beam waist of ~1mm diameter. The laser beam was passing through the center of the sample cell, without affecting the EPR setup.
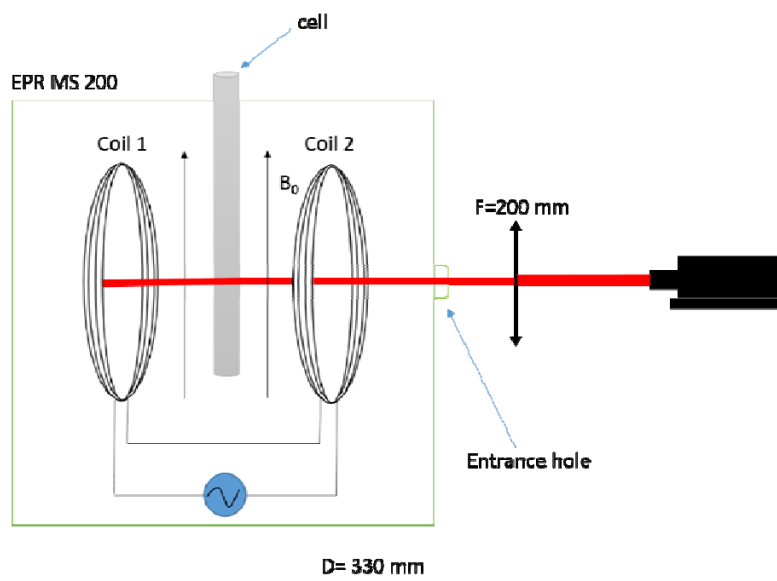
Figure 1.7: Schematic representation of EPR experiments (in-vivo)

The protocol used for these experiments was the following: first a background was acquired with the sample before light irradiation started. Then the same sample was irradiated for several hours, during which EPR scans were acquired. EPR scans continued after the LASER switched off in order to monitor the possible decay of the radicals. The systems studied are Polyisoprene solutions at high concentrations ($c \gg c^*$).

The EPR spectrum measured for the solution in toluene before laser irradiation is depicted (fig 1.8) was averaged over 40 scans (40 min). No specific feature could be seen in this background signal, confirming the expected low level of free radicals in such solutions.
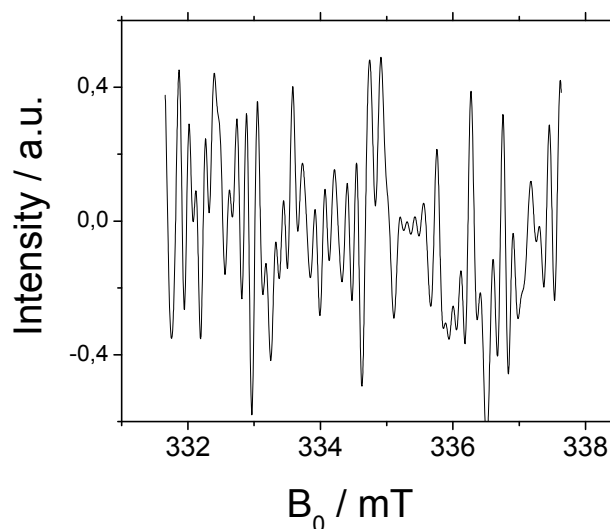
Figure 1.8: Typical baseline the EPR data. Figure shows the subtraction between the averages of the first 40 scans with the averages of the last 40 scans.

1.3 – Results

Raman experiments

The fact that the "written" (irradiated) material is insoluble in good solvents like alkanes, toluene and can be extracted (Anyfantakis, Fytas et al. 2010; Athanasekos,

Vasileiadis et al. 2012) suggests that some molecular alterations occurred during the irradiation process. Raman scattering was employed to study possible laser-induced changes in the molecular structure of the pollydienes. A μ-Raman consisting of a laser beam at λ=780 nm was used, along with a microscope at several magnifications from x20 – x100 objectives.

The Raman spectra of the used polybutadiene (left) and polyisoprene (right) are shown in figure 1.9. Some characteristic peaks that will be of interest to check for modifications are shown with arrows. The peak at 1667 cm^{-1} corresponds to C=C stretching and the area between 1200-1500 cm^{-1} corresponds to CH$_2$ vibrations.

Figure 1.9: Typical Raman spectra with some characteristic peaks for polybutadiene (left) and polyisoprene (right)

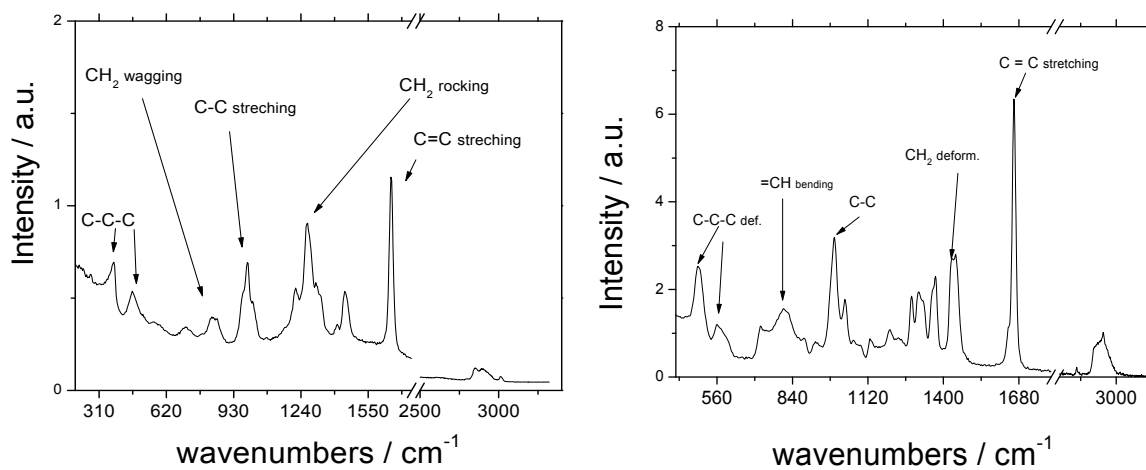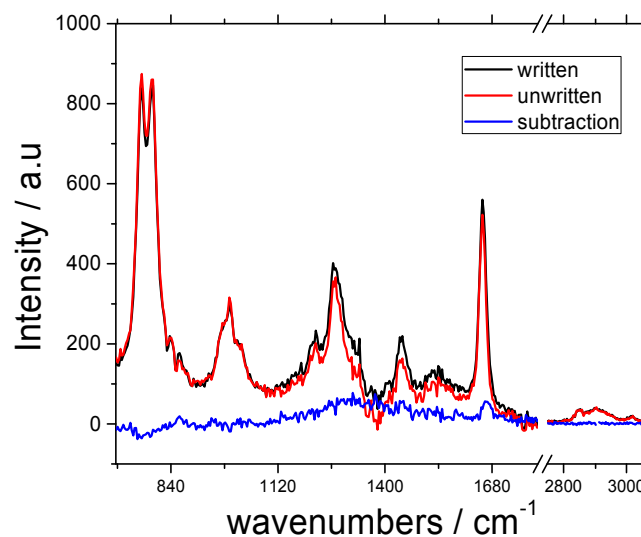**Figure 1.10:** Raman of PB in CCL$_4$ at c=15.4% wt. Red line represents the "clear" unwritten solution and black line the fibrilar structures (written) in the solution. For direct comparison the subtraction of two is plotted (blue line).

Figure 1.10 depicts written and unwritten spectra obtained for the solution Polybutadiene in carbon tetrachloride (CCl$_4$) solvent at concentration of 15.4% wt. CCl$_4$ was used of as solvent since it offers a good separation of the Raman peaks of the polymer and the solvent. All the Raman peaks of CCl$_4$ are below 840 cm^{-1}. The two Raman spectra do not show strong differences. In fact they are almost identical. In particular, there is neither an appearance of new peaks nor a shift of the positioning of the peaks, as clearly depicted in the subtraction of the two (blue line). Small deviations from the intensity of the two peaks can be attributed to small differences in the local concentration. Experiments using different solutions and concentrations did not show significant differences between written and unwritten material. One reason might be that the measured volume mostly consisted of unwritten polymer even in the "written-material" spectra, The possible local molecular alterations in the fiber bundles are then not very apparent in the "in situ" measurements . Raman experiments were then performed in the extracted dried material.

Figure 1.11 shows the Raman spectrum of the extracted dried PB (red line), together with the spectrum of pristine PB (black line). The subtraction between the two spectrums (blue line) is also shown. Four very clear differences are visible in the spectra of the extracted written materials and the original one, which become very apparent in the subtraction. The most noticeable changes are:

- The appearance of the peak at 1146 cm^{-1} which corresponds to vibration in the trans-PB
- An additional peak at 1570 cm^{-1} which does not correspond to any vibration spectrum of PB.
- A strong broadening of the peak at 1250 cm^{-1} which is due to CH$_2$ conformations. The intensity of the peak is increased by a factor of two.
- A decrease of the peak and a broadening at 1667 cm^{-1} is observed which refers to C=C bond vibrations.

30

A cis-trans isomerization of the butadiene could possibly explain the change in the Raman spectrum.

Figure 1.11: Raman spectrum of cis-1,4 polybutadiene before (black line) and after (red line) irradiation. For direct comparison a subtraction the two spectra is plotted (blue line)

Figure 1.12 shows the Raman spectra for cis-1,4 Polyisoprene 1096 kg/mole. Red line represents the spectra after irradiation and extraction and black line the pristine PI from the same batch. For direct comparison the subtraction of the two spectra is plotted (blue line). Obvious differences between the spectra are:

- An appearance of additional peaks at 850 and 916 cm^{-1} ,which corresponds to a trans-PI vibration spectrum
- Broadening of the area between 700-920 cm^{-1}.
- Decrease of the peak at 1667 cm^{-1} which corresponds to C=C stretching
- Decrease of the peak at 1000 cm^{-1} corresponding to C-C stretching
- Small broadening of the peak at 1667cm^{-1}
- Broadening of the peak at 1447 cm^{-1} which correspond to deformation of CH$_2$ groups of the macromolecules.

Other less obvious differences between the spectra are observed in the relative peak intensities, however no clear conclusions can be made due to high background intensity in the written material. The clear differences can tentatively be ascribed to molecular changes and possibly to cis-trans isomerization due to red laser irradiation, the trans conformation is energetically more favorable.
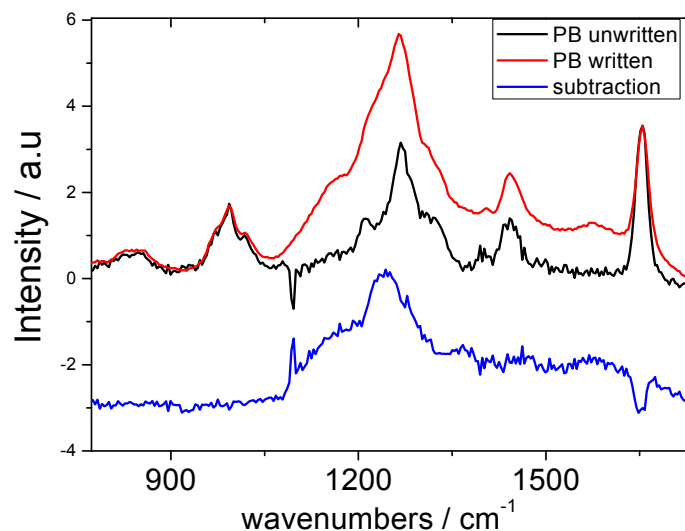
Figure 1.12: Raman spectrum of cis-1,4 polyisoprene before (black line) and after (red line) irradiation. For direct comparison a subtraction the two spectrum is plotted (blue line)

The possibility of cis-trans isomerization rises the question of irradiation effect on trans-Polyisoprene. Trans PI is indeed responding to the red light irradiation in a similar fashion than cis-PI (see next chapter for more details). Figure 1.13 shows Raman spectrum of trans-PI before (black line) and after irradiation (red line). For clear comparison, the subtraction of the two is plotted (blue line).
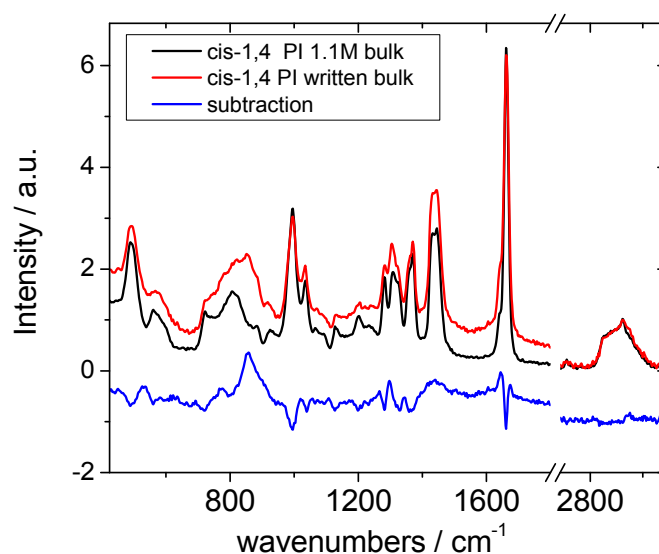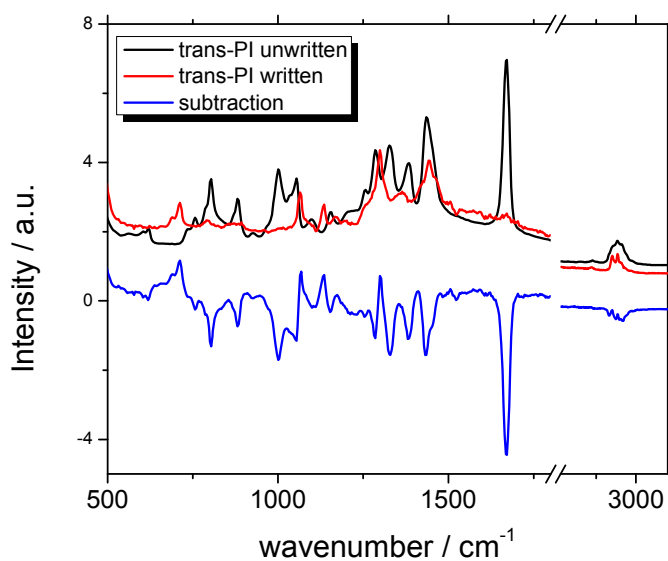

Figure 1.13: Raman spectrum of trans polyisoprene before (black line) and after (red line) irradiation. For direct comparison a subtraction the two spectrum is plotted (blue line)

There are number of noticeable changes like:

- Significant decrease of the peak at 1667 cm^{-1} (C=C stretching) decreases significantly.
- Disappearance of the peaks at 800, 875 and 1000 cm^{-1}.
- An appearance of peaks at 711 and 1129 cm^{-1} is observed which the correspondence vibration not to be present in the trans-Polyisoprene.

These clear differences cannot be easily ascribed to any specific changes in the polymer microstructure, but nevertheless confirm some level of modification upon red laser irradiation. Ongoing Raman experiments are needed for a clearer identification.

EPR experiments

In order to check for the possible appearance of free radicals during red laser irradiation, EPR experiments were performed. The Irradiation power was 250mW with a lens of f=20 cm placed 33 cm away to create a defocused beam of 1mm diameter. Figure 1.14 shows the time dependent EPR spectra measured for a PI-toluene solution (c=0.105g/ml) with red laser light irradiation turned on. The black line represents the spectra without irradiation and the red and green lines the evolution of ESR spectra after 100 and 400 min respectively. Each spectrum represent the average of 50 scans accumulated over 50 min and the given name/time correspond to the time of the last averaged scan. Appearance of a clear 4 double peak signal around 334 mT within the first 20 minutes of sample irradiation was observed. At initial times (t=0) the signal was low and the accumulation of at least 25 scans was needed. This signal, though relatively weak and requiring long accumulation time, is the clear sign of the presence of free radicals in the irradiated sample, which were not there before irradiation.
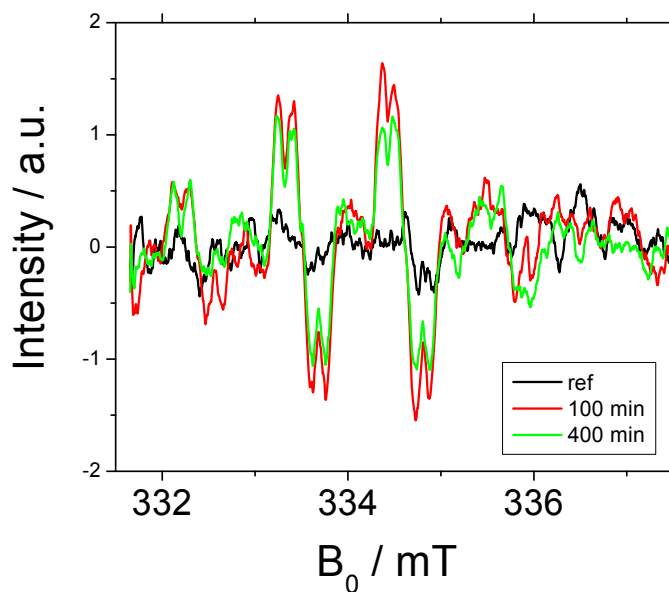
Figure 1.14: In-vivo evolution of radical formation for PI in toluene at c=0.105 g/ml
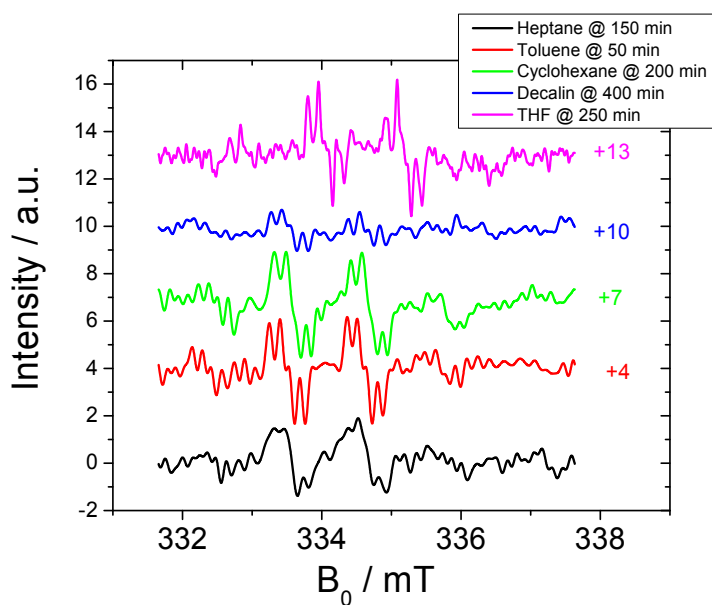
Figure 1.15: "In-vivo" evolution of radical formation at the maximum intensity for each of the five solvents measured.

Figure 1.15 shows the typical EPR spectra obtained for solution in different solvents, at time where the maximum signal was observed. 4 double peaks features are observed in all solvents, with however intensity variation. In particular, the signal is weaker in decalin

and the peaks are less well marked in heptane. In THF the peaks are slightly shifted compared to the other cases[1].

The relatively large accumulation time required to obtain good signal did not allow to obtain precise knowledge on the kinetics of the radicals' formation. However, a crude estimate of the evolution of the radical concentration could be obtained by double integration of the 4 double peak feature. Figure 1.16a shows the resulting integrated intensity of radicals during laser irradiation as a function of time for the four different solvents which is proportional to the free radical concentration. In cyclohexane, the intensity was found to increase untiul a maximum reached after ~200 mn and then to decay and eventually to remain constant. In heptane solution the intensity was found to increase and then to remain constant. In the other solvents the intensity was found overall constant over time, with some fluctuation.

After 400 min of irradiation the laser was switched off and the EPR was kept on, to measure eventual decay time of the radicals. The integrated intensities are shown in figure 1.16 right). In cyclohexane solution the highest concentration of radicals was observed.
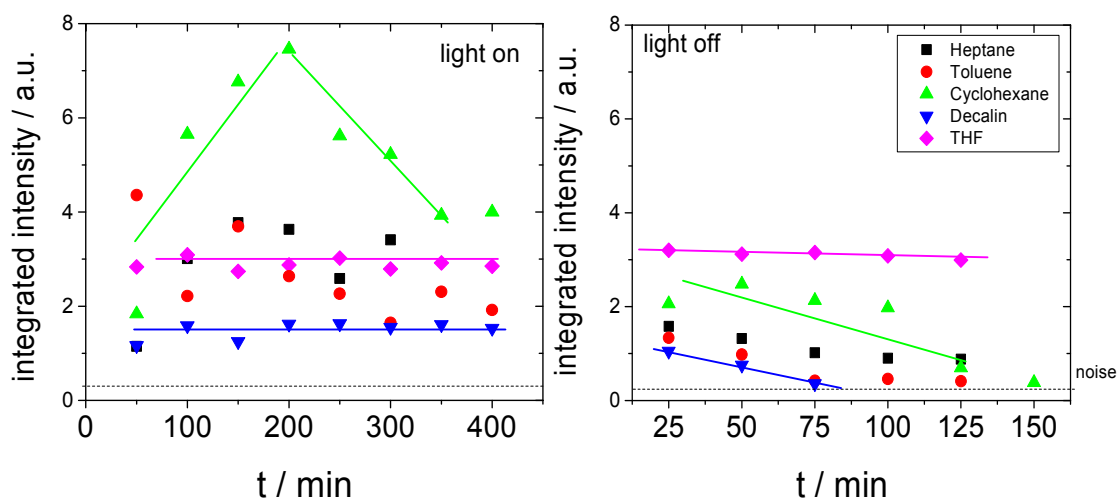
**Figure 1.16:** Comparison of the integrated intensity (no. of radicals) at different solvents with light on (left) and light off (right)

---

[1] THF absorb a lot in the GHz regime and we had difficulties to lock the frequency at 9.38 GHz. This slight shift of the spectra in THF could be related with a possible non-proper lock of the frequency.

After switching off the light, intensity started to decrease in all but THF solutions decreasing towards the minimum measurable threshold, corresponding to a low radical concentration present in the samples. In THF solution the intensity remained constant over the 125 mn of the measurement. In toluene, the radicals fully decay in about 75 min after switching off the laser. Similar trend was observed for the solution in decalin. In Cyclohexane, where the radical signal was the strongest, the decay to zero intensity took about 130 mn.

The purpose of using different solvents was to vary the kinetic of formation (diffusion conditions) and to establish possible connection between the number of radicals and the pattern formation. Figure 1.17 shows the fibers formed after in-vivo EPR experiments, for the different solvents. The length is the diameter of the NMR tube that we used for the experiments (4 mm). The most stable fibers are formed in heptane and cyclohexane solutions, with the first fiber appearing in less than a minute. On the other hand in toluene solutions (red points), the formed fibers were unstable, breaking into small pieces, creating mainly dots of written material rather than continuous fibers.

Figure 1.17: Microscope pictures from fibers formed after the EPR measurements from top to bottom: The color of the boarder corresponds to the solvent used. The length correspond to the size of a NMR cell (~4 mm).

In decalin solution (blue points), the rate of formation observed from phase-contrast microscopy measurements is 10 times slower than in toluene solution and 40 times slow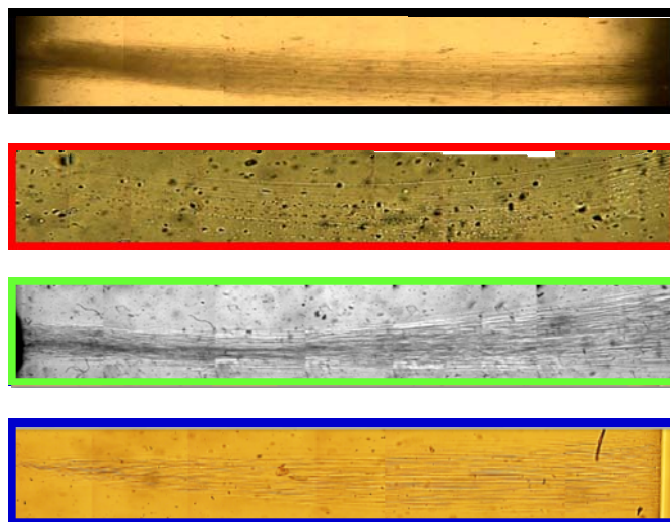er than in alkane solutions (hexane,heptane). Yet the fibers formed appear to be stable, and similar to the fibers from alkane solutions (figure 1.17, blue boarder). Interestingly, the decalin solution showed the lowest concentration of radicals. In the case of PI in THF solvent, a strong signal in the EPR spectrum was observed, which remains even after 200 min from the laser switch off. There the appearance of a "negative" pattern with solvent-rich central part was evidenced (Anyfantakis, Koniger et al. 2012), clearly different from the standard "positive" patterns observed in most other solvents. In this case, despite the large number of formed free radicals, the formed patterns are not stable and no structure can be seen by microscopy. We could expect the free radicals may cause some cross-linking in the material, which helps the fibers to sustain its fibrilar structure. But in THF there is therefore no obvious correlation between the pattern stability and the free radical concentration.

The 4 double peaks EPR features is characteristic of carbon-centered free radicals upon laser irradiation. By breaking C=C, two freely rotating groups are created with two neighboring tertiary groups. The tertiary group of (CH2-**C**-CH2-CH) is giving rise to the EPR feature, as the relaxation of (H-**C**-CH2-CH) is very fast and outside of the EPR measurement range. The four double peaks observed in the spectra correspond to the methyl groups that have appeared in the polyisoprene. The doublets are due to the methyl groups that are attached next to the carbon that was connected with the double bond. Polybutadiene has only 2 methyl substitutes next to the double bond, so the EPR relaxation is expected to be faster than EPR threshold.

The minimum number of radicals that the EPR setup can capture is estimated to be in the order of 10^{15} radicals. In our case, given the optical experimental conditions (beam waist $2w_0$=1 mm, length= 4mm), it will correspond to a concentration of the order of 10^{15}/3 mm^3 or $3*10^{20}$ radicals/L, which is roughly ~0.5mM. This concentration is to be compared to the monomer concentration. As the concentration was 105g/L and the monomer molecular weight is M_{PI}=68g/mol, this corresponds to ~1.5 M molar. Therefore, the estimated number of free radical is only a small fraction of the total number of monomer, of the order of one

every 30000. To compare, for a M=1096kg/mol polymer the number of monomers are ~16000. The observed free radicals are of the order of one per chain or less, which is a very small number, probably to low to expect network formation.

A free radical can either recombine back and form again the double bond or find another free radical and make a stable bond. If none of this two happened, then the radical will remain free. The ratio between creation – recombination is what EPR spectrometer can capture. The precise recombination mechanism should have to do with the environment that surrounded the radical. Direct comparison of the concentration of EPR-detected radicals with a cross-linking density is difficult. Observation of long-lived radicals does not exclude the presence of short lived ones that react to create the needed crosslinks.

Photooxidation and photodegradation of polydienes

Due to industrial importance of polydienes, especially as the main component of tyres, the stability of dienes polymers has long been of interest and therefore studied carefully. Below we summarized what is known for light induced chemical changes in polybutadienes and polyisoprenes, and discuss the possible relevance of such processes for the observed chemical modifications after laser light irradiation.

The processes of polymer degradation and crosslinking may be also due to secondary chemical reactions following the primary chemical reaction in the system, in which the polymer macromolecule does not participate. Diene polymers are resistant to visible light (400-800 nm). In the presence of oxygen these polymers are rapidly degraded by sunlight or ultraviolet radiation. The ultraviolet radiation not only intensifies the oxidation reaction but also photodegrades the polymer. In an atmosphere free of oxygen in a polymer irradiated by ultraviolet radiation two parallel processes are observed, namely, photodegradation and crosslinking.

Diene polymers in solutions are easily degraded or crosslinked. The reaction course depends upon a number of physicochemical factors such as the structure of the polymer, its concentration in solution, type of solvent, the presence of oxygen and other chemical agents and their reactions, intensity and energy distribution of incident light, etc.

Photochemical processes in the macromolecule take place then only when the energy of absorbed light quanta is at least equal to the dissociation energy of the bonds between the atoms in the main chain.

In photodegradation, irradiation brakes C=C bond due to excitation of the π-electrons. Golub et al. (Golub and Stephens 1967) reported in similar polymers irradiating with 253 nm wavelength, that the energy need to break C=C bond was transferred through solvent molecules, with interconversion of polymer and solvent molecules to take place. Experiments on Polyisoprene and Polybutadiene samples irradiating with γ-rays (Golub 1958; Tsurugi, Fukumoto et al. 1967) show cis-trans isomerization, which under certain conditions was reversible. Similar observations were found in polybutadiene using ultraviolet laser light (Golub and Stephens 1967; Ng and Guillet 1978; dos Santos, Suarez et al. 2005)

Photochemistry may occur in two ways: photooxidation and photodegradation. In photooxidation, the creation of oxygen substitutes such as hydroperoxides, leads to creation of ketones and aldehydes in polyisoprene/polybutadiene molecules which change dramatically the molecular structure, depending on oxygen permeability occurring under irradiation. Piton et al. (Piton and Rivaton 1996) observed strong changes in the IR spectra, after PB irradiation by UV light, especially in the range of 1720 cm^{-1} and 3400 cm^{-1}, which correspond to C=0 and C-O vibrations respectively. Photooxidation of polymers upon red laser irradiation could be a possible mechanism, since it is the only reported mechanism that crosslinks the material using wavelengths in the visible area. In our case, ATR/IR experiments performed in written and unwritten polyisoprene show no significant differences apart from the peak at 3400 cm^{-1} which amplitude was increased by factor of two. The relative small differences in amplitude and the absence of other noticeable differences rule out photooxidation process as the dominant mechanism for radical

formation. Moreover EPR spectra show that the type of radical we observe does not include oxygen.

The mystery remains if and how photooxidation could occur. A possible mechanism is that the necessary oxygen which will attack the polydiene is transferred through solvent molecules. The oxygen attacks the methyl group next to the double bond, creating a radical which can freely move around the double bond.
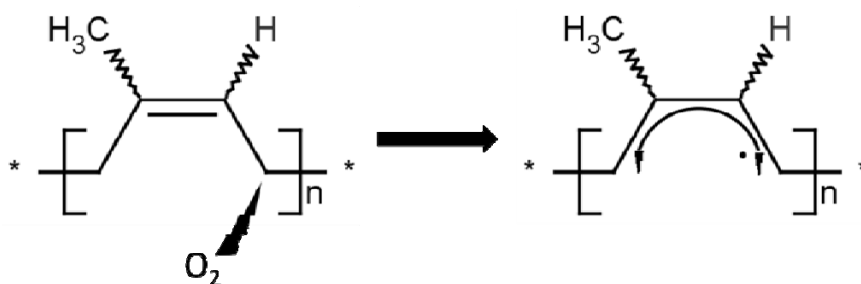
The presence of solvent molecules seems to be important since when we performed experiments under similar conditions in bulk polymers, EPR together with μ-Raman didn't show any differences between irradiated and non-irradiated sample.

Other Possible mechanisms could be two photon process, or through an absorption band that exists in the wavelengths we used. In order to have two-photon process, the absorbed wavelength should be in the range of 330 nm, half of the wavelength we used (λ=670 nm). Several reports on photodegradation show the use wavelengths around λ~320 nm in polydienes (PI and PB) (Adam, Lacoste et al. 1991; Piton and Rivaton 1996; dos Santos, Suarez et al. 2005), in contrast with most of the reports in photodegradation which use UV light (λ~250 nm) (Kaczmarek 1995; dos Santos, Suarez et al. 2005). We know also that the laser-polydiene coupling is more efficient using a red laser (633<λ<670 nm) rather than green laser (λ~530 nm).

As already mentioned, the polymers do not absorb in the visible range (400-800 nm). Figure 1.18 shows UV-VIS spectra of polyisoprene in heptane. The absorbance between 400-800 nm is very small and is due to scattering losses. This is evidenced in the inset of figure 1.18 where the absorbance between 400-800 varies from 5-10%. The sharp decrease of the absorbance below 300 nm is due to absorbance from the cell we used.

Oxygen can be transferred through atmosphere or through solvent molecules. Experiments performed in bulk polydienes show no photooxidation after irradiating it for several hours, meaning that only solvent could be a possible reservoir for oxygen molecules. Oxygen O_2 presents an absorption band at around 650 nm and a significantly smaller at 532 nm (Ogryzlo 1965). More experiments should be carried out to clarify the importance of the the presence of oxygen
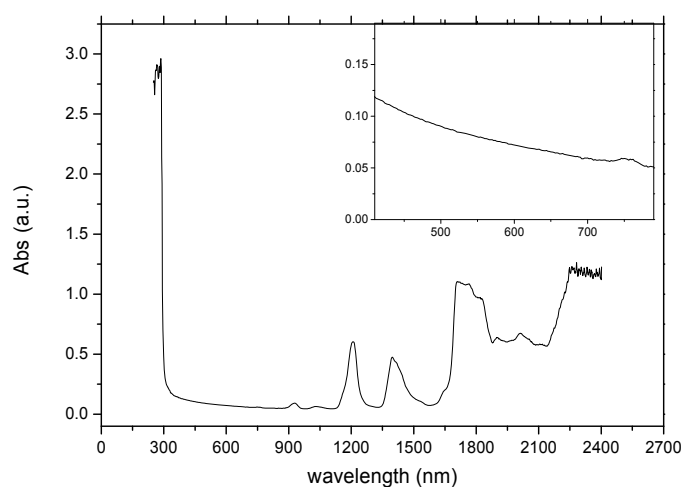
Figure 1.18: Absorbance spectra of polyisoprene in heptane at c=0.105g/ml

Swelling and Rheology experiments

From EPR and Raman experiments we conclude that upon red laser irradiation free radicals appeared during irradiation and the macromolecular structure exhibits chemical alternation. The ability to extract the written material which is insoluble and immerse it in good solvent points the presence of cross-linking, since the material does not redissolve and keeps its shape. The extracted material was immersed in heptane solvent, good solvent for polyisoprene, to reveal any swelling. Figure 1.17 show a swelling experiment of PI in heptane. The top picture shows bundles in dry state and the bottom bundles at maximum

swelling. Assuming cylindrical isotropic swelling of the bundles, swelling ratio can be extracted as:

$$\frac{V_{(t=0)}}{V_{(t=t_{max})}} = \frac{R^2_{t=0}}{R^2_{t=t_{max}}} \frac{\Delta L}{L}$$

with **V** to define the volume of the cylinder and **R** the radius and L its length, the calculated swelling ratio was 2.7. The swelling experiments provide a way to estimate the crosslink density using the Flory –Rehner formula for polymer network swelling

$$-[\ln(1-\varphi_2) + \varphi_2 + \chi\varphi_2^2] = V_1 n \left(\varphi_2^{1/3} \frac{\varphi_2}{2} \right)$$

where, φ_2 is the volume fraction of polymer in the swollen mass, the molar volume of the solvent, is the number of network chain segments bounded on both ends by crosslinks, and χ is the Flory solvent-polymer interaction term (see also figure 1.16). The crosslinking density was calculated around 25%.

Figure 1.16: Flory –Rehner formula for calculating the crosslinking density. ϕ_2 was calculated around 0.36 which roughly corresponds to ~25% crosslinking.
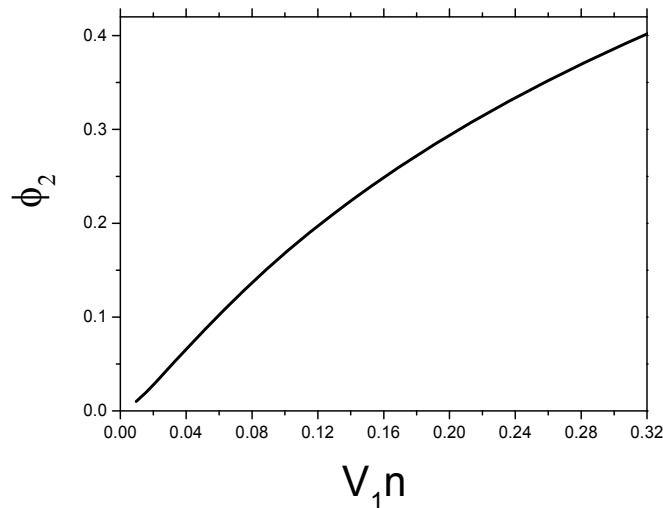
When the elastic modulus is the same with the viscous moduli, with the slope to be 0.5 over the frequency, the system behaves as gel-like (Mours and Winter 1996). Figure 1.18 show dynamic frequency sweep for unwritten PI (red points) and written PI (black points) at 20°C. In both cases the sample were not fully loaded in the rheometer due to small amount of sample. Values of G' and G" are underestimated but the trend is not affected. Unwritten material shows common behavior of viscoelastic bulk PI, i.e rubbery plateau. The written material exhibits power law dependence with a slope of 0.5 for both moduli, typical behavior for a gel-like material.

1.4 – Conclusion

The above results can be sum up as follow: through Raman spectra, a series of chemical modifications were observed before and after irradiation. Cis-trans isomerization could be a mechanism to describe modifications in the cis-polydienes. For the trans-PI, modifications were observed, yet is not possible to attribute to any known conformation. Rheology revealed a gel-like structure in the written material, which is due to cross-linking of the material. Swelling experiments can validate the gel-like behavior, with the material to keep its shape by immersing it in good solvent, causing a swelling ratio of two, which should correspond to about 25% crosslinking. This 25% is probably in agreement with the Raman spectroscopy result but much larger than the fraction of free radicals observed by EPR.

EPR spectroscopy detects a small number of long lived free radicals that are probably not directly involved in the chemical modification observed by Raman spectroscopy. The cross-linking needed (order of percent, i.e 100 more than the detection threshold of EPR) to create the insoluble but swellable extracted material is expected to happen on a fast rate which makes it "invisible" by EPR (as it is the case in most photo-chemical processes) . A chemical process is at work, caused (more or less directly) by the red laser irradiation.

Observation of long-lived radicals does not exclude the presence of short lived ones that react to create the needed crosslinked (order of ~ 25%). This 25% is in agreement with the observed change in the Raman spectra.

So far we were not able to apply time resolved spectroscopy that will allow to follow the chemical changes and to correlate them with the refractive index changes, to establish unequivocally the relation between the two. Real time Confocal Raman should be our best hope to elucidate possible changes in-vivo and correlate with the formed pattern.

We also need to understand / clarify how the red light could interact with the dienes moiety, the role of the solvent, etc. Below a brief summary of what is known about photo-induced changes in polydienes will be discussed.

1.5 – Future work

In spite of characterizing the written extracted material in order to elucidate the molecular changes that light does, further investigation is required to gain insight information of the light-induced process. As it was discussed previously, the mechanism which creates the free radicals is still missing. Moreover due to low signal from EPR data, we were not able to correlate possible coupling between radical formation and pattern formation at early times. Preliminary experiments from ATR/IR shows the presence of oxygen in the extracted materials pointing towards photooxidation, as a possible mechanism for the radical formation.

The possible role of oxygen should be checked. Future experiments should be directed to red laser irradiation in polydienes with absence of oxygen. This will confirm whether oxygen, through photooxidation contributes (fully or partially) to the radical formation. Moreover additional experiments in solution Raman will be performed in order to confirm the chemical modifications observed from extracted material.

Carefully designed real-time (confocal) micro- Raman experiments should also be able to reveal the time scale for chemical changes in the solutions during irradiation and correlate them with the pattern development.

1.7 – References

Adam, C., J. Lacoste, et al. (1991). "Photo-oxidation of polyisoprene." Polymer Degradation and Stability **32**(1): 51-69.

Anyfantakis, M., G. Fytas, et al. (2010). "Experimental investigation of long time irradiation in polydiene solutions: reversibility and instabilities." Journal of Optics **12**(12): 124013.

Anyfantakis, M., A. Koniger, et al. (2012). "Versatile light actuated matter manipulation in transparent non-dilute polymer solutions." Soft Matter **8**(8): 2382-2384.

Athanasekos, L., M. Vasileiadis, et al. (2012). "Micro-fabrication by laser radiation forces: A direct route to reversible free-standing three-dimensional structures." Optics Express **20**(22): 24735-24740.

Choi, S. S., J. P. Hong, et al. (2006). "Fabrication and characterization of electrospun polybutadiene fibers crosslinked by UV irradiation." Journal of Applied Polymer Science **101**(4): 2333-2337.

dos Santos, K. A. M., P. A. Z. Suarez, et al. (2005). "Photo-degradation of synthetic and natural polyisoprenes at specific UV radiations." Polymer Degradation and Stability **90**(1): 34-43.

Golub, M. A. (1958). "The radiation induced cis-trans isomerization of polybutadiene." Journal American Chemical Society **80**: 1794-8.

Golub, M. A. and C. L. Stephens (1967). "Photoisomerization of polybutadiene." Journal of Polymer Science Part C: Polymer Symposia **16**(2): 765-779.

Junk, M. J. N., U. Jonas, et al. (2008). "EPR Spectroscopy Reveals Nanoinhomogeneities in the Structure and Reactivity of Thermoresponsive Hydrogels." <u>Small</u> **4**(9): 1485-1493.

Kaczmarek, H. (1995). "Accelerated photodegradation of cis 1,4-polybutadiene in the presence of hydrogen peroxide." <u>Polymer Bulletin</u> **34**(2): 211-218.

Mours, M. and H. H. Winter (1996). "Relaxation patterns of nearly critical gels." <u>Macromolecules</u> **29**(22): 7221-7229.

Ng, H. C. and J. E. Guillet (1978). "PHOTOCHEMISTRY OF cis-POLYISOPRENE AND ITS SINGLET OXYGEN ADDUCT." <u>Photochemistry and Photobiology</u> **28**(4-5): 571-576.

Ogryzlo, E. A. (1965). "Why liquid oxygen is blue." <u>Journal of Chemical Education</u> **42**(12): 647.

Piton, M. and A. Rivaton (1996). "Photooxidation of polybutadiene at long wavelengths (λ > 300 nm)." <u>Polymer Degradation and Stability</u> **53**(3): 343-359.

Tsurugi, J., T. Fukumoto, et al. (1967). "Radiation Induced cis and trans Isomerization of Polyisoprenes and Temperature Dependence of the Equilibria." <u>Rubber Chemistry and Technology</u> **40**(4): 1222-1229.

[Type here]

Chapter 2   Exploring the sample's parameters

2.1 - Introduction

In this part, I report results concerning the kinetics of the refractive index change following the light irradiation. The local refractive index change is monitored through quantitative phase contrast. We observed the refractive index change in the focus of the beam, using cells with light path length of the order of the Raleigh length of the Gaussian beam.

For polyisoprene and butadienes homopolymer solutions, a phase contrast study has been completed and his given in appendix A. Here I will therefore mostly report recent experiments involving samples more complex (than the homopolymer solutions). The sample conditions were chosen to address specific question about the process and its kinetics and hopefully lead to some clarification about the mechanism of formation and its kinetics. One of such issue is the nature of the transport necessary for the increase of the polymer concentration and of the observed variation of refractive index (as we believe that $\delta n=(dn/dc)/\delta c$). Does the mechanism require flow or is it mostly diffusive? For this we used cross-linked sample where large macroscopic flow of the polymer is prevented. Also the use of co-polymer and selective solvent allows to obtain large viscoelasticity at low monomer concentration (compare to homo-polymer through supra-molecular aggregation).

2.2 – Materials and Techniques

Materials

Anionically polymerized, monodisperse poly (isoprene) (PI) as well as relatively monodisperse poly (styrene) – poly (butadiene) random copolymer (SBR) and poly (styrene) – poly (isoprene) - poly (styrene) (SIS) were used in this study. In addition, cis-1, 4 PB (Polymeri Europa) (polydispersity 2.5) and commercial trans-1, 4 PI (Sigma-Aldrich), were

also used. . Solutions in a broad spectrum of solvents were prepared, including linear and cyclic alkanes as well as toluene. Table 1 summarizes all the polymers used here and their molecular characteristics. The solutions used were prepared by adding the desired amount of solvent to a known amount of polymer in a glass vial.

Name	M (kg/mol)	microstructure	% 1,4 content	cartoon
PI-xlinked	70	cis-1, 4 5% x-linking	100	
PI-xlinked	70	cis-1, 4 10% x-linking	100	
tPI410	410	trans-1, 4	99	
PB390	390	cis-1, 4	92	
SBR	146	21.7 % PS 67,8% 1, 2- PB	25	
SIS	170	16 % PS	84	

Table 1: Characteristics of the polymers used in this study

The solutions were either stirred by a magnetic stirring bar or through vortexing to ensure fully homogeneous samples. The solutions were loaded into the sample cells using short glass pipettes, or syringes.

Phase contrast microscopy

Phase contrast imaging was implemented by means of the white light Köhler illumination unit of the microscope to create a collimated beam of a few mm, a 32x objective lens (O, Zeiss) and an 8-bit 640x480 CCD camera (Basler) with frame rate between 1 and 10 frames per second. The imaging was performed with a filter (F) placed in front of the CCD to block the scattered laser light. The images were acquired with the microscope objective lens

slightly defocused (~40 μm above the focal plane) to permit quantitative phase contrast analysis where the intensity measured at the CCD relates to the refractive index profile (see appendix).

2.3 - Light-polydiene interactions in homopolymer solutions

Effect of Antioxidant

We attempted to evaluate the possible effect of presence of antioxidant (2,6-Di-tert-Butyl-p-Kresol also known as BHT) during red-laser irradiation. After synthesis a reagent is added to the final product in chain. To prevent oxidation by the oxygen in air, an amount of antioxidant molecules is often added in small amount, typically ppm to polydienes. The role of antioxidant is to "grab" any oxygen molecules that could be present after the polymerization. If the concentration of radicals is crucial for the creation and the stability of the radicals, the concentration of antioxidants should affect the appearance of the pattern and their rate of growth. Figure 2.1 shows the kinetics of polybutadiene in heptane solution at the concentration of 11% wt. Black points show the kinetics in the absence of added Antioxidant. Red points show the observed growth when a large excess of antioxidant has been added (one antioxidant per ten Isoprene monomer?). Despite this large antioxidant addition, the kinetic of formation remain the same. Moreover the formed patterns in both solutions are also very similar as shown in the figure. A large variation of the antioxidant concentration does not seem to play a large role in the formation and it's kinetic. This finding somehow rule out the importance of the oxidation process in the formation, as no large scale oxidation is expected to take place in the presence of an excess of antioxidant.
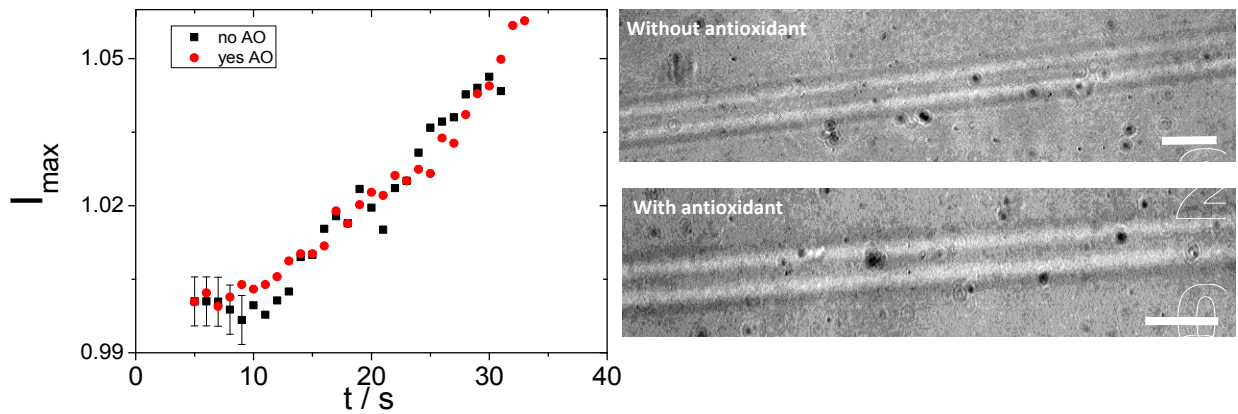
Figure 2.1 Kinetics curves of I_{max} vs. irradiation time for PB in heptane (c = 11 % wt) with (red points) and without (black points) antioxidant. The laser power is 240 mW. On the right we have images from phase contrast experiments that show fibers formed due to laser irradiation.

Pattern formation in crosslinked samples

In order to address the issue of transport and the presence (or not) and importance of flow during irradiation we performed experiments in chemical crosslinked polyisoprene. In two different sample environments. In the first case the polymer was crosslinked at two specific crosslinking densities creating a chemical gel. Typically in a crosslinked gel, there is absence of flow due to chemical crosslinking of the polymer which decreases the chain diffusion.

Figure 2.2 shows kinetic curves for polyisoprene (M_w= 70 kg/mole) in heptane at two different crosslinking densities 5% (black points) and 10% (red points) respectively. In both case a "waiting" time followed by a growth $\exp\Gamma(t-t_0)$ is observed. For both crosslinking densities the exponential growth starts at around 100s. For 10% cross-linking density a plateau is observed around 100s and above that the fiber formed start to move out of the irradiation volume.
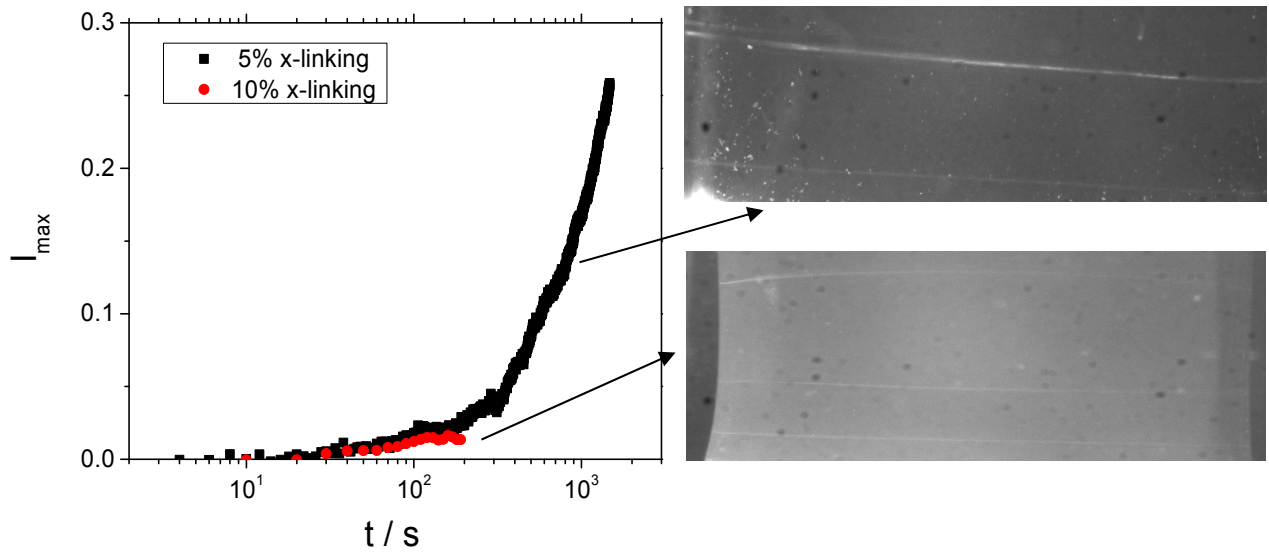
Figure 2.2: Kinetics curves of I_{max} vs. irradiation time for PI in heptane (c = 8 % wt) with 5% (black points) and 10% (black points) cross-linking density. Pictures on the right shows the fibers after four months inside the 10 mm square cell. the picture width is about the cell width (1 cm)

The observed local increase of concentration was found to be permanent as in the solution case. The fibers are stable and remained straight even after four months in the 10mm square cell (fig 2.2 right). The elasticity of the crosslink gel sample prevent sinking. The observed pattern correspond to a local increase of the refractive index, i.e a local increase of polymer concentration that is probably due to a local increase of the crosslink density. Even though the material is crosslinked, there is mobility between the anchoring points and together with the creation of radicals, an increase of the concentration is performed due to crosslinking rather than osmotic compressibility.

In order to directly check for the presence of flow in the sample during the process, we dispersed in a polydiene solution in good solvent, gold nanoparticles as tracers. Polybutadiene solution in cyclohexane was prepared at c= 0.1 g/ml.

Tracer particle could be imaged in the standard optical setup. Upon red laser irradiation and pattern formation, no significant motion or flow of the tracers was observed across the beam direction. In some cases we observed some flow but most probably due to instabilities during the experimental procedure and not clearly related to the "writing" process. At initial state, tracer particles are observed along the beam direction. By continuous irradiation, pattern formation was observed with the light to self-propagate through the fibers, as

in the "positive" case (2.3b). At the final state fibrilar structure was observed, similar to homopolymer solutions in alkanes.
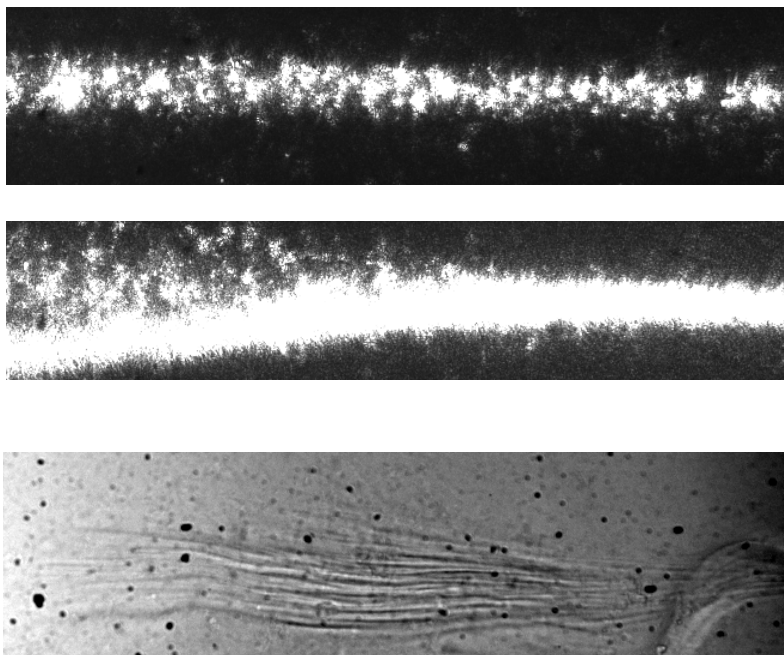
Figure 2.3: Phase contrast microscopy pictures of PB in cyclohexane doped with gold nanoparticles at **a)** t=0s , **b)** late state and **c)** late state with blue filter to remove the scattering intensity from the laser.

Kinetic of formation Trans-PI solutions

We attempted to further evaluate the influence of varying the microstructure of the polydiene by changing the chain conformation. The absence of effects in 1, 2-PB has already been reported by Sigel et al (Sigel, Fytas et al. 2002). Experiments on a solution of 1, 2-PB (M = 20 kg / mol) in hexane, at c = 57.73 % wt. confirmed the absence of response of this microstructure as already evidenced. After 1 hour of irradiation (P = 300 mW), no refractive index changes were detected.

To further check micro-structure trans-polyisoprene (M_w= 410 kg/mole, 99% 1,4 units) dissolved in toluene were also tested.
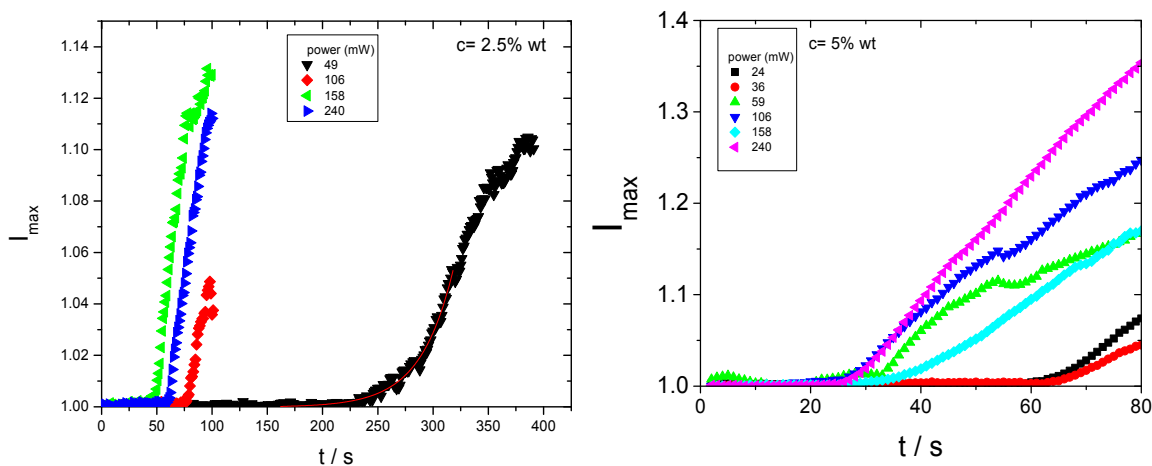
Figure 2.4: I_{max} as a function of irradiation time for different laser powers for trans-PI in toluene. The concentrations are 2.5 % wt (left) and 5% wt (right). Red line depicts the exponential fit to extract the growth rate.

Since trans-1, 4 PI is highly crystalline, solutions were prepared at relatively low concentration in toluene using heating to about 60°C to facilitate dissolution. The standard filament like pattern formation was clearly observed in these solutions. Kinetics measurements were carried out at room temperature with solutions of c=2.5 and c=5 wt. The increase of I_{max} as a function of irradiation time is shown for two different concentrations 2.5% (2.4 left) and 5% (2.4 right) respectively. Noticeably, in both concentrations a waiting time was observed before an exponential-like growth. This waiting time was not found to depend strongly on the used laser power at both concentrations. For the lowest concentration the waiting time varies from 50s at the highest laser powers up to 250s for lowest measured power. Surprisingly this waiting time is stronger at 2.5% wt, since for 5 % wt the waiting time varies around 20-60 sec for similar laser powers. The linear dependence of the growth rate on the different incident laser powers was confirmed in almost all cases. Figure 2.5 shows the dependence of the growth rate at different laser powers for the two concentrations studied. At 2.5% wt the slope is 1.5, significantly higher from the slopes observed for polydienes in alkane solution (Anyfantakis, Loppinet et al. 2008, Anyfantakis, Loppinet et al. 2014) which is close to one. In the highest concentration (5% wt) the rate is power independent, similar to what has been observed for polydiene solutions at very high concentrations.
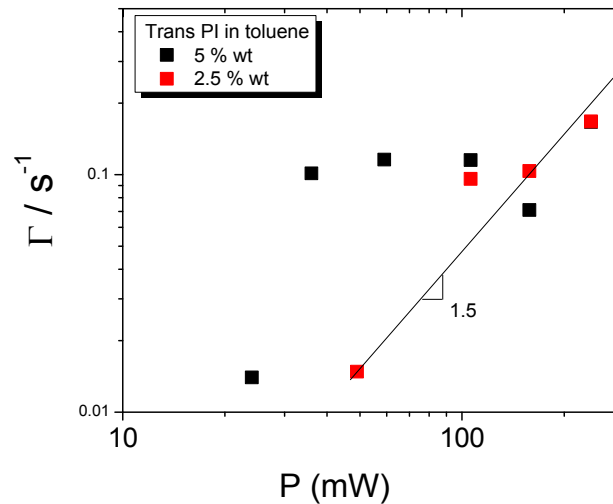
Figure 2.5: Dependence of the growth rate on laser power, for the two concentrations used (2.5% and 5% wt)

2.4 - Light-polydiene interactions in complex solutions

To further elucidate the role of the different parameter in the coupling between light and matter and extend the possibilities of pattern formation, we introduce copolymer based on polydienes, hoping that the rich phase diagram they exhibit in selective solvents may provide new insights. Moreover those materials are easily accessible, as they are industrially relevant and very much available from the rubber industry.

Transparent solutions

SBR in heptane

Styrene-butadiene rubber (SBR) is the name given to a variety of copolymer of styrene and butadiene. It is available industrially as an elastomer. The presence of styrene monomer that change the chain conformation compare to pure polybutadienes. In particular: change of solubility, change of viscoelasticity, different thermal behavior. The use of SBR also allows to further vary the microstructure and possibly to elucidate its effect and the re-

quired amount of 1,4 dienes as SBR has a variable vinyl (1,2) content . SBR-solution in hep-
tane were found to be "responsive" upon red light irradiation, with the formation of a self-
propagating fibrilar pattern.

Figure 2.6 shows the results obtained for SBR in heptane at 10% wt for three laser
powers. The filament like pattern formation was also observed in this solution. The shape of
the kinetic curve in non-exponential. The normalized intensity I_{max} in log-scale increases lin-
early with irradiation time for all laser powers. By fitting with exponential growth, the rate is
linear proportion of the laser power, with an exponent of 0.67, much smaller from poly-
dienes in alkane solution and even lower for the trans-PI discussed before. Slope below one
could denote constraints in the mobility of the polymer due to styrene blocks, which slows
down the growth kinetics.
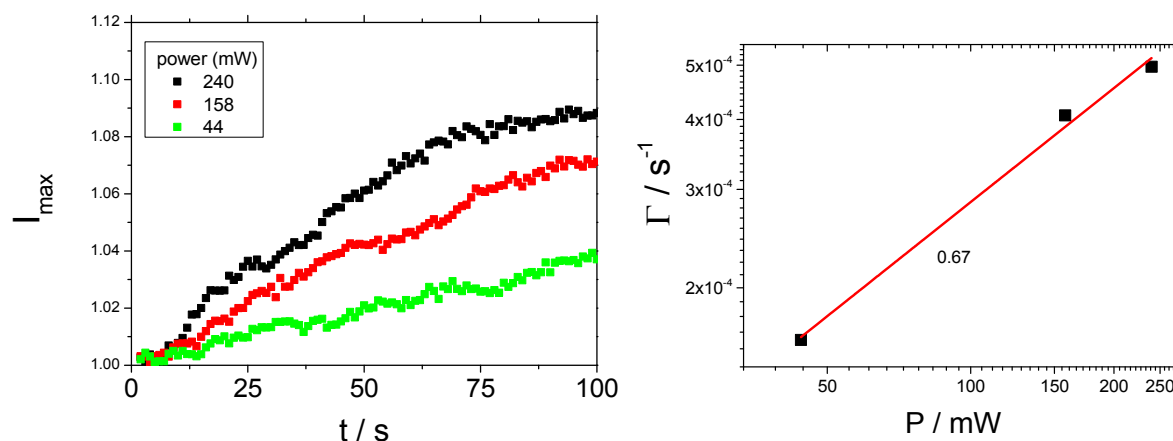
Figure 2.6 left: I_{max} vs. irradiation time for SBR in heptane (~10% wt) at different laser powers **right:**
Growth rate of the fiber formation obtained from the exponential growth fits, Γ vs. irradiation time

SIS in heptane

The triblock copolymer ABA type structure, gives the opportunity to affect the over-
all viscoelasticity of the solutions by varying the solvent and its selectivity between styrene
and isoprene. The triblock copolymer used consist of 16 % styrene equally distributed in the
two polymer ends. Heptane is a good solvent for polyisoprene and bad for polystyrene. We
expect the formation of supramolecular structures and at large enough concentration we
may expect the sample to have a gel-like behavior, due to attractive interaction between
the PS blocks and local aggregation acting as crosslink. (Watanabe, Sato et al. 1997) Confir-

mation of the formation of viscoelastic phases at low concentration (relative to the homo-polymer of similar M) is seen from the viscous aspect of the solutions and confirm by rheological measurement (Figure 2.7) where the response is essentially elastic ($G'>>G''$). Moreover the dynamic light scattering correlation function shows the occurrence of a clear non-ergodic plateau, typical of gel states. Figure 2.7 show the intermediate scattering function (ISF) and the dynamic frequency response (DFS) of SIS in heptane and decane at the concentration of 5% wt.
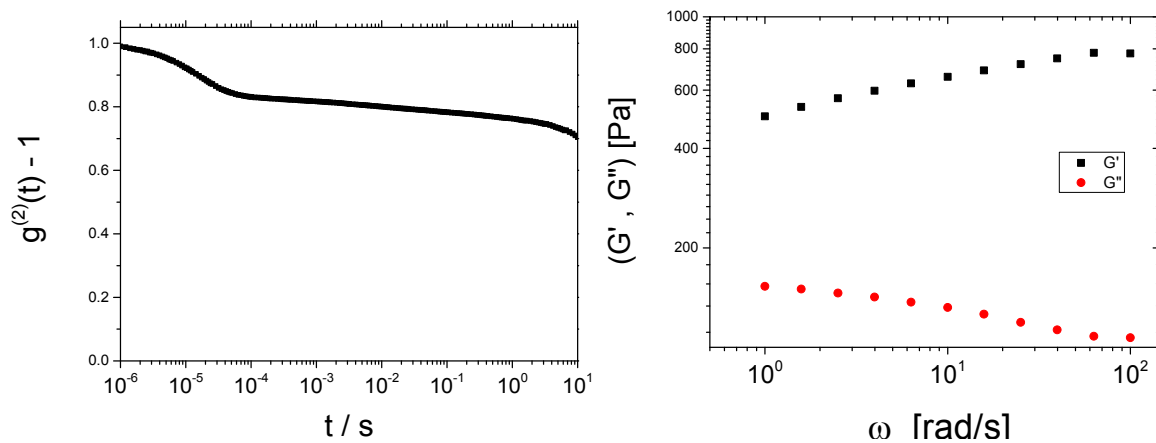
Figure 2.7 left: Intermediate scattering function for SIS (q=0.01949 nm^{-1}, T=20°C) in heptane at 5% wt **right:** Dynamic frequency sweep for PI in decane at c=5% wt (T=20°C)

In all cases formation of fibrilar structures were observed and the imaged contrast was found to increase with time. Figure 2.8 shows the maximum imaged intensity as a function of irradiating time for different concentrations and powers. The shape of the measured increase can not be described by an exponential growth as in the case of the simple homo-polymers discussed in previous studies (Anyfantakis, Loppinet et al. 2008, Anyfantakis, Loppinet et al. 2014). In both concentrations a waiting time is observed before the intensity growth. The waiting time seems to increase as we decrease the laser power. At lower concentrations, the growth formation exhibits power dependence. In the highest concentration the power dependence of the kinetics is limited, with only the lowest power being slower.
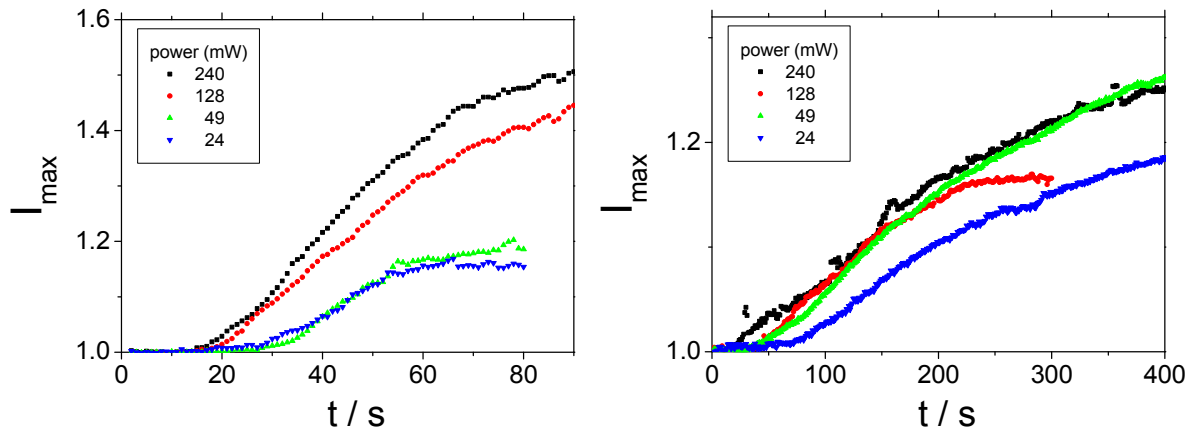
Figure 2.8: I_{max} vs. irradiation time for SIS in heptane at different laser powers. The concentration is 2% wt (**left**) and 10% wt (**right**)

Figure 2.9 depicts the growth rate of the fiber formation for different powers and three concentrations. At 10% wt the growth rate is power independent, similar to what has been observed for polydienes at very high concentrations. By lowering the concentration the rate increases linearly with laser power, with an exponent lower than one.
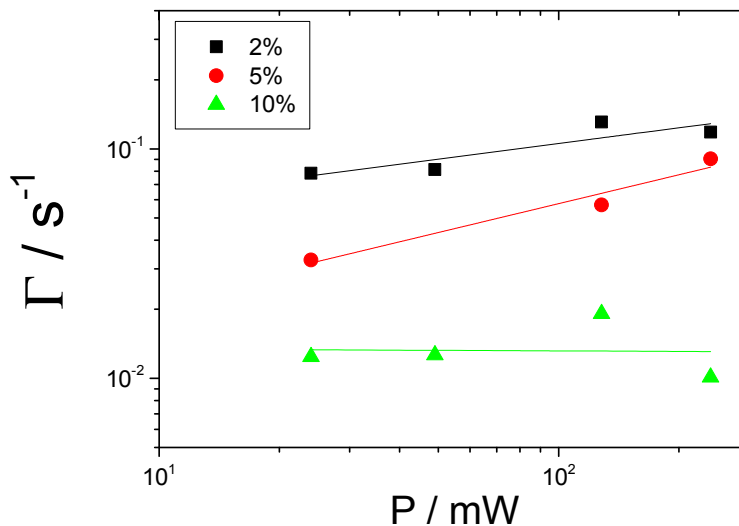
Figure 2.9: Growth rate of the fiber formation obtained from the exponential growth fits, Γ vs. irradiation time for three different concentrations.

SBR in Ethyl Acetate: "Negative" and transparent solution

We designate by negative case the appearance of a lower refractive index region in the original laser beam trace, which in most cases corresponds to a local decrease of polymer concentration. The red irradiation was shown to be able to create such "reverse" pattern in certain solvent condition, in particular when THF was used as a solvent.

Here we report the phase contrast observation using styrene-butadiene random copolymer in the same solvent (ethyl acetate). SBR remains soluble in EA, and transparent solutions are easily obtained (this is different from block copolymer, where solutions at RT are highly turbid as described below).

Figure 2.10 shows the observed effect of red-light irradiation on SBR in ethyl acetate at the concentration of 10% wt. Ethyl acetate is marginal solvent for PS and bad solvent for PI, resulting in more complex dispersions. The sample is somewhat turbid (T~40% over 10 mm path). We expect that strong scattering to originate from. Initially at early times, a lower refractive index stripe is created across the cell. In a later state the stripe broadens and eventually a conical shape at the exit of the shell appears. This resulted in a tubular structure which is evidenced along the beam direction. This effect is very similar to what had been observed recently in our group in polyisoprene solution in THF (Anyfantakis, Loppinet et al. 2012) . Most of the light is propagated along the beam direction, whereas part of the light is guided through the tubular donut-like structure, as seen from the microscopy side view and from the donut shape transmitted beam.

Figure 2.10: Real time phase contrast imaging of a turbid SBR in ethyl acetate (c=10% wt). Arrow denotes the laser beam direction.

SIS in Ethyl Acetate: "Negative" and turbid solution

As discussed before, the triblock SIS in solution has a very rich phase diagram. In particular solutions in EA are transparent and very fluid at temperature higher than ~55°C and undergo phase separation under cooling. The phase separation appears to almost arrest through some kind of gelation/percolation and does lead to a large turbidity that is distributed over the fool volume of the cell (see figure 2.11g). The solution remain turbid, we hardly observe any sedimentation over long period of times (days).

Both focused and defocused beam were shown to lead to an impressive patterning in the solution. Figure 2.10 shows the microscopy observation obtained for the defocused beam.

At concentration c=0.1 g/ml the sample is opaque and the transmission through the 1 cm cuvette is almost zero. By irradiating with a defocused red laser beam, the transmission increases with time and eventually a clear beam can be observed. At the same time the transmition shows a donut-like shape of the intensity, typical for a "negative" case. By looking at the phase contrast microscopy pictures (figure 2.10) at t=100s a large complex pattern formation seemingly consisting of multi-fibrilar fiber formation is observed, with the fiber size to be around 10µm. The formation propagates from the left to right, similar to the beam propagation and "drills" the sample, which at the end it forms a tubular structure. This tubular structure is confirmed by the appearance of a central spot in the transmission, evidence of a laser induced transparency.

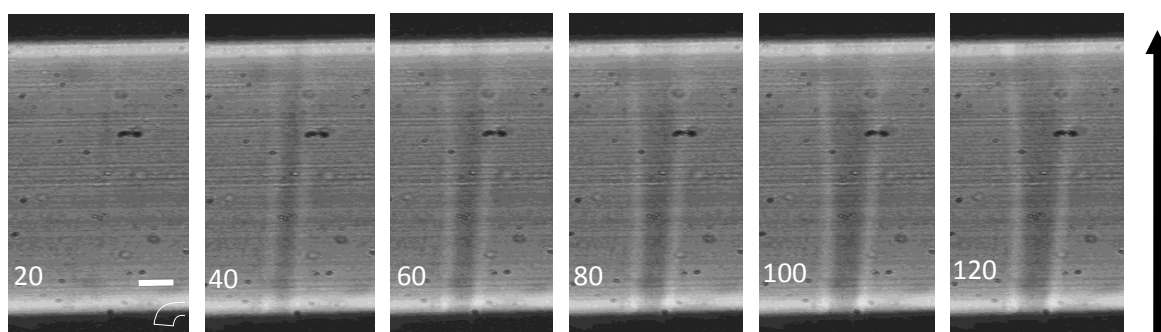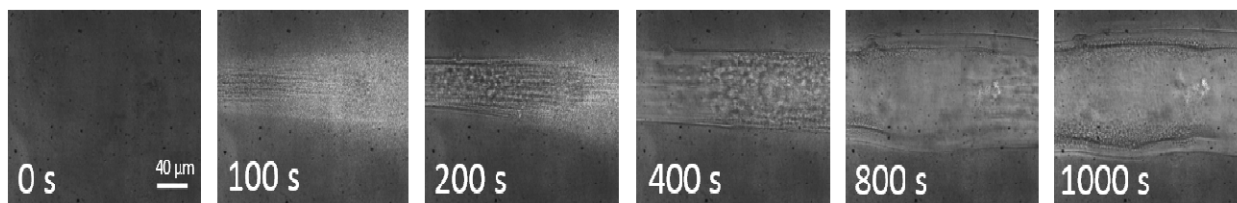**Figure 2.10:** Real time phase contrast imaging of a turbid SIS in ethyl acetate (c = 0.1g/ml). Arrow denotes the laser beam direction.

The details of the formed pattern view by optical means are shown in figure 2.11. The bright stripe in figure 2.11a show the region of the sample affected by the long-lasting

laser irradiation (~1 hour). One can clearly see that it goes all over the 1cm thick cell. The darker spot in Fig2.11 g shows the "exit" hole. A closer look in fig2.11e reveals the presence of at least two holes, with the small one shown in fig 2.11f. The side views Fig2.11 b,c,d reveal the tubular structure (c-d), and a skin-like formation which looks like a thin polymer film is surrounding the a central clear part . The higher magnification reveals some phase separated like pattern on the skin. The concentration of large flakes (which increase the turbidity of the sample) inside the tube is smaller from outside. At the exit of the beam, a clear hole is observed with an even smaller tube inside, with different transmissions (figure 2.10g and 2.10e-f).
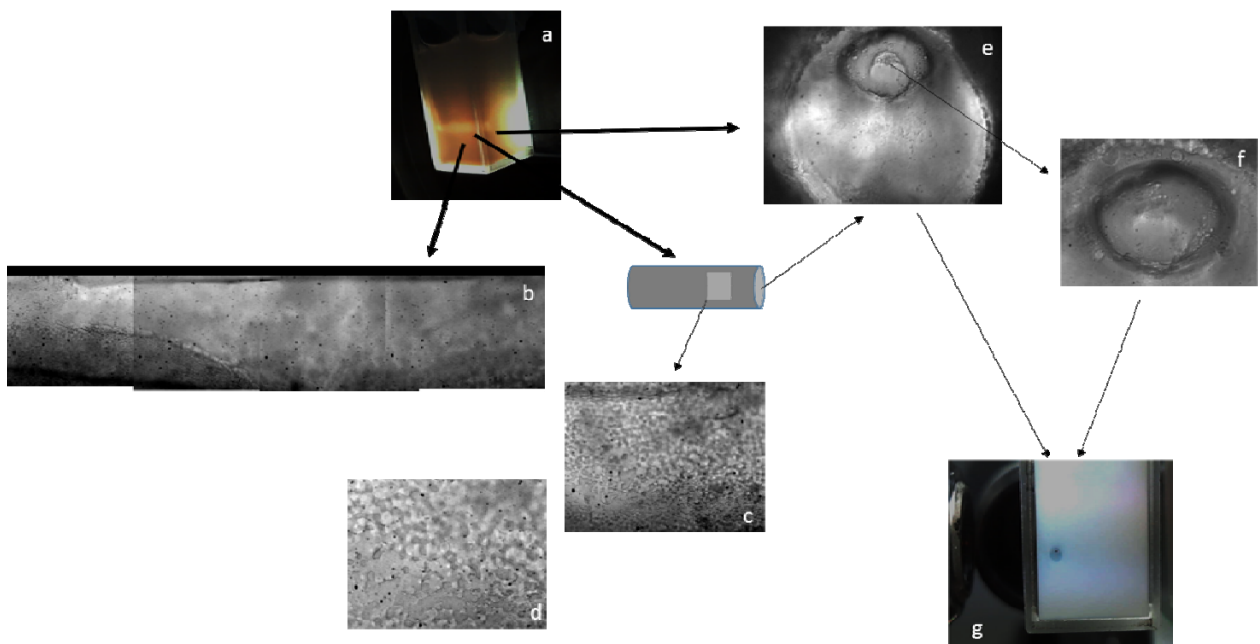
Figure 2.11a: Picture of SIS upon irradiation**.** The light yellow stripe corresponds to the tube-like structure formed by red laser**. b:** Phase contrast microscopy picture at 90° of the formed tube–like structure. **c-d:** magnification of the skin formed around the tube. **e-f:** the exit of the tubular structure. We observe two circles, one inside the other (**e-g**).

We can notice a large difference in the light transmission when propagating inside the tubular structure in what appear to be clear solution or outside in the turbid solution. Possible explanation of the phenomenon is the following: Upon red laser irradiation the clusters/flakes inside the sample "melt" and the solution become clear. Moreover the irradiated material forms a solid skin around the beam probably through cross-linking. Since the beam "melts" the clusters, the transmission in increased creating a tubular structure with less tur-

bidity. Radiation pressure could be also a possible force for the induce transparency due to the large micron sized clusters formed, but no significant flow is observed along the beam direction.

2.5 – Conclusion

The presented results lead us to the following conclusion:

i) the size of the individual fiber formed are very constant in all samples,

ii) The formation kinetics is not identical for all samples, unlike homopolymer solutions, the exponential growth that was found to satisfactorily describe the contrast increase in most of the homopolymer does not provide a good fit for the measured growth in the more complex samples. Deviation are observed, with sometimes "incubation" time, during which no pattern formation is observed (trans-PI, chemically crosslinked gels) or linear like growth in elastic samples. This variety probably reflects the difference mechanism in the different samples and possibly an influence of sample architecture and conformation on the kinetics of formation.

iii) a clear laser power dependence of the rate apart from the highest volume fractions where there is no power dependence,

The presence of excess antioxidant does not affect much the formation and its kinetics. This can be taken as a proof that photo-oxidation of the dienes, which the antioxidant is supposed to prevent, is not that relevant for the process.

This is enhanced from experiments performed in more complex structures like SBR where the cis-1,4 content is small, that participate to this phenomenon.

The appearance of the pattern even in the crosslinked material is an evidence that the fiber forms through the participation of local chains. It does not require large scale motion. In a swollen gel, the local polymer concentration can increase, through local contraction of the gel and de-swelling (but it cannot decrease, unless some crosslink points are broken). This also partially answers the question whether flow is necessary during the writing process. This result together with the experiments polybutadiene-gold solutions, provide evidence that flow is not a necessary condition, it does not have to be present.

By increasing the complexity, moving to diblock (SBR) or even triblock (SIS) architectures, the power dependence of the growth rate is less than the linear dependence observed in cis-polyisoprene or polybutadienes solutions. This strong decrease of the slope can tentatively be attributed to local constrains of the chain due to partial solubility of the chain in the solvent and the complex architecture they exhibit (acting as physical crosslink in the solutions). At the concentration of 10% wt in SIS the rate of formation is constant with laser power similar to what we have observed previously at different systems.

Whereas the positive case (increase of polymer concentration in the irradiated part) can tentatively be explained by a local crosslinking mechanism initiated by the light, it seems at first sight, difficult to account for the negative case with such a mechanism.

An explanation for the negative case could be a sequential formation starting with the local formation of a crosslink region that produces to a cone of light then we could have the formation of cross-link in this cone of light, and formation of a tubular sheet like cross-linked material pattern.

It is not presently easy to tell why one solvent response should be that direction or this direction. It could be that the early stage of the process is more active and lead to a faster formation than then will not lead to the self-focusing needed for the filament base self-propagation. Such variation of patterning have been reported in photorefractive polymer (at least to some extend in the transmission pattern (Villafranca and Saravanamuttu 2008)). The variation of the laser power can lead to large variation in the kinetics of formation, and that can be rationalize assuming a saturable process (the refractive index can only increase to a maximum value). The analogy may not be straightforward and this proposal will needs to be further cross-checked, but we clearly observed the formation of an irreversible "solid like" pattern, and it is probably obtained through the same mechanism than the "positive" fibers. Spectroscopic characterization will help to confirm the scenario.

Through the use of SIS / SBR copolymers we saw that the patterning is kept down to relatively low 1,4-diene content in SBR and also down to very low monomer concentration . The presence of styrenes monomer does not seem to affect much the effect (this is compatible with a diene cross-linking mechanism that should remain present independently of the presence of copolymers). Overall SIS and SBR showed the same trends, similar to PI or PB

In the case of solutions in ethyl acetate (we recall that pure PI or PB are not soluble in EA), both SIS and SBR exhibit the "negative" effects. Moreover SIS can be made very tur-

bid, and red light irradiation exhibit there a spectacular case of induced transparency. The mechanism that could create this induced transparency is still unclear, yet it has to be connected with what creates the turbidity in the first place. Turbidity arises from a phase separation that is almost arrested through some kind of gelation. Maybe the laser irradiation and the dienes-related effect is large enough for the phase separation to proceed further to a less turbid later stage (that could explain the large droplets observed through microscopy). More work needed to identify the proper mechanism.

2.6 – References

Anyfantakis, M., B. Loppinet, G. Fytas, C. Mantzaridis, S. Pispas and H.-J. Butt (2012). "Self-induced transparency in diblock copolymer dispersions." Optics Letters **37**(13): 2487-2489.

Anyfantakis, M., B. Loppinet, G. Fytas and S. Pispas (2008). "Optical spatial solitons and modulation instabilities in transparent entangled polymer solutions." Optics Letters **33**(23): 2839-2841.

Anyfantakis, M., B. Loppinet, A. Pamvouxoglou, G. Fytas, S. Pispas and C. Mantzaridis (2014). "Kinetics of the concentration optical nonlinearity in polydiene solutions." in preparation.

Sigel, R., G. Fytas, N. Vainos, S. Pispas and N. Hadjichristidis (2002). "'Pattern Formation in Homogeneous Polymer Solutions Induced by a Continuous-Wave Visible Laser'." Science **297**: 67-69.

Villafranca, A. B. and K. Saravanamuttu (2008). "An Experimental Study of the Dynamics and Temporal Evolution of Self-Trapped Laser Beams in a Photopolymerizable Organosiloxane." The Journal of Physical Chemistry C **112**(44): 17388-17396.

Watanabe, H., T. Sato, K. Osaki, M.-L. Yao and A. Yamagishi (1997). "Rheological and Dielectric Behavior of a Styrene–Isoprene–Styrene Triblock Copolymer in Selective Solvents. 2. Contribution of Loop-Type Middle Blocks to Elasticity and Plasticity." Macromolecules **30**(19): 5877-5892.

Appendix: Experimental Techniques

1– Raman

The technique of Raman spectroscopy owes its name to the Indian scientist Chandrasekhara Venkata Raman (1888-1970), among the founders of scientific research in India, and Asia's first Nobel Prize winner in science.

Raman spectroscopy probes molecular vibrations and therefore is sensitive to the chemical environment of the sample material. When light hit matter, the electric field of light induces a dipole moment μ in the molecule due to polarizability, α, according to

$$\mu = \alpha E \tag{1}$$

where **E** is the Electric field

Due to the oscillation of the electric field, the dipole moment of the molecule also oscillates. Through the energy transfer from photons of the incident light to molecules, the latter can be excited to their higher energy levels, by emitting the scattering light. The energy transition can be either elastically (Rayleigh scattering) or inelastically, giving rise to emitted photons of energies either higher or lower that of the incoming light; this is what we called Raman effect. The photons emitted at the lower energy, $h\nu_o$-$h\nu_1$, are called Stokes Raman photons. The energy difference $h\nu_1$ arises from the energy lost from the incoming photons to promote the molecule into an excited vibrational level of the ground electronic state. Anti-Stokes Raman photons appear at the same energy difference in relation to the excitation line, but on the high-energy side of the Rayleigh photons. The intensities of Anti-Stokes Raman bands are very weak. In the most of the cases the Raman spectra reported include only the Stokes portion (Tanaka and Young 2006).

If a molecule is vibrating with a certain frequency, the displacement of the k-th atom in the molecule from its equilibrium position can be written by

$$q_k = q_k^0 \cos(2\pi\nu_m t) \tag{2}$$

where q_k^0 *the amplitude of the displacement, and* ν_m is the frequency of the vibration. The polarizability *a* of the molecule can be expanded in the form of Taylor series
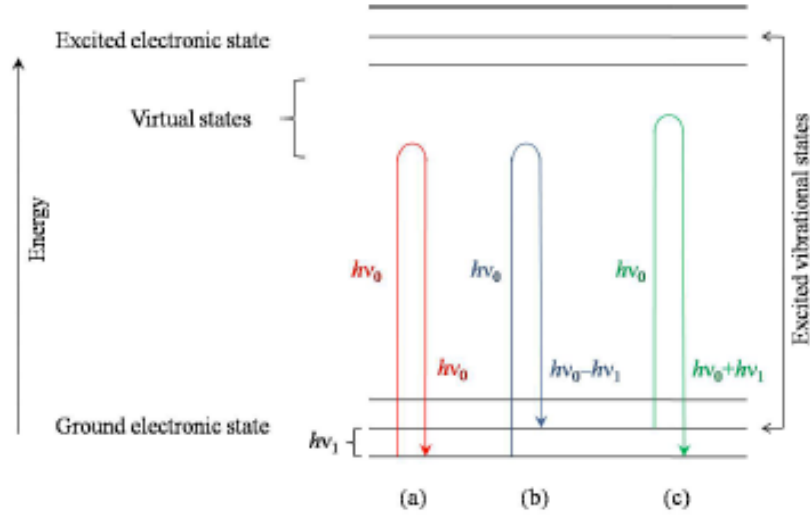
Figure 1.1: Schematic representation of the (a) Rayleigh, (b) Stokes Raman and (c) anti-Stokes Raman scattering effect

$$\alpha = \alpha_0 + \sum_\kappa \left(\frac{\partial\alpha}{\partial q_k}\right)_{q_i=0} q_k + \frac{1}{2}\sum_{i,j}\left(\frac{\partial^2\alpha}{\partial q_i \partial q_j}\right)_{q_i=0} q_i q_j + ... \tag{3}$$

The displacement q_k concerning the molecular vibration is considered to be very small, and the high order terms (from the 3rd term in the right-hand side of the equation and above) can be neglected. The combination of the above equations gives

$$\mu = \alpha_0 E_0 \cos(2\pi\nu_0 t) + \sum_\kappa \left(\frac{\partial\alpha}{\partial q_k}\right)_{q_i=0} q_k E_0 \langle \cos[2\pi(\nu_0 - \nu_m)t] + \cos[2\pi(\nu_0 + \nu_m)t]\rangle \tag{4}$$

In **Equation 4**, the first term is related to the Rayleigh scattering, while in the second term, the part containing ($v_o - v_m$) is related to the Raman scattering for which the vibrational energy of the molecule moves to a higher energy level than its initial energy level (Stokes Raman scattering). In contrast, the scattering with the vibrational energy transition of the molecule from its initial energy level to a lower energy level (anti-Stokes Raman scattering) is related to the part with ($v_o + v_m$). It can be easily realized that the condition for a vibrational mode to be Raman active is shown by

$$\left(\frac{\partial \alpha}{\partial q_k} \right)_{q_k = 0} \neq 0 \tag{5}$$

which indicates that the molecular polarizability of the vibrational mode should be neither maximum nor minimum when the atoms are at their equilibrium positions (Long 2005).

The experimental setup used during this study (Nicolet Almega XR Raman spectrometer) is based a confocal microscope. A LASER beam (λ = 780 nm, P = 15 mW) is focused on a micron-sized spot in the sample through a microscope objective of high numerical aperture. Light scattered from this spot in backward direction is collected and collimated by the same objective lens. The Rayleigh line is blocked by an appropriate notch filter. The different frequency components of the inelastically scattered light are dispersed in a monochromator, whose entrance slit is replaced with a pinhole. A CCD detector is placed in its exit focal plane so the whole Raman spectrum is recorded (Smith and Dent 2005). Due to the confocal scheme, only light from the focus can penetrate through the pinhole; light from other depths in the sample is efficiently blocked. As a consequence, out-of-focus regions do not blur the signal, but are dark. A schematic of a typical micro-Raman setup is shown in **Figure 1.2**:
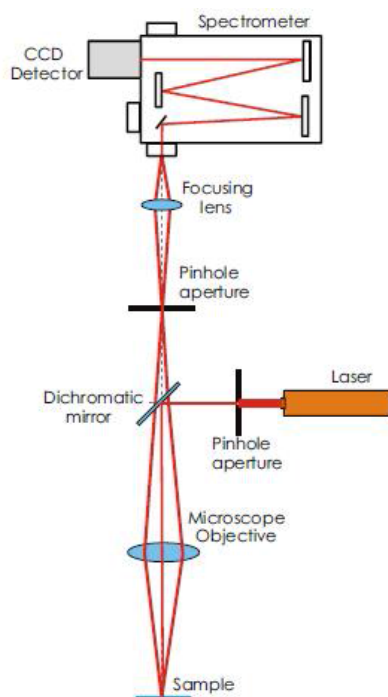
Figure 1.2 : Schematic representation of a typical micro-Raman setup

2 – Electron Paramagnetic Resonance (EPR)

Electron paramagnetic resonance (EPR) or electron spin resonance (ESR) spectroscopy represents a technique for studying systems which have at least one unpaired electron in their composition. The principle behind this technique is the interaction between the unpaired electron spin with an external magnetic field. When subjected to an external uniform magnetic field, the absorption of electromagnetic radiation by molecules with unpaired electrons gives rise to transitions between energy levels that are degenerate in absence of the field, but become split in its presence, the splitting being proportional to the field strength. The transitions between these levels are evidenced by subjecting the sys-

tem to another magnetic field (an oscillating one, and perpendicularly oriented with respect to the uniform field) if a resonance condition is satisfied. The existence of minimum one unpaired electron is crucial, and since most stable molecules exist in singlet state (having all their electrons paired), the applicability of EPR techniques is reduced. This limitation may be viewed as an advantage, since it allows the study of specific molecules enclosed in otherwise EPR silent materials, provided the life-time of the unpaired electron is long enough.

In EPR spectroscopy the radiation used is in the Gigahertz range. Unlike most traditional techniques, in EPR spectroscopy the frequency the radiation is held constant while the magnetic field is varied in order to obtain the absorption spectrum. Figure 2.1 shown a typical EPR spectrometer. The Spectrometer we used was operating at 9.5 GHz with a magnetic field of 0.34 Tesla with the radiation to be continues. The sample is placed in a resonant cavity which admits microwaves through a hole. The cavity is located in the middle of the Helmholtz coils and helps to amplify the weak signals of the incident microwave photons. Moreover other components such as field modulator, amplifier and attenuator are also included to enhance the signal.

When an electron is placed within an applied field, B_o, the two possible spin states of the electron have different energies. The lower energy state occurs when the magnetic moment of the electron is aligned against the magnetic field and a higher energy state where m is aligned against the magnetic field. The two states are labelled by the projection of the electron spin, M_s, on the direction of the magnetic field, where M_s = -1/2 is the parallel state and M_s = +1/2 is the antiparallel state.
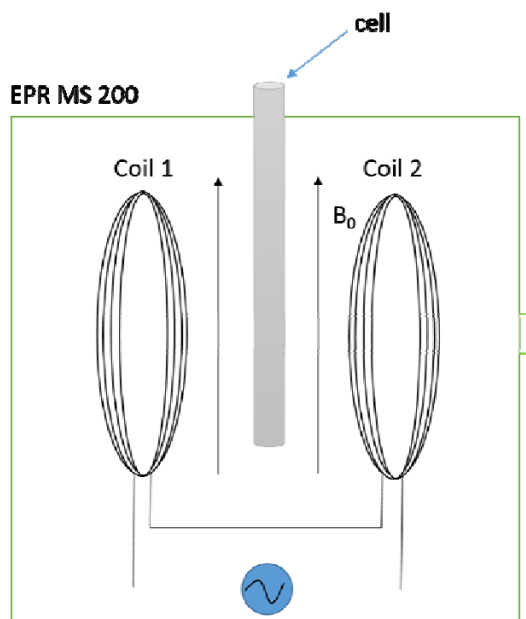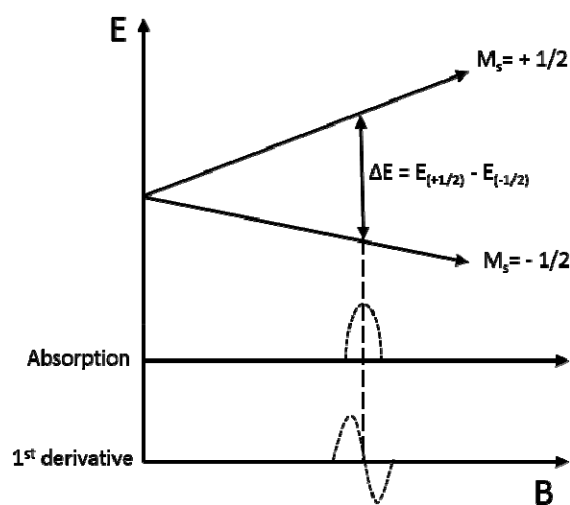
Figure 2.1: Sketch of a typical EPR setup.

Figure 2.2: Energy levels for an electron spin ($M_S = \pm 1/2$) in an applied magnetic field. Absorption and 1st derivative of the absorbed microwave radiation.

Like most spectroscopic techniques, when radiation is absorbed, a spectrum is produced similar to figure 2.2. In the EPR spectrometers a phase-sensitive detector is used which results in the absorption signal being presented as the first derivative. The absorption maximum corresponds to the point where the spectrum passes through zero, which also determines the centre of the signal.

For a molecule with one unpaired electron in a magnetic field, the energy states can be defines as:

$$E = g\mu_B B_0 M_S = \pm\frac{1}{2}gm_B B_0 \tag{6}$$

Where g is the proportionality factor (g-factor), μ_B is the Bohr magneton, B_0 is the magnetic field, and M_S is the electron spin quantum number. At $B_0=0$, the two spins states have the same energy. Moreover the difference between the two spin states increases linearly with increasing magnetic field strength. Absorption occurs when the magnetic field "tunes" the two spin states so that their energy difference is equal to the radiation. The g-value depends on the surrounding environment of the electron. In our case we observe free electrons and the g-value is 2.00232 at 9.3GHz frequency and 335 mT magnetic field.

Additional information can be obtained from the so-called hyperfine interaction. The nuclei of the atoms in a molecule or complex usually have their own fine magnetic moments. Such magnetic moments occurrence can produce a local magnetic field intense enough to affect the electron. Such interaction between the electron and the nuclei produced local magnetic field is called the *hyperfine interaction*. Then the energy level of the electron can be expressed as:

$$E = g\mu_B B_0 M_S + \alpha M_S m_l \tag{7}$$

In which *a* is the hyperfine coupling constant, m_l is the nuclear spin quantum number. Hyperfine interactions can be used to provide a wealth of information about the sample such as the number and identity of atoms in a molecule or compound, as well as their distance from the unpaired electron.

The rules for determining which nuclei will interact are the same as for NMR. For isotopes which have even atomic and even mass numbers, the ground state nuclear spin quantum number, I, is zero, and these isotopes have no EPR (or NMR) spectra. For isotopes with odd atomic numbers and even mass numbers, the values of I are integers. For example the spin of ^{2}H is 1. For isotopes with odd mass numbers, the values of I are fractions. For example the spin of ^{1}H is 1/2.

The number of lines from the hyperfine interaction can be determined by the formula: $2NI + 1$. N is the number of equivalent nuclei and I is the spin. When coupling to a single nucleus, each line has the same intensity. When coupling to more than one nucleus, the relative intensity of each line is determined by the number of interacting nuclei. For the most common I=1/2 nuclei, the intensity of each line follows Pascal's triangle, which is shown in figure 2.3a. For •CH$_3$, the radical's signal is split to $2NI+1= 2*3*1/2+1=4$ lines, the ratio of each line's intensity is 1:3:3:1 figure (2.3b).
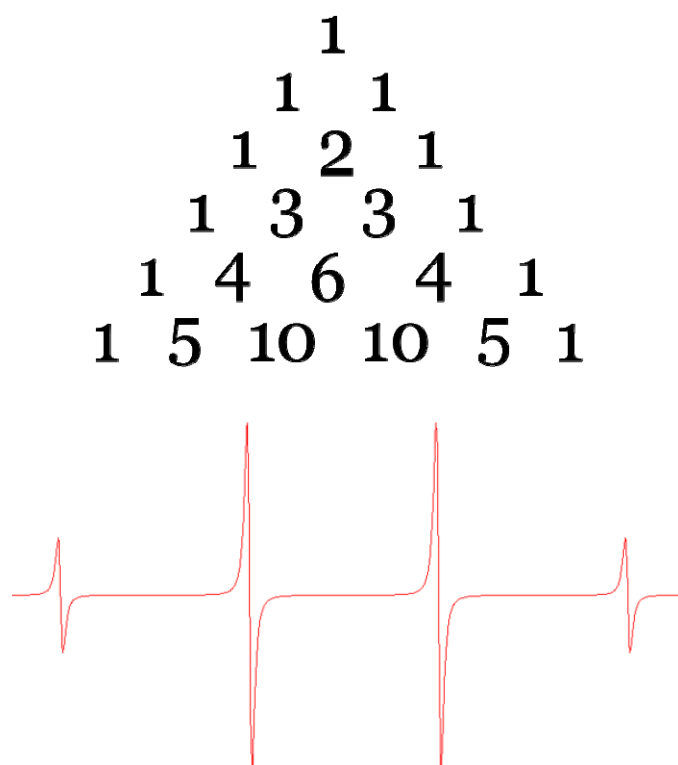
Figure B2.3: a)Pascal's triangle b) EPR spectrum of •CH$_3$ radical

The systems studied in the thesis are Polyisoprene solutions at high concentrations ($c >> c*$). The appearance of free radicals is due to the double bond breaking in the main backbone. This results into two freely rotating groups, with the tertiary group of (CH2-**C**-CH2-CH) to be observed from EPR, since the relaxation of (H-**C**-CH2-CH) is very fast (figure 2.4). The four peaks observed in the spectra correspond to the methyl groups appeared in the polyisoprene and the doublets are due to the methyl groups that are attached next to the carbon that was connected with the double bond.
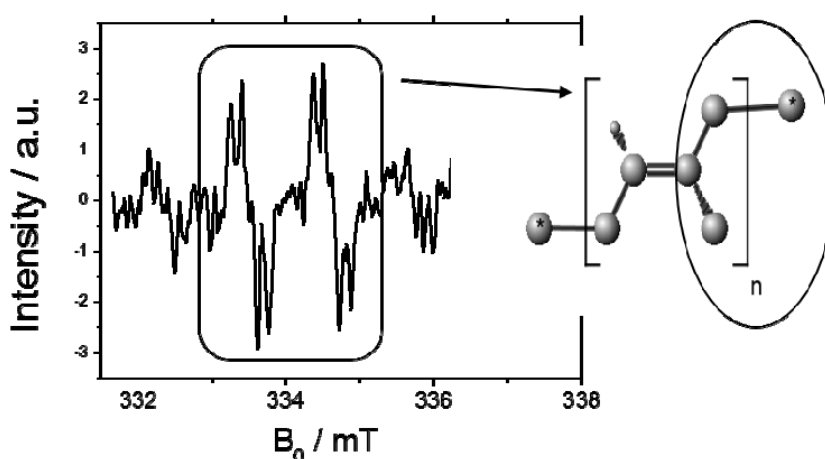
Figure 2.4: Typical EPR diagram of Polyisoprene solution upon laser irradiation. The circle on the molecule denotes the tertiary part, which is measured by EPR.

3 - Phase Contrast Microscopy

The experimental setup for pattern formation and simultaneous imaging of the light- induced structures consists of two basic parts. The one part is a typical upright optical microscope (Zeiss Axioskop 2). The second part is a metallic plate attached to the microscope stage, containing the optical and mechanical elements. As depicted in Fig-

ure 3.1, a CW LASER source (λ= 671 nm, P = 240 mW) is placed on the plate. The LASER beam is guided through two mirrors (M1 and M2) to a 4x microscope lens (W, focal length, f = 35 mm, NA = 0.12), and is focused in the middle of the glass cell which contains the sample. The incident power on the sample cell was varied between 240 to 10 mW by using a stepped optical filter.
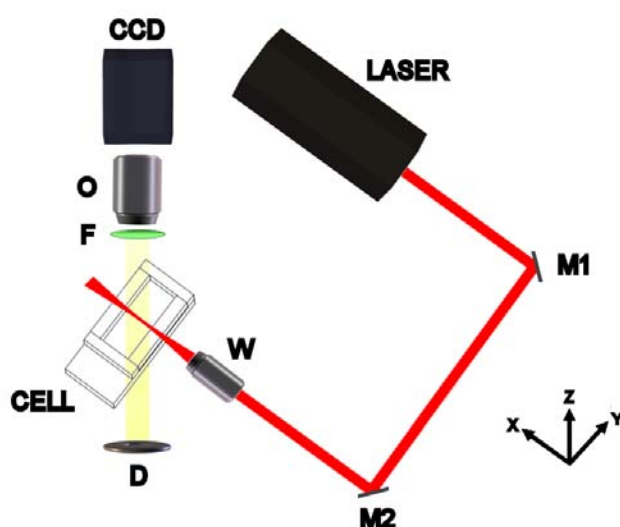
Figure B3.1: A schematic of the experimental setup for creating and simultaneously imaging the light-induced patterns.

The beam diameter at the focal spot is roughly 28 μm and was set at the entrance of the glass cell. The sample cell is mounted on an x, y, z-translation stage, giving the ability to irradiate different sample positions.

Utilizing the above setup, someone can observe the writing phenomenon in all the three ways described in the introduction. The transmitted LASER beam is projected to a screen. This allows detection of the changes occurring to the shape of the spot during irradiation. Moreover, the scattered LASER light during pattern formation can be detected through the objective lens and the CCD camera that is attached on the microscope. Finally, by means of white light Kohler illumination and by using the bandpass

filter F (which blocks the LASER light), real time imaging of the structures can take place. The illumination and imaging conditions will be described in detail in the next Section.

Quantitative Phase Contrast Microscopy

In order to quantify the local refractive index variation induced by the laser illumination, we used quantitative phase contrast microscopy. The technique is simple and particularly well suited for the cylindrically symmetric patterns formed. In the following, we briefly describe the procedure followed to obtain the refractive index contrast of the formed pattern.

A collimated white light beam combined with a slightly out of focus microscopic detection leads to an image where the intensity can be quantitatively related to the refractive index alteration. This variant of quantitative phase contrast imaging has been developed in the recent years by the group of K. Nugent (Barty, Nugent et al. 1998, Barone-Nugent, Barty et al. 2002). It provides an easy way to measure low refractive index differences, especially for objects with cylindrical symmetry like optical fibers.

The following relation between the imaged intensity and the refractive index variation had been obtained (Barty, Nugent et al. (1998) using intensity propagation formalism:

$$\frac{\partial I(z)}{\partial z} = -\frac{\lambda}{2\pi} I(\Delta z = 0) \vec{\nabla}^2 \phi(\vec{r}) \qquad (8)$$

using the relation for the wavenumber, k_0, $k_0 = 2\pi/\lambda$ leads to the following relation:

$$-\frac{k_0}{I(z=0)} \frac{\partial I(z)}{\partial z} = \Delta_{x,y} \phi = \frac{\partial^2 \phi}{\partial y^2} \qquad (9)$$

where z is along the propagation axis of the microscope illumination light and the gradient is along the radial dimension of the cylindrically symmetric object observed. I is the intensity measured on the CCD for a defocusing distance Δz. The filament direction defines the x-axis. Due to the relatively small refractive index variation, the in-focus image is almost feature less and therefore

$$\frac{\partial I(z)}{\partial z} \approx \frac{\Delta I(z)}{\Delta z} \tag{10}$$

Within the mentioned approximations, the imaged intensity is directly proportional to the Laplacian of the phase and the gradient of the phase is related to the gradient of refractive index, through an Abel transform(Barty, Nugent et al. 1998):

$$k_0 n(r,x) = -\frac{1}{\pi} \int_r^R \frac{\partial \phi}{\partial y} (R^2 - y^2)^{1/2} dy \tag{11}$$

It is possible to compute the refractive index profile from the image by an inverse Abel transform of the phase gradient. The full treatment requires an inverse Fourier transform and an inverse Abel transform. We here used a simplified approach well suited for the cases of interest, where a Gaussian functional form for the refractive index profile is assumed:

$$n(r,t) = n_0 + \delta n \exp(-r^2/a^2) \tag{12}$$

In that case, imaged intensity at de-focus distance Δz, $I(y, \Delta z)$, can be easily calculated analytically through the Laplacian of the Abel transform of the refractive index profile .

$$\frac{I_z(y)/I_0}{\Delta z} = \frac{\partial}{\partial x^2} \left(2 \int_y^\infty \frac{k_0 n(r) r \, dr}{\sqrt{r^2 - y^2}} \right) \tag{13}$$

$$= 2a \delta n \sqrt{\pi} \frac{\partial \left(\exp(-y^2/a^2) \right)}{\partial x^2} = \frac{4}{a} \delta n \sqrt{\pi} \left(1 - \frac{2y^2}{a^2} \right) \exp(-\frac{y^2}{a^2}) \tag{14}$$

The functional form (3.7) provided a decent fit of the imaged intensity.

In (13), the maximum of the measured intensity is observed at the centre of the pattern (*y*=0) and it could be directly related to the refractive index increment δn and the filament transverse dimension *a*. Moreover in the cases reported below, the dimension *a* was observed to be independent of time, (*a*(*t*) = *a*) and the maximum of intensity I_{max} provided a direct measurement of the refractive index increment δn:

$$\delta n = \frac{1}{4\sqrt{\pi}} \frac{a}{\Delta z} \left(I_{\max} - 1 \right) \tag{15}$$

The validity of this simplified approach was further assessed through a comparison with the full quantitative approach(Papazoglou and Tzortzakis 2008), which confirmed the validity of the Gaussian profile.

The sensitivity and range of the technique as implemented here is limited by the relatively low dynamic range of the used CCD camera (8 bit). The smallest measurable intensity variation is of the order of 1% that would correspond to a refractive index change of δn ~ 10-4. For a constant illumination (as used during a measurement) and with a starting uniform intensity of the order 50 counts, the maximum measurable intensity is a factor of 2 larger. It corresponds to maximum refractive index increase of the order of δn~3.5x10^{-2} assuming *a*=5 μm (fiber radius) and Δz=20 μm (typical defocusing distance used). In addition, the maximum weight fraction increase δc=δn/(dn/dc) is of the order of δc~0.27 g/ml, for a refractive index increment d*n*/d*c*~0.13 ml/g. This simple implementation of the quantitative phase contrast provided the precision required for this study.

4 - References

Barone-Nugent, E. D., A. Barty and K. A. Nugent (2002). "'Quantitative Phase-Amplitude Microscopy I: Optical Microscopy'." J. Microsc. **206**: 194–203.

Barty, A., K. A. Nugent, D. Paganin and A. Roberts (1998). "'Quantitative Optical Phase Microscopy'." Opt. Lett. **23**: 817-819.

Long, D. A. (2005). "Introductory Raman Spectroscopy. John R. Ferraro, Kazuo Nakamoto and Chris W. Brown. Academic Press, Amsterdam, Second Edition, 2003. xiii + 434." Journal of Raman Spectroscopy **36**(10): 1012-1012.

Papazoglou, D. G. and S. Tzortzakis (2008). "'In-line Holography for the Characterization of Ultrafast Laser Filamentation in Transparent Media'." Appl. Phys. Lett. **93**: 041120.

Smith, E. and G. Dent (2005). Modern Raman Spectroscopy: A Practical Approach, Wiley.

Tanaka, M. and R. J. Young (2006). "Review Polarised Raman spectroscopy for the study of molecular orientation distributions in polymers." Journal of Materials Science **41**(3): 963-991.

Part II

Structure and dynamics in suspensions and glasses of soft colloids

Chapter 3   Structure and Dynamics in Concentrated Suspensions of Soft Colloids

3.1 - Introduction

It is very interesting to look whether polymers and colloids, two very important categories in soft condensed matter, show common behavior in the liquid regime. The dynamics of polymers and colloids with changing the concentration exhibit interesting phenomena, which are dictated by the hydrodynamic interactions mediated through solvent molecules (Stellbrink, Allgaier et al. 1997, Sigel, Pispas et al. 1999, Petekidis, Gapinski et al. 2004, Loppinet, Fytas et al. 2005, Pamvouxoglou 2006, Eckert and Richtering 2008, Gapinski, Patkowski et al. 2009, Voudouris, Choi et al. 2009). These open issues provide a good motivation to experimentally study model systems with both polymer and colloid character. Well-studied systems with intermediate properties are particles which have spherical cores and end-grafted polymer chains as corona. By varying the number of arms these systems exhibit either colloidal (highly grafted small polymer chains) or polymeric behavior (highly grafted big polymer chains) (Vlassopoulos, Fytas et al. 2001, Pamvouxoglou 2006, Voudouris, Choi et al. 2009).

For hard sphere systems, the short-time dynamics around the peak of S(Q) are slowed down as we increase the volume fraction, evidence that thermodynamic and hydrodynamic interactions are affected (Pusey and Tough 1985, Megen and Underwood 1993). For charged colloidal particles (Gapinski, Patkowski et al. 2009) which are effectively described by a soft repulsive interparticle potential, they report the appearance of a slowdown of the dynamics near the peak of S(Q) and can be fitted with theoretical models (Banchio and Nagele 2008, Gapinski, Patkowski et al. 2009). Microgel particles examined by Richtering et al.(Eckert and Richtering 2008) showed a strong slowing down of the dynamics around the peak of S(Q) similar to the HS

83

despite the "fuzzy" particle surface, whereas for core-shell particles examined by Petekidis et al.(Petekidis, Gapinski et al. 2004) this slowdown of D(Q) around the peak of S(Q) is much weaker. Reports in diblock copolymers are controversial. In giant PS-PI micelles studied by Siegel et al. (Sigel, Pispas et al. 1999) there is no additional slowing down of D(Q) near peak of S(Q). Note that a study on similar SI block copolymer in equally good solvent, forming microphase separated states by Chrissopoulou et al. (Chrissopoulou, Pryamitsyn et al. 2001) indicated an additional slowing down near the peak of S(Q) to be strong, as expected by theory.

In hard spheres, by increasing volume fraction the short-time self-diffusion become slower as it is predicted by Brady et al. (Banchio and Brady 2003) approaching glass transition through Accelerated Stokesian Dynamic (ASD) simulations. For soft spheres reported by Voudouris et al. (Voudouris, Choi et al. 2009) where the particles are coated with shorter end-grafted polymer chains, the structure and dynamics were close to Hard Sphere behavior whereas for long grafted polymer chains, they are deviations due to softness.

3.2 - Method

3.2.1 - Materials

The hybrid particles (PMMA-SiPs) were synthesized by surface-initiated atom transfer radical polymerization (ATRP) of MMA, as reported previously (Ohno, Morinaga et al. 2005). The mean diameter of the SiP were 130 nm with a relative standard deviation of 10%, as measured by transmission electron microscopy. These particles have SiP core and PMMA shell chains, having weight-average molecular weight $\overline{M_w}$ 126 (**P2_126k**) and 402 kg/mol (**P2_402k**) with polydispersity index (PDI) 1.24 and 1.15 respectively. The surface density of the SiP is 0.65 chain/nm². This means that both particles have 34500 grafted chains per particle. Knowing the weight fraction of PMMA in the hybrid particle and literature value of the density f of PMMA and SiP in the bulk, the calculated overall (average) density of the PMMA-SiP 126k and 402k hy-

brid particles to be 1.33 and 1.24 respectively. 1,2-Dichloroethane (50% vol) and o-dichlorobenzene (50% vol) were used to prepare index matching solvents. For the particles with higher chain molecular weight (402k) a mixture of o-dimethoxy benzene (veratrole) and Dimethyl Formamide (DMF) were used to refractive index match (n=1.489) the shell at λ=633 nm. In P2_402k we also prepare solutions in toluene, a good solvent for PMMA. The polymer is more extended compared with solvent mixture and the hydrodynamic radius was increased, and the surface density in the outer blob was decreased.

In order to observe the phase diagram, we prepared several samples in quartz square cell of 4mm thickness. The protocol used for these experiments was the dispersion of the sample in the desired volume fraction. The sample was at constant temperature for two days before visual observation tests were performed. The results for P2_126k are shown in the sketch below.
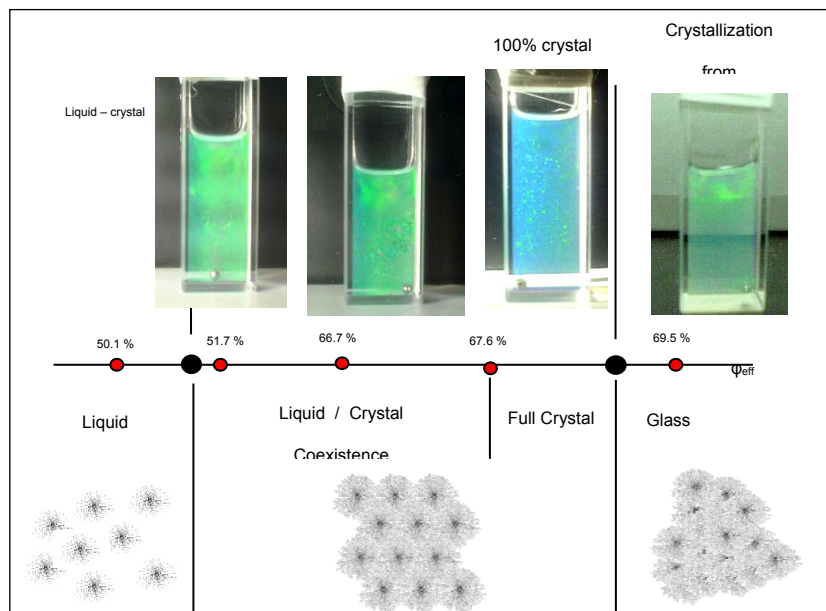
Sketch 3.1: Phase diagram of P2_126k in 50-50 solvent.

For the calculation of the effective volume fraction (c/c*) we took into account the hydrodynamic radius, with $\varphi_{eff} = \dfrac{c}{c*(R_H)}$; where $c*(R_H)$ is calculated from mass concentration of the particle. The liquid-crystal coexistence regime extend from c/c*=0.51 up to ~0.69. As we

increase the volume fraction the percentage of crystal increases and the solution becomes fully crystal crystal at c/c*=0.7. Comparing with the hard spheres, we have a broad coexistence and glass regime due to the softness of the particles. We expect similar phase diagram for P2_402k in both solvents at different volume fraction range due to softness.

Since these systems have very high grafting density, two regions can be distinguished: (1) the Concentrated Polymer Brush regime (CPB), characterized by high grafting density σ resulting in stretched conformations of the grafted chains and (2) the intermediate brush regime that is characterized by a reduced grafting density and relaxed polymer conformations. Since for spherical particle brushes the effective grafting density decreases with increasing distance r from the particle surface according to $\sigma_{eff} = \sigma_o \left(\dfrac{r_o}{r} \right)^2$, where r_o denotes the particle core radius and σ_o is the surface grafting density, a transition from the concentrated to the semidilute regime is expected at a critical distance r_C. The latter was first reported by Daoud-Cotton for star polymer systems $r_C = 2 \upsilon r_o (\pi \sigma^*)^{\frac{1}{2}}$, with $\sigma^* = \sigma_o a^2$ denoting the dimensionless surface coverage (α is the monomer length) and υ the excluded-volume parameter that is about b/a (b is the Kuhn length) for athermal solvents (Daoud and J.P. 1982). In this case, when f chains are grafted on the surface of the particle core, $\sigma_o = \dfrac{f}{4 \pi r_o^2}$ and $r_C \approx bf^{1/2}$ is the size of the core and the concentrated brush regime (CPB), where the excluded-volume effect is screened out. The ratio r_C/L, where $L = \dfrac{R}{\sqrt{6}}$ with R to be the end to end distance in good solvent, defines the "softness" of the particle, which in our case varies depends on the system and the solvent. Voudouris (Voudouris, Choi et al. 2009) and co-workers found that for $r_C/L \approx 1$ the system behaves as a hard sphere. In the present work we will use the ratio r_C/R_H to define the softness since for the same we used different solvents, which change the hydrodynamic radius. Table 3.1 show characteristic values for different systems like hydrodynamic radius, surface density, grafting density, particle softness and effective density of the outer blobs for different soft systems. The samples a-c are the particles studied in this work.
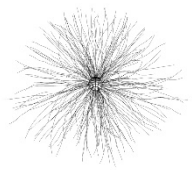
Sample name	R_h (nm)	Number of chains/nm² (σ)	Number of chains/particle (f)	r_C / L	r_C / R_H	σ_{eff} outer blob	sketch
a) P2 126K	205 (DCB-DE)	0.65	34500	0.78	0.62	0.065	
b) P2 402K	420 (Ver-DMF)	0.65	34500	0.39	0.305	0.016	
c) P2 402K	470 Tol	0.65	34500	0.39	0.27	0.012	
d) SiP-PS_short(Voudouris, Choi et al. 2009)	29	0.84	1056	1	0.90	0.098	
e) SiP-PS_long(Voudouris, Choi et al. 2009)	67	0.5	628	0.3	0.27	0.011	
f) SiP-PDMS(Petekidis, Gapinski et al. 2004)	196	8.2e-3	3114	0.34	0.17	0.0066	
g) Star 12880(Vlassopoulos, Fytas et al. 2001)	~60	-	128	~0.44	0.28	0.0028	

Table 3.1: Characteristics of silica particles grafted with PMMA shell (a-c). We use for comparison silica particles grafted with PS shell (d-e), silica particles grafted PDMS shell (f) and PB star polymer with 128 arms (g).

3.2.2 - Experimental

The technique used in this work is the so-called 3D Dynamic light scattering setup (Schatzel 1991, Overbeck, Sinn et al. 1997, Urban and Schurtenberger 1998, Urban and Schurtenberger 1998, Urban 1999) (3DDLS), in which the two incident and the two detected light paths are placed at an angle θ/2 above and below the plane of symmetry of the scattering experiment. The initial (k_1^i, k_2^i) and final (k_1^f, k_2^f) wave vector pairs are rotated by some angle about the common scattering vector q =q₁ =q₂ for the two scattering processes 1-1 and 2-2, whereas the two other scattering processes 1-2 and 2-1 detected in this experiment have different scattering vectors. These additional scattering processes will therefore contribute to the background only, which means that the maximum intercept for the 3d experiment is only one quarter of the value obtained for autocorrelation or other cross-correlation schemes such as

the two-color method, i.e. $\beta_{12,ideal}$ = 0.25 (Schatzel 1991). The reason for this reduction is that scattered light from the first (second) beam can fall also into the second (first) detector. Thus the cross-correlation function can be written as:

$$G_c = \frac{\left\langle I_1^i(0)I_2^i(\tau)\right\rangle + \left\langle I_1^i(0)I_2^{ii}(\tau)\right\rangle + \left\langle I_1^{ii}(0)I_2^i(\tau)\right\rangle + \left\langle I_1^{ii}(0)I_2^{ii}(\tau)\right\rangle}{\left\langle I^2\right\rangle} \quad (1)$$

where Arabic numbers denote the detector and Roman numbers denote the incident beam

As we said before in the 3D cross-correlation experiment the undesired contributions from the "wrong" incident beams are still detected by the photomultipliers, but they produce different scattering vectors $q_1 \neq q_2$ and are decorrelated. In the equation above only the second term gives correlated contributions to $G_c(\tau)$.

$$G_c(\tau) = \frac{3\left\langle I_1\right\rangle\left\langle I_2\right\rangle + \left\langle I_1^i(0)I_2^{ii}(\tau)\right\rangle}{\left\langle I_1^i + I_1^{ii}\right\rangle\left\langle I_2^i + I_2^{ii}\right\rangle} = \frac{3}{4} + \frac{1}{4}[1 + \beta^2[C(q,t)]] = 1 + \beta_{tot}^2[C(q,t)] \quad (2)$$

The factor β_{tot}^2 includes any correction that you have to take into account in a cross-correlation experiment and is $\beta_{tot}^2 = \beta^2\beta_{OV}^2\beta_{MS}^2\beta_T^2$, with β^2 the coherent factor, β_{OV}^2 the overlap volume factor of the two beams at the cross point, β_{MS}^2 the multiple scattering factor and β_T^2 the technique factor, which in this instrument is 0.5 [ref]. The correction factor β_{tot}^2 therefore can be calculated through the ratio values of the intercept of the correlation function between the concentrated and the dilute regime as:

$$\beta_{tot}^2 = \beta_{MS}^2\beta_{OV}^2\beta_{SETUP}^2 A = \frac{(g^{(2)}(Q,t=0)-1)_{concentrated}}{(g^{(2)}(Q,t=0)-1)_{dilute}} \quad (3)$$

The calculation of S(Q) has to take into account the scattering loss parameters like the correction factor β_{tot}^2 and the sample transmition. Then the structure factor can be written as:

$$S(Q) = \frac{I(Q)c_{dil}T_{dil}}{F(Q)c_{conc}T_{conc}}. \quad (4)$$

where subscript **dil** denotes the dilute regime and **conc** the concentrated volume fraction,**C** is the concentration and **T** the transmition.

The scattering intensity I^s(Q) is calculated by multiplying the intensity scattering intensity with the correction factor β_{tot}^2: $\quad \left\langle I^s(Q)\right\rangle = \sqrt{\beta_{tot}^2\left\langle I(Q)\right\rangle}. \quad (5)$

Several research groups (Overbeck, Sinn et al. 1997, Aberle, Hólstede et al. 1998, Urban and Schurtenberger 1998) have demonstrated the feasibility of such an experiment and clearly shown that dynamic light scattering need not be restricted to dilute suspensions of small particles, but that it can be used to successfully characterize extremely turbid suspensions down to 4 % transmition.
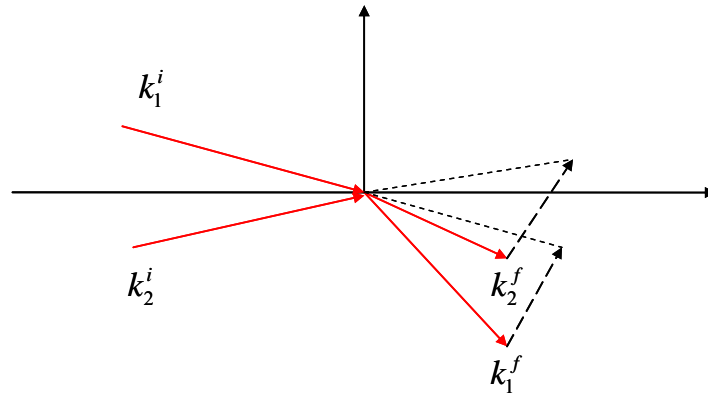

Figure 3.1: Schematic representation of 3D-DLS light path. k_{i1} is the incident wave vector of beam 1 and k_{f1} is the final , scattered light of beam 1. Beam 2 is marked analogously.

3.3 - Dilute solutions

Form factor

In the dilute regime the static scattering intensity reflects particle's form factor. In all cases the form factor is strongly q-dependent and can be fitted with core-shell models. Figure 1 show the form factor of the 3 systems studied in this work. Open symbols are experimental data and solid lines the fit for core-shell model. P2_126k shows a minimum at 0.0185 nm^{-1} (black circles) corresponding to a size of 242 nm assuming HS model (QR=4.49) and 194 nm by fitting it with the core-shell model. As we increase the softness moving to bigger particles (P2_402k) at two different solvents (Veratrole-DMF and toluene) we have the same minima at 0.012 nm^{-1} with a stronger deep of F(Q) in toluene solvent. The hard sphere models calculates an effective

3.   Structure and Dynamics in Concentrated Suspensions of Soft Colloids

size of 368 nm and the core shell model 396 and 382 in Ver-DMF (red squares) and toluene sol-

vent (blue triangles) respectively. For the core-shell model we used the fit for core-shells with

the extra term for the fuzzy outer part of the shell. The particle forma factor can be described

as:

$$F(Q) = \left[\frac{3[\sin(QR) - QR\cos(QR)]}{(QR)^3} x \exp\left(-\frac{\sigma^2 Q^2}{2} \right) \right]^2 \qquad (6)$$

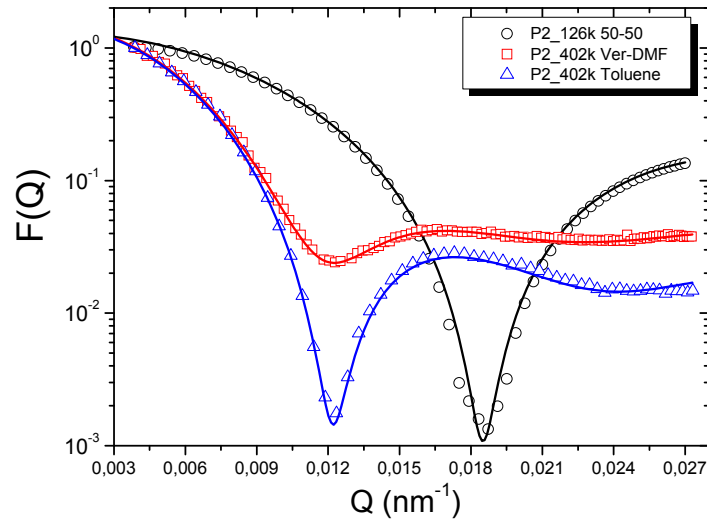where σ denotes the width of the fuzzy particle surface.

Figure 1: Particles' form factor as a function of the scattering wavevector. Open symbols are experimental data and solid lines the fit for core-shell model. P2_126k shows a minimum at 0.0185 nm^{-1} (black circles) corresponding to a size of 242nm assuming HS model (QR=4.49) and 194 nm by fitting it with the core-shell model

The softer particle (P2_402k) at two different solvents (Ver-DMF and toluene) have the

same minima with a strong deep of F(Q) in toluene solvent. The HS models give an effective size

of 368 nm and the core shell model 396 and 382 in Ver-DMF (red squares) and toluene solvents

(blue triangles).

3.4 – Concentrated solutions

3.4.1 – Static properties

Figure 3.2 shows the evolution of the normalized scattering intensity as a function of QR_H at different effective volume fractions. At higher volume fractions (c/c* ~0.48) the peak position of the intensity is at QR~2.9. This value is significant lower than the Percus-Yevick theory (Abade, Cichocki et al. 2010, Abade, Cichocki et al. 2010, Abade, Cichocki et al. 2011) which is at QR~3.5 for the concentration range close to liquid-crystal coexistence. As we decrease the volume fraction the peak position moves to lower QR (larger distances) and it's amplitude decreases and broadens due to lower probability to find particles at distance which correspond to $Q_{peak}=2*\pi/R$, where R is the particle- particle distance. At low Q's the normalized scattering intensity increases as we decrease the effective volume fraction.
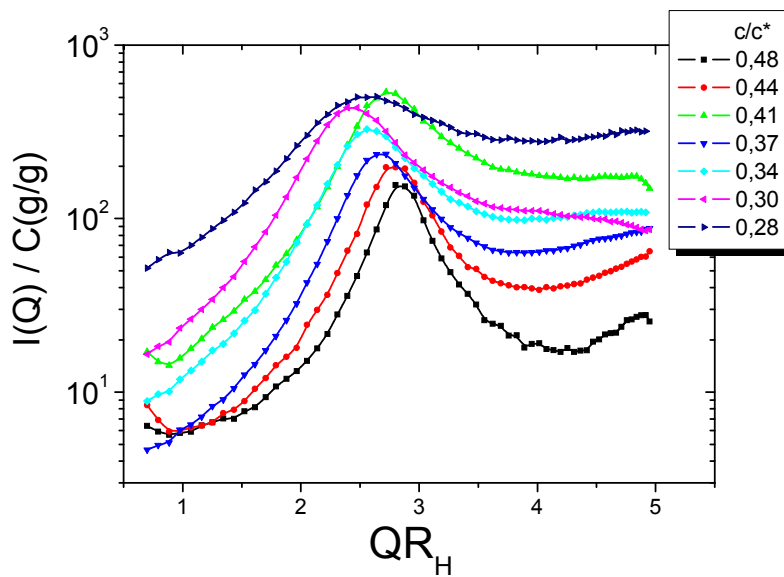

Figure 3.2: Evolution of the normalized scattering intensity as a function of the effective volume fraction(c/c*) for P2_126 in solvent mixture.

As we increase softness moving to the bigger particle (P2_402k) in solvent mixture (Ver-DMF) the particle size increases almost double and we are able to go to high QR_H range where the intensity is almost constant at all volume fractions (figure 3.3). The first minima at QR~5 which is probably due to destructive interference from the form factor (minimum of F(Q)~5.04) is also φ independent. The intensity at maximum is at QR~2.8 and moves to lower Q's as we decrease the volume fraction. At the same time the peak moves out of the experimental window, since the interparticle distance increases with decreasing volume fraction.

Figure 3.3: Evolution of the normalized scattering intensity as a function of the effective volume fraction (c/c*) for P2_402 in Ver-DMF.

Similar behavior we observe in P2_402k in toluene solvent (figure 3.4). The normalized scattering intensity at high Q's is volume fraction independent. The absolute value is almost the same with P2_402k in solvent mixture. The shape of the intensity curve is the same with the first minimum of the scattering intensity to be at QR~6 due to higher particle size compared to the solvent mixture. The position of the peak is at QR~3.5, and the interparticle distance to be closer from the solvent mixture. The peak position has the same trend and moves to lower Q's with decreasing the volume fraction
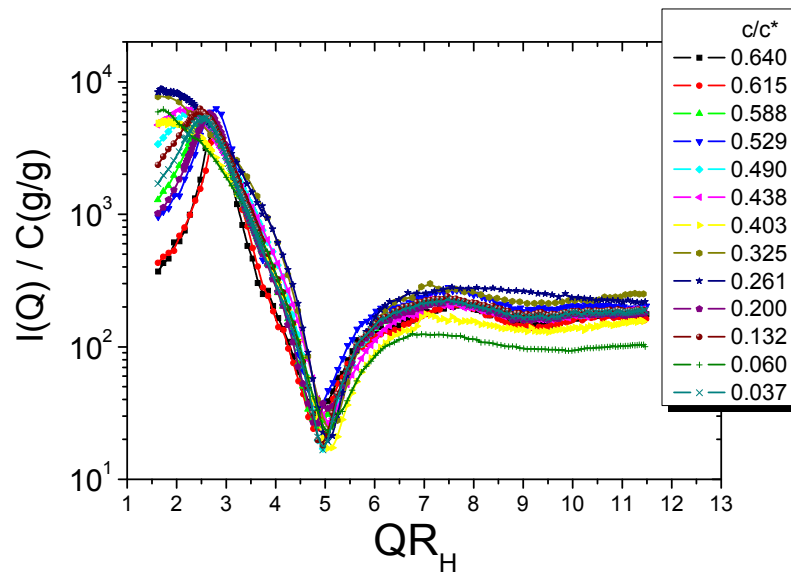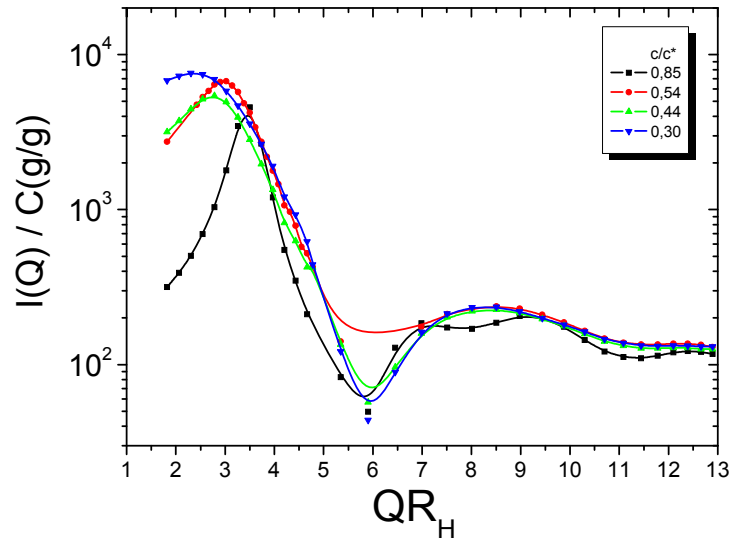
Figure 3.4: Evolution of the normalized scattering intensity as a function of the effective volume fraction for P2_402 in Toluene.

Interactions between particles were examined through structure factor. For the sake of clarity we show only the structure factor for P2_402k in Ver-DMF (figure 3.5) as was calculated by using eq. 4. The particle form factor kept constant in all the volume fraction range. At high Q's the structure factor becomes one, evidence that the thermodynamic interactions are negligible. For the analysis of the dynamics later in this work we will extract the short-time self-diffusion at high Q's where S(Q)→1, or at the specific Q where S(Q)=1. Interestingly at high q-limit we observe well defined oscillations evidence of well-ordered structure even at low volume fractions. The first minimum of S(Q) is at QR~5 and can be attributed to scattering losses due to form factor. Similar S(Q) shape was reported by Laurati et al. (Laurati, Stellbrink et al. 2007) in star like micelles at high volume fractions. In this paper the minimum is due to partial crystallization of the sample, as they have observed from SANS experiments. In our case this is unlike to be, since this minimum exists even at low volume fractions. The amplitude of the peak of S(Q) which corresponds to the concentration of the particle at a given interparticle distance shows a non-monotonic behavior with the volume fraction. At the highest volume fraction, close to liquid-crystal coexistence, the peak is at QR~2.8, significantly at higher distance comparing
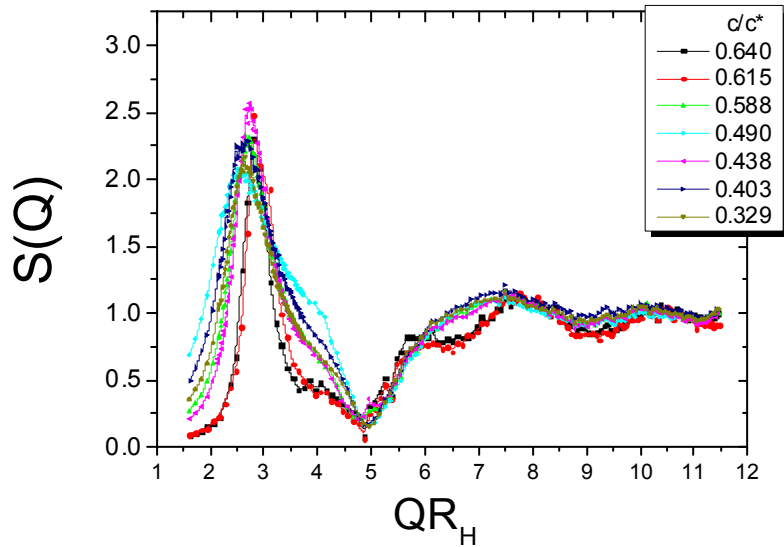
Figure 3.5: Volume fraction dependence of the normalized structure factor S(Q) for P2_402k in Ver-DMF.

with the hard spheres (QR~3.5 for φ<0.49) Moreover the width becomes broader as we decrease the volume fraction. At the limit of Q→0 the osmotic pressure (~1/S(Q=0)) strongly increases as we increase volume fraction.

By mapping the Q-position of the S(Q) we can compare and identify the particle-particle interactions. Figure 3.6 shows the Q-position for our 3 systems in comparison with hard and charged spheres. For P2_126k the dependence of the peak position up to c/c*~0.2 is similar to charged systems where the surrounding particles have interparticle distance which scales with R^{-3}. Below c/c* ~0.2 the particle-particle distance is constant. The discrepancy from hard spheres is maximum 12% at lower volume fractions. The trend is the same with hard spheres and therefore we can hypothesize that dangling chains in the outer blob lead to larger hydrodynamic size compared with the static radius taken from P(Q) may be the reason between such discrepancy. In contrast P2_402k in solvent mixture shows strong repulsive interactions which are probably particle-solvent and/or particle-particle interactions.

The same particles (P2_402k) in toluene show different behavior (figure 3.4). The particles are softer due to swelling of the PMMA chains by 12% leading to higher effective volume fractions up to 0.84. The particles within the error follow hard sphere behavior. We have to mention here that these systems do not have electrostatic interactions. Only Van der Waals interactions are possible due to RI match between shell-solvent, which however are quite short in range.
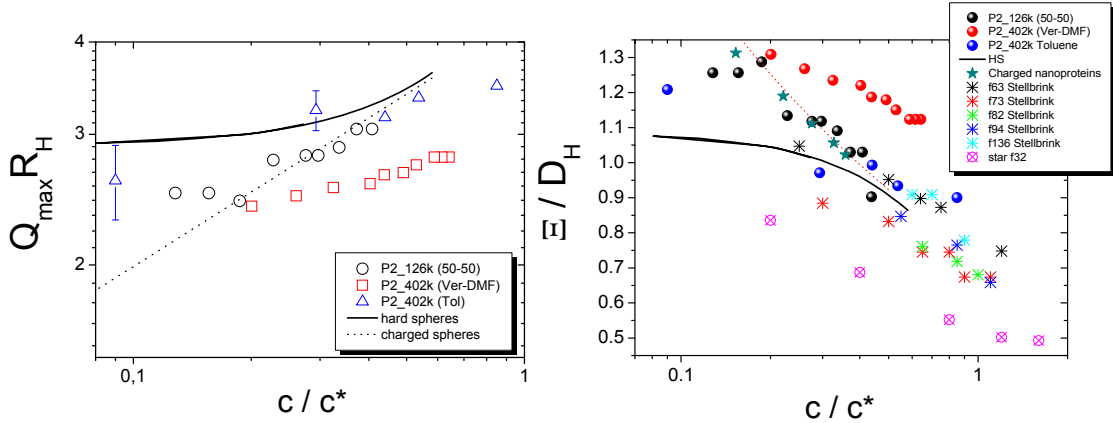
Figure 3.6: Mapping the Q-position of the peak of S(Q) as a function of the effective volume fraction for our systems, comparison with hard (solid line) and charged spheres (dashed line). **b:** normalized particle-particle distance a function of the effective volume fraction ($\Xi=2\pi/Q_{peak.}$). For direct comparison we have plotted Ξ for similar systems.

For star-like micelles (Laurati, Stellbrink et al. 2007) the Q-position changes as a function of the grafting density but in all cases we have strong interpenetration or retraction. In order to obtain the effect of the softness fig 3b shows the normalized particle-particle distance as a function of the effective volume fraction for the same systems. For values $\Xi/D_H <1$ we have interpenetration or retraction. For star-like micelles at all grafting densities the particles are soft and we have interpenetration or retraction. For charged nanoproteins Ξ/D_H values goes towards 1 at high volume fractions, a behavior also reflected in P2_126k. In P2_402k in mixture solvent Ξ/D_H decreases as we increase volume fraction and become constant at high ϕ's and equal to 1.13.

Apart from mapping the Q-position of S(Q) the amplitude of the first peak (figure 3.7) depicts the probability of 2 particles to be at distance $2\pi/Q_{peak}$, where Q_{peak} is the value at the peak of S(Q). Hard spheres predicts that S(Q) peak increases as we increase ϕ, with the maximum value to be at 2.85 for the liquid state as it is reported by Hansen and Verlet (Hansen and Verlet 1969). For P2_126k the data superimpose the hard sphere theory with a small discrepancy at low c/c*.

For P2_402k in solvent mixture the amplitude of the first peak increases reaching a plateau around c/c*~0.4, then increases up to 2.85 at c/c*~0.6 and then decreases as we continue

increasing volume fraction up to 0.64. This decrease comes from partial crystallization of the sample which decreases the peak of S(Q)].
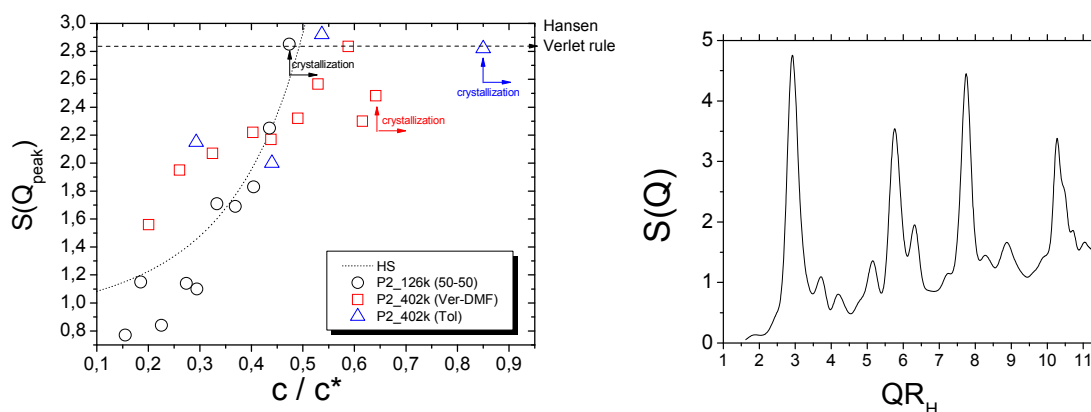

Figure 3.7a: Amplitude of the first peak of S(Q) as a function of the effective volume fraction. Dotted line denotes the HS prediction. The horizontal dashed line corresponds to the limit of the peak of S(Q) before system leads to crystallization, prediction that reported by Hansen et al. [ref] for hard spheres. **b)** structure factor of P2_402k in Ver-DMF at c/c*=0.8.

The paricles are monodisperse and partial crystallization may oocur at high volume fractions close to liquid-crystal coexistence. The non-monotonic behavior of the amplitude can be attributed to particle retraction as we increase the volume fraction. Same behaviour appears to P2_402k in toluene. Arrows denote the last volume fraction before the coexistence. Figure 3.7b shows the structure factor inside the crystal regime for P2_402k in solvent mixture. The absolute values of S(Q) may vary ~10% due to strong scattering intensity. The first peak of S(Q) is narrow and the amplitude around 5, indicating strong crystal. For the relative distances between the peaks we can estimate the type of crystal we form. The ratio of the peak position scales with $\sqrt{N}$ where N=1,2,3....,denoting FCC crystal.

The value of the structure factor at low Q's is connected to the osmotic compressibility and denotes the interaction potential between the particles. Figure 3.8 depicts the value at the loq-Q limit of the S(Q) as a function of c/c*. Interestingly the particles with the smaller chains (P2_126k) follow within errors the theory for hard spheres predicted by Segre et al. (Segre, Behrend et al. 1995) (dashed line). For the bigger particles in different solvents, the osmotic

96

compressibility is the same, meaning that there is no solvent dependence of $\dfrac{\partial \Pi}{\partial c}$. We are not able to fit the data for the bigger particle with the HS theory due to the higher effective volume fraction, even though the trend is the same. A possible reason is a shift factor in the effective volume fraction.
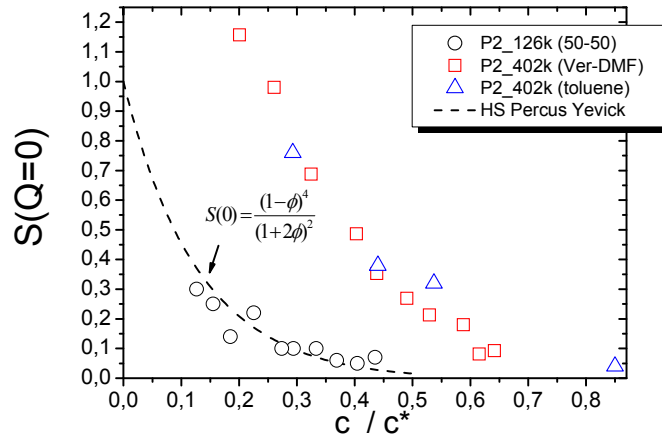
Figure 3.8: Evolution of S(Q) at Q→0 as a function of the effective volume fraction. Dashed line depicts the HS model

3.4.2 – Dynamic properties

As we have discussed before the dynamics are not affected by changes in F(Q) or in the scattering conditions. Therefore, they directly reflect the relaxation of concentrated fluctuations through the cooperative or self-diffusion mechanisms. In figure 3.9 we show the correlation function at different volume fractions for a specific scattering vector Q=0.027 nm^{-1} (θ=135°) which correspond to the highest Q-limit in our setup.
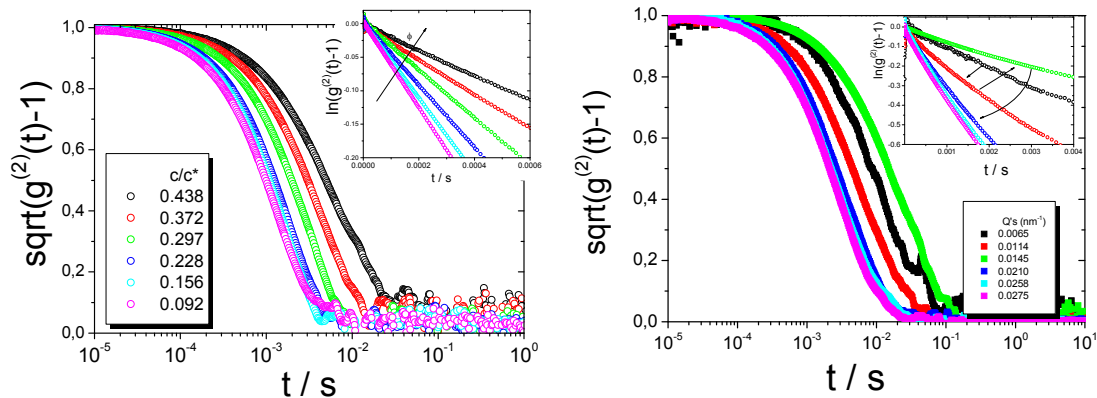
Figure 3.9a: correlation function as a function of time at different effective volume fractions **inset:** Initial slope for the relaxation function at different volume fractions at q*R_H where S(Q)~1. **b)** Correlation functions of the scattering field at different scattering wave vectors for c/c* = 0.438. **Inset:** Correlation functions in ln-lin plot.

We examine that the relaxation time becomes slower as we increase the volume fraction.

Then comparing the correlation function at different scattering vectors we observe an non-monotonic behavior with the scattering vector at c/c* = 0.435. This comes from the rise of S(Q) which is inverse proportional of D(Q) as: $D(Q) = D_0 \dfrac{H(Q)}{S(Q)}$.

Figure 3.10 reveals the effect of hydrodynamic and thermodynamic interactions in D(Q) for all the systems. At higher Q's the normalized D(Q) reflects the Q-independent $D_s(Q)$. The dynamics at the peak of S(Q) slow down with φ. Figure 8a shows the normalized D(Q) for P2_126k. In comparison we plot the HS calculation at the same volume fraction (lines). As we decrease the volume fraction we have discrepancy from the HS curves. Even at low volume fractions (c/c*=0.2) the dynamics around the peak which corresponds to particle particle interactions are stronger compared to hard spheres (Segre and Pusey 1996) . In all cases the deep position is at lower Q's comparing with the hard spheres.
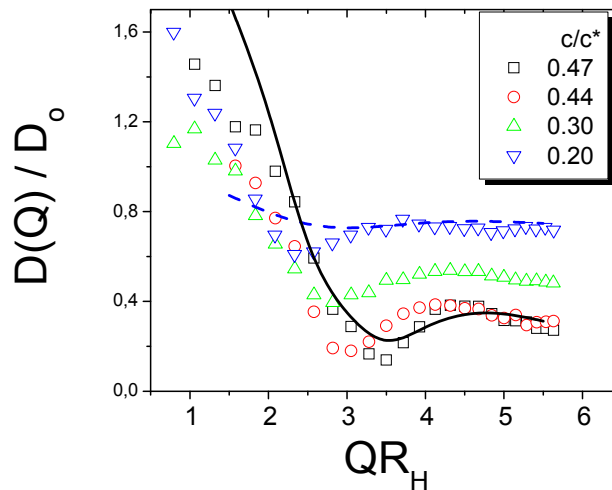
Figure 3.10a : Normalized diffusion coefficient as a function of Q*R_H for P2_126k at different effective volume fractions (open symbols). Solid lines depict the HS calculation of D(Q) at the same volume fraction.

For the softer particle (P2_402k in mixture) a strong Q-dependence of the normalized D(Q) is observed (figure 3.11). The minimum of D(Q) is at lower QR's (QR~2.80) denoting longer

in range interactions in respect to P2_126k. Since the particles are big we can extract accurately the short time self-diffusion $D_s^s(Q)$ in the Q-range where $D_s^s(Q)$ is Q-independent and S(Q)~1. In this system we observe an extra strong minimum of D(Q) at $Q_{max}R_H$ ~ 5-6 which is probably due to the minimum of the form factor.

Figure 3.11: Normalized diffusion coefficient as a function of Q*R_H for P2_402k in Veratrole – DMF mixture at different effective volume fractions
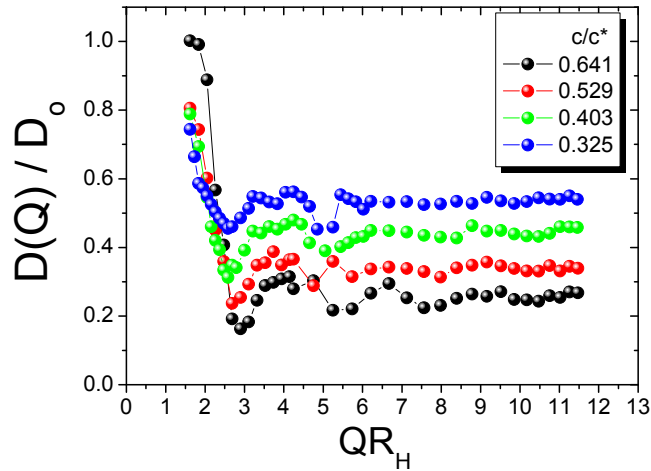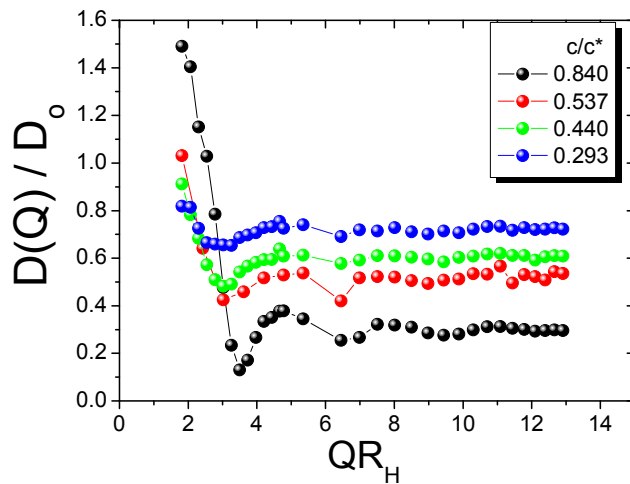

Figure 3.12: Normalized diffusion coefficient as a function of Q*R_H for P2_402k in toluene at different effective volume fractions.

Using the same particles and changing the solvent to toluene (figure 3.12), the particles swell around 12% and becomes softer. The position of the deep of D(Q) is at QR~3.5, moving to

lower QR's with decreasing c/c* similar to hard spheres. At QR$_H$ > 10 we extract the $D_s^s(Q)$ in the same way as previously.

Figure 3.13 shows the normalized $D_s^s(Q)$ as a function of the volume fraction for the 3 systems. The data will be compared with hard and permeable sphere theory (Abade, Cichocki et al. 2010, Abade, Cichocki et al. 2010, Abade, Cichocki et al. 2011). It is clear from figure 8 that there is a discrepancy with hard sphere theory for the normalized D(Q). This discrepancy comes from softness of the particle of the outer part (probably dangling effect) due to low surface density of the outer blob. Comparing this deviation with the theory of permeable spheres by Nagele et al., the particles can interpreted as porous spheres with different reduced inverse hydrodynamic screening length x, with $x = \kappa * R_H$, with k the permeability factor (Abade, Cichocki et al. 2011). The calculation of the inverse hydrodynamic screening length were made by fitting the equation for the normalized diffusion coefficient D(Q) for annulus spheres to our experimental data. The equation proposed by Nagele using HYDROPOLE method (Abade, Cichocki et al. 2011) for the normalized translational diffusion is:

$$\frac{D(Q)}{D_0(Q)} = 1 + \lambda_t(x) * \varphi_{eff}(1 + 0.12 * \varphi_{eff} + O(\varphi_{eff}^2)), \text{ with } \varphi_{eff} = c/c*$$

For P2_126k the normalized D(Q) can be fitted with x=30 and k=0.146. By increasing softness (P2_402k in mixture) the dynamic properties change significant. At intermediate volume fraction the normalized $D_s^s(Q)$ slows down faster even from the HS theory. The origin of this is unclear and may denote an extra repulsive force due to solvent effect, as such effect is absent in toluene. By continuing increasing the volume fraction we see a departure from the HS theory with the normalized $D_s^s(Q)$ exhibits a weaker decrease at higher Q's (figure 3.12). At these high φ's the compressibility is high and the particle have 4 times lower surface density on the outer blob (table 1) comparing with P2_126k. This softness can be fitted with permeable spheres with x=11 and k=0.026 nm^{-1}. As we increase the softness by changing the solvent (P2_402k in toluene) the $D_s^s(Q)$ slows down at higher φ's showing the softer character of the particle and data superimpose with permeable spheres with x=7 and k=0.015 nm^{-1}.

An interesting point worth checking is the inverse permeability k^{-1} which depicts how much is the softness in actual scale. As we calculated for P2_126k k=0.146 → k^{-1}=7 nm. For

P2_402k we found the k^{-1} = 38 and 67 for Ver-DMF and Toluene respectively. If we compare these values with the hydrodynamic sizes, we found that the softness is up to a certain size for both systems even if we changed solvent (R_H =420 and 470 for Ver-DMF). This cut-off around 380-400 nm approximately, evidence that the particles are soft only close to the edge if we take into account that the core size is 65 nm.
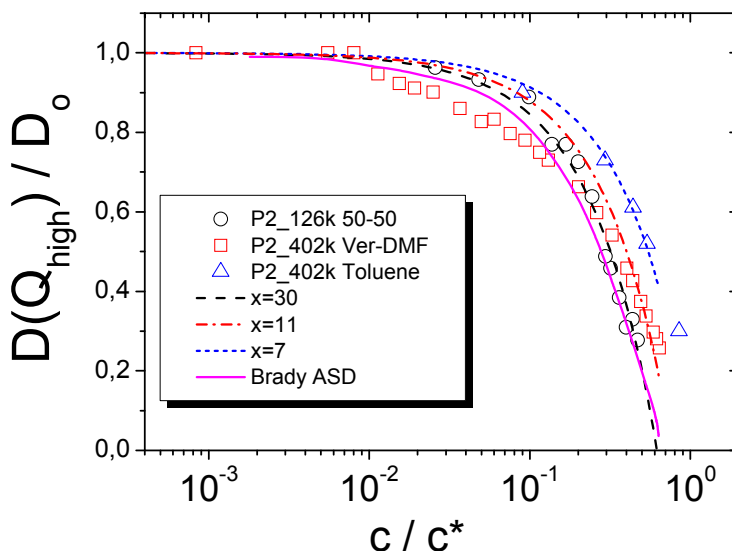
Figure 3.13: Normalized short-time self-diffusion coefficient as a function of the effective volume fraction. Solid lines depict the theories for hard spheres (magenta) and permeable at different permeabilities. The hard sphere prediction is from ASD simulations by Brady et. al. (Banchio and Brady 2003). Simulations for the permeable spheres were performed by Nagele et al. using HYDROPOLE model (Abade, Cichocki et al. 2010).

The softness effect is also depicted in the normalized cage diffusion coefficient $D(Q_{min})$ (figure 3.14). The theory for permeable spheres is also valid for the smaller particle and for the large one in toluene solvent. There is a small discrepancy in terms of the actual values of the permeability which maybe is due to the calculations that we have done in order to extract the theoretical values of the cage diffusion coefficient. Something interesting is the change of the slope of the cage diffusion around c/c*~0.45 which seems to be valid in both systems where we have points in liquid state above the c/c*~0.5 the hard-sphere liquid-crystal coexistence. We observed similar behaviour in the amplitude of S(Q) and we referred it to particle retraction.
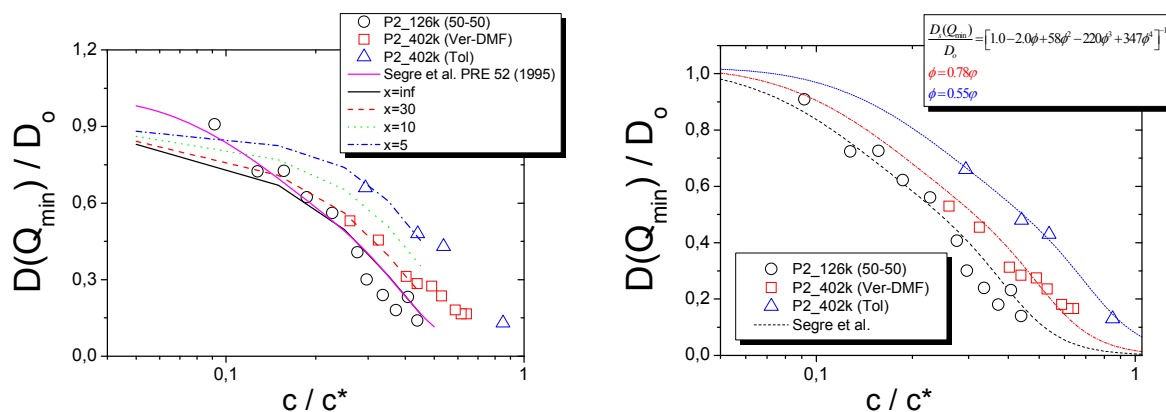
Figure 3.14: Normalized diffusion coefficient at the minimum of D(Q) as a function of effective volume fraction. Solid lines depict the theories for hard spheres (magenta) and permeable at different

By fitting the hard sphere model for cage diffusion using an effective volume fraction (figure 3.14 right), we clearly observe that the data are in good agreement with the scaled volume fraction. Black solid line in figure 3.14 (right) is plotted until one, unlike with the theory that predicts the cage diffusion is zero at random close packing fraction (ϕ=0.64) , in order to show the nice fitting in the soft particles.

From the minima of D(Q) we can calculate an apparent random close packing fraction. In hard sphere theory the structural dynamics become zero at random close packing, as it is proposed by Segre et al. (Segre, Behrend et al. 1995). To calculate the effective Random Close Packing fraction (RCP) we plot the cage diffusion coefficient as a function of the reduced volume per particle V/V_0 ($V/V_0 = \pi/6\phi$) (figure 3.15). The data can be described by a linear function at high volume fractions. The extrapolated volume fraction ϕ^* of zero diffusion coefficient $D_S(Q_{min})=0$ found to be close to 0.64 for P2_126k ($\Phi_{RCP} = 0.67 \pm 0.04$) and much higher for P2_402k in ver-DMF ($\Phi_{RCP} = 0.92 \pm 0.02$) and P2_402k in toluene ($\Phi_{RCP} = 1.14 \pm 0.05$).
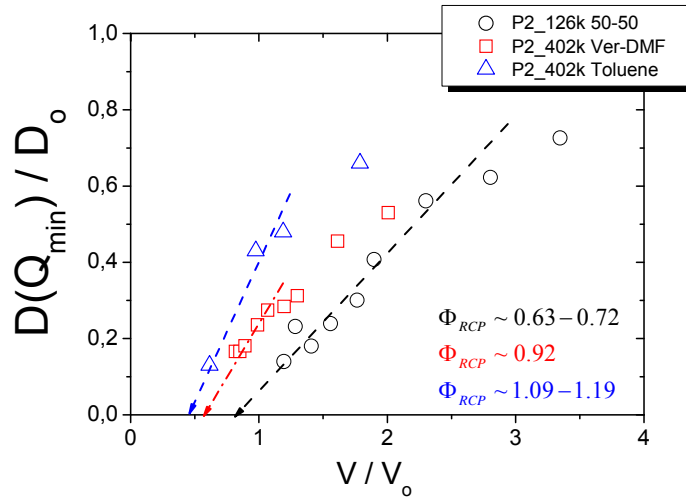
Figure 3.15: Normalized diffusion coefficient at the main peak of S(Q) as a function of the reduced volume per particle $V/V_o = \pi/6\phi$ as proposed by Segre et al. [ref]. The arrows denote the RCP for each system. As we increase the softness, the volume fraction at the maximum packing increases from around 0.65 (P2_126k) to 1.1 for P2_402k in toluene.

The dynamics in the low-Q limit reflect the collective diffusion and cooperative motion can be extracted. For the bigger particles in the two solvents, the cooperative diffusion cannot be calculated safely dute to the high QR values (QR>>1). For the smaller particle we used the points of the lowest Q. In figure 3.16 we plotted the cooperative diffusion as a function of c/c* for P2_126k. At the same graph we have plotted also the shot-time self-diffusion for the same system, together with the HS theory and the theory for permeables. The data are in good agreement with the hard sphere theory.
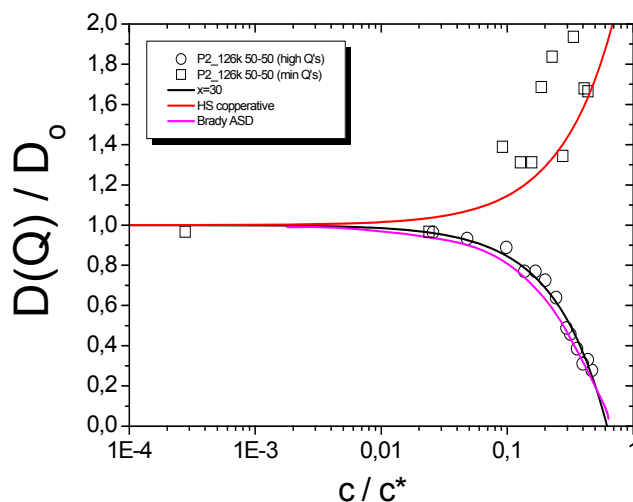
Figure 12: Normalized diffusion coefficient as a function of the effective volume fraction for P2_126k. Open squares show the cooperative diffusion, extracted at the limit of Q→0 and are in agreement with the HS model (red line)

103

3.5 - Conclusions

Structure and dynamics in concentrated suspensions were investigated through 3D dynamic light scattering experiments. We observed rich phase diagram but wider compared to HS. The structure properties show deviations from hard spheres, denoting the soft particle character. Specifically for P2_402k we observed a non-monotonic behavior in the amplitude of S(Q) , evidence of particle retraction. The particles have long-range repulsive interactions with Ξ/D_H to be 1.13 for the concentrations close to liquid-crystal coexistence.

For the dynamical properties, theory for permeable spheres seems to be the best candidate to describe the behavior. By changing one parameter, the hydrodynamic penetration depth x, we were able to fit self-diffusion and cage (structural) diffusion. The packing fraction extracted from the limit of $D(Q_{min}) \to 0$ increases as we increase particle size (softness). For P2_126k the apparent random packing is close to HS (c/c*(RCP)~0.67) and becomes 1.2 for P2_402k in toluene.

3.6 - References

Abade, G. C., B. Cichocki, M. L. Ekiel-Jezewska, G. Nagele and E. Wajnryb (2010). "Dynamics of permeable particles in concentrated suspensions." Physical Review E **81**(2): 4.

Abade, G. C., B. Cichocki, M. L. Ekiel-Jezewska, G. Nagele and E. Wajnryb (2010). "Short-time dynamics of permeable particles in concentrated suspensions." The Journal of Chemical Physics **132**(1): 014503-014517.

Abade, G. C., B. Cichocki, M. L. Ekiel-Jezewska, G. Nagele and E. Wajnryb (2011). "Rotational and translational self-diffusion in concentrated suspensions of permeable particles." The Journal of Chemical Physics **134**(24): 244903-244907.

Aberle, L. B., P. Hólstede, S. Wiegand, W. Schrφer and W. Staude (1998). "Effective Suppression of Multiply Scattered Light in Static and Dynamic Light Scattering." Appl. Opt. **37**(27): 6511-6524.

Banchio, A. J. and J. F. Brady (2003). "Accelerated Stokesian dynamics: Brownian motion." The Journal of Chemical Physics **118**(22): 10323-10332.

Banchio, A. J. and G. Nagele (2008). "Short-time transport properties in dense suspensions: From neutral to charge-stabilized colloidal spheres." Journal of Chemical Physics **128**(10).

Chrissopoulou, K., V. A. Pryamitsyn, S. H. Anastasiadis, G. Fytas, A. N. Semenov, M. Xenidou and N. Hadjichristidis (2001). "Dynamics of the Most Probable Composition Fluctuations of "Real" Diblock Copolymers near the Ordering Transition." Macromolecules **34**(7): 2156-2171.

Daoud, M. and C. J.P. (1982). "Star shaped polymers: a model for the conformation and it's concentration dependence." J. Physique: 531-538.

Eckert, T. and W. Richtering (2008). "Thermodynamic and hydrodynamic interaction in concentrated microgel suspensions: Hard or soft sphere behavior?" Journal of Chemical Physics **129**(12).

Gapinski, J., A. Patkowski, A. J. Banchio, J. Buitenhuis, P. Holmqvist, M. P. Lettinga, G. Meier and G. Nagele (2009). "Structure and short-time dynamics in suspensions of charged silica spheres in the entire fluid regime." Journal of Chemical Physics **130**(8).

Hansen, J.-P. and L. Verlet (1969). "Phase Transitions of the Lennard-Jones System." Physical Review **184**(1): 151-161.

Laurati, M., J. Stellbrink, R. Lund, L. Willner, E. Zaccarelli and D. Richter (2007). "Asymmetric poly(ethylene-alt-propylene)-poly(ethylene oxide) micelles: A system with starlike morphology and interactions." Physical Review E **76**(4).

Loppinet, B., G. Fytas, D. Vlassopoulos, C. N. Likos, G. Meier and G. J. Liu (2005). "Dynamics of dense suspensions of star-like micelles with responsive fixed cores." Macromolecular Chemistry and Physics **206**(1): 163-172.

Megen, W. v. and S. M. Underwood (1993). "Dynamic Light Scattering Study of Glasses of Colloidal Hard Spheres." Physical Review E **47**: 248.

Ohno, K., T. Morinaga, K. Koh, Y. Tsujii and T. Fukuda (2005). Synthesis of Monodisperse Silica Particles Coated with Well-Defined, High-Density Polymer Brushes by Surface-Initiated Atom Transfer Radical Polymerization. **38:** 2137-2142.

Overbeck, E., C. Sinn and T. Palberg (1997). Approaching the limits of multiple scattering decorrelation: 3D light-scattering apparatus utilising semiconductor lasers. Optical Methods and Physics of Colloidal Dispersions**:** 117-120.

Pamvouxoglou, A. (2006). Viscoelastic response of micelles with chemically cross-linked cores, Materials Science & Technology.

Petekidis, G., J. Gapinski, P. Seymour, J. S. van Duijneveldt, D. Vlassopoulos and G. Fytas (2004). "Dynamics of core-shell particles in concentrated suspensions." Physical Review E **69**(4).

Pusey, P. N. and R. J. A. Tough (1985). Particle interactions," in Dynamic Light Scattering, R. Pecora, ed. New York, Plenum.

Schatzel, K. (1991). "Suppression of Multiple Scattering by Photon Cross-correlation Techniques." Journal of Modern Optics **38**(9): 1849 - 1865.

Segre, P. N., O. P. Behrend and P. N. Pusey (1995). "Short-time Brownian motion in colloidal suspensions: Experiment and simulation." Physical Review E **52**(5): 5070-5083.

Segre, P. N. and P. N. Pusey (1996). "Scaling of the Dynamic Scattering Function of Concentrated Colloidal Suspensions." Physical Review Letters **77**(4): 771.

Sigel, R., S. Pispas, D. Vlassopoulos, N. Hadjichristidis and G. Fytas (1999). "Structural Relaxation of Dense Suspensions of Soft Giant Micelles." Physical Review Letters **83**(22): 4666.

Stellbrink, J., J. Allgaier and D. Richter (1997). "Dynamics of star polymers: Evidence for a structural glass transition." Physical Review E **56**(4): R3772.

Urban, C. (1999). Development of Fiber Optic Based Dynamic Light Scattering for a Characterization of Turbid Suspensions, ETH.

Urban, C. and P. Schurtenberger (1998). "Characterization of Turbid Colloidal Suspensions Using Light Scattering Techniques Combined with Cross-Correlation Methods." Journal of Colloid and Interface Science **207**(1): 150-158.

Urban, C. and P. Schurtenberger (1998). Dynamic light scattering in turbid suspensions: An application of different cross-correlation experiments. Trends in Colloid and Interface Science XII**:** 61-65.

Vlassopoulos, D., G. Fytas, T. Pakula and J. Roovers (2001). "Multiarm star polymers dynamics." J. Phys. : Condens. Matter **13**: R855-R876.

Voudouris, P., J. Choi, H. Dong, M. R. Bockstaller, K. Matyjaszewski and G. Fytas (2009). "Effect of Shell Architecture on the Static and Dynamic Properties of Polymer-Coated Particles in Solution." Macromolecules **42**(7): 2721-2728.

Chapter 4   Slow dynamics, ageing and Glass-Crystal Re-entrant in soft colloids

4.1 - Introduction

The glass transition in colloidal systems has attracted considerable scientific interest for many years (Pusey 2008). Significantly high number of publications have focused on understanding the dynamics approaching and above the glass transition. In a variety of systems, the structural relaxation slows down upon reducing temperature or increasing concentration, approaching the liquid-crystal transition. In the glass regime it is often evidenced that dynamics slow down with waiting time (Cipelletti and Ramos 2005, Masri, Brambilla et al. 2009). Recently molecular dynamic simulations in hard spheres found spontaneous crystallization in glass regime where the system ages with time (Zaccarelli, Valeriani et al. 2009).

Studies of star polymers by Monte Carlo simulations and theory (Watzlawek, Likos et al. 1999, Foffi, Sciortino et al. 2003) report a variety of crystal phases, with no clear experimental evidence. The lack of experimental proof was attributed to fluctuations of the outer blob and polydispersity effects. The first report came from Stiakakis et al. (Stiakakis, Wilk et al. 2010) with multiarm star polymers, where a glass-crystal transition was revealed through Multispeckle Dynamic Light Scattering (MSDLS) and SANS experiments. Here we investigate similar effects in core-shell particles in an effort to understand th extend of universal behavior of such soft particle glasses.

107

4.2 – Method

4.2.1 – Materials

The core-shell particles used for this work are the same with the particles used for the 3DDLS experiments (chapters 3) and P2_41k that has been studied elsewere. We preferred to use the solvent mixture of Veratrole-DMF for P2_41k and P2_402k to refractive index match with the corona and suppress the multiple scattering. The sample was placed in a NMR cell to minimize multiple scattering. The rejuvenation was performed by vortexing the sample with a stainless steel ball immersed in the solution and then stiring using a magnet in order to erase the history of the sample.

Sample name	R_h (nm)	Number of chains/ nm^2 (σ)	Number of chains/particle (f)	r_C / R_H	σ$_{eff}$ outer blob	sketch
P2 41K	130 (Ver-DMF)	0.55	34500	1.00	0.138	
P2 402K	420 (Ver-DMF)	0.65	34500	0.305	0.016	

Table 1: Sample names and characteristics of the particles used for rheology

In order to fully characterize the systems studied, visual observations were performed to define the phase diagram, similarly with the protocol used in chapter 3. For the smaller and harder particle (P2_41k) the visual observation test together with rheology showed only liquid-glass transition, even though crystal phase was expected due to very small polydispersity. For the larger and softer particle (P2_402k) the liquid-crystal coexistence was between c/c*~0.65 and c/c*~0.75-0.77, beyond which the system was trapped in the glassy state.

4.2.2 - Experimental

The experimental setup we used is shown in figure 4.1. In this setup we have two different detection units for the scattered light. Arm 1 holds the MSDLS setup while arm 2 a conventional DLS setup. The sample is placed at the center of the vat in a way that the laser beam passes through the center of the cell. The cell is immersed in an index matching liquid (decalin) to avoid reflections. The temperature controlling unit is built at the bottom part of the vat (will be discussed further in the text).

A green CW Nd-Yag laser (Coherent) beam with a wavelength of λ=532 nm was used in this setup. The beam is vertically polarized and passes through a beam coupler – fiber (single mode – polarization maintaining) – collimator system which is placed close to the goniometer. The polarization of the incident and the scattered beam is vertical to the scattering plane and can be tuned by the polarizers P1, P2 and P3. After the collimator the incident beam passes through the polarizer P1 and is scattered from the sample in the cell. The detection units for the conventional DLS and MSDLS are positioned on the two arms. On arm 2 we have the conventional DLS setup with a photon multiplier as a detector. The coherent and polarized beam[2] passes impinges on the sample and is scattered in all directions. Then the PMT collects the scattering light at an angle, θ, relative to the incident beam and a digital multi-tau (ALV-5000 E) calculates the autocorrelation function of the scattering intensity.

On arm 1 we have placed as a detection unit a CCD camera. This setup consists of a polarizer P2 a pinhole which defines the speckle size[3] (figure 4.1) (d=2.5mm) and a lens at distance 2*f from the camera to image the speckles at a magnification of M=1. The advantage of this setup is that we can directly measure a large number of speckles at the same scattering angle (bright spots on the image of figure 4.1).

The sensor of the CCD camera contains multiple pixels, each one of them works as a single photon detector (photomultiplier in arm 2). We also used software which instead of the correlator calculates the auto-correlation function.

---

[2] To achieve this we use single mode fiber with a gradient index lens (GRIN), which focuses the scattering light at the center of the fiber (O/Z collimator , LPC-01-488-3.5/126-S-0.6-2.6GR-25-3S-3A-4)
[3] With this pinhole we have a difference in the scattering angle $\Delta\theta \sim 1°$
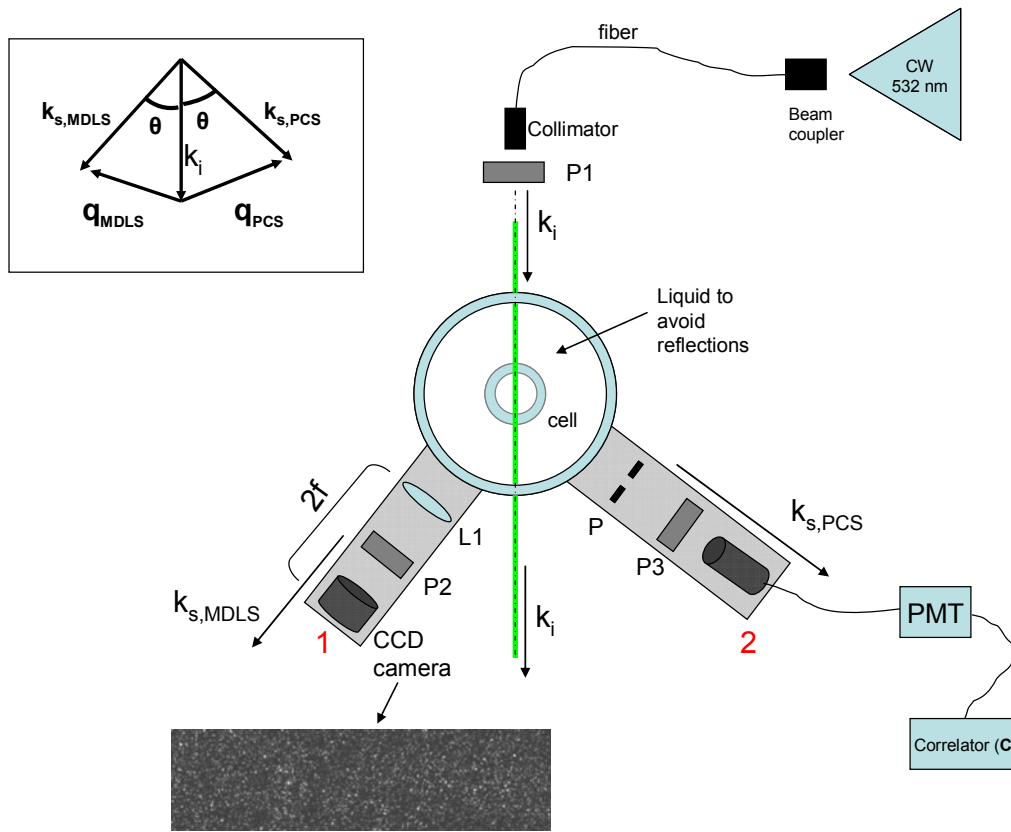
Figure 4.1: schematic representation of the home made experimental setup. In this setup we use two different arms for the two different setups; the conventional DLS (arm 2) and the modified MSDLS (arm 1). Furthermore we show an image of the speckle pattern, as it is captured from the CCD camera.

The software process a series of images from the CCD camera (similar picture is the one in figure 4.1), which are saved in the hard drive of a computer. The software will be explained in detail later. During such long time measurements we need to take into account the temperature stability. Small differences in temperature during slow dynamics and aging measurements may affect the experiment (Cipelletti and Ramos 2005). For that reason we have put together a temperature controlling system with heating and cooling which is controlled by a temperature controller. The fluctuation of the temperature inside the vat is $\Delta T \sim 0.03^oC$. Inside the copper cylinder we have placed an optical glass that we use as vat. The vat is filled with decalin to avoid reflections and to have temperature stability in the cell. In the cylinder copper we have implanted 3 ceramic thermal cylinders in order to isotropically heat the glass vat. These ceramic

cylinders are controlled by a temperature controller. Under the copper cylinder (see bottom view) we have installed a liquid cooling system[4] which is connected to a temperature controlling bath. This temperature controlling system is very stable in a temperature regime between 5°C up to 90°C providing a ± 0.05°C accuracy.

Software Correlator – Calculation of autocorrelation function

During the MSDLS experiment a series of images with different speckle pattern are saved in the hard disk drive of the computer. The time difference between the images depends on the frame rate that we are using during the experiment. These images are uncompressed bitmap files (raw files). The CCD camera that we are using is a BW 8-bit digital camera (Basler A301f) with a CCD area of 649(H) x 486(V). For most experiments we were using a region of 300(H) x 60(V) and frame rates between 2 & 82/s depending on the experiment. This means that our images are arrays of 300 columns by 60 rows, with integer values from 0 to 255. The software that we are using to capture and save images is "Streampix" (NorPix). In order to calculate the correlation of the images, a program copies the pixel intensity of each frame to the RAM or the hard disk of the computer. We can then write the intensity of each pixel p at time t as $I_p^{raw}(t)$. We also measure the dark counts of each pixel by doing the experiment with the same frame rate but without illuminating the sample. By averaging a number of frames (~100) we derive the average intensity of the dark counts for each pixel $\left\langle I_p^{dark} \right\rangle$. The instantaneous value of the scattered intensity measured by the pth pixel at time t used to calculate the autocorrelation function (Cipelletti and Ramos 2005) is, then:

$$I_p(t) = I_p^{raw}(t) - \left\langle I_p^{dark} \right\rangle \tag{1}$$

$I_p(t)$ is used to calculate the degree of correlation of the scattered intensity of two images separated by lag time τ:

$$c_I(t, \tau) = \frac{\langle I_p(t) I_p(t+\tau) \rangle_p}{\langle I_p(t) \rangle_p \langle I_p(t+\tau) \rangle_p} \tag{2}$$

---

[4] We use a liquid cooling system similar to what is used to cool hardware parts in computer systems.

where the average $\langle ..... \rangle_p$ is taken over all CCD pixels (figure 2.2.4). The degree of correlation $c_1(t, \tau)$ is calculated by multiplying two frames (the first at t and the second at t + τ), and summing up the results from all pixels by the number of the pixels $\left(\langle I_p(t) I_p(t+\tau) \rangle_p \right)$. Note that no time average is needed; the degree of correlation depends on both the lag time τ between the two images analyzed and the time t at which the first image of the pair is taken.
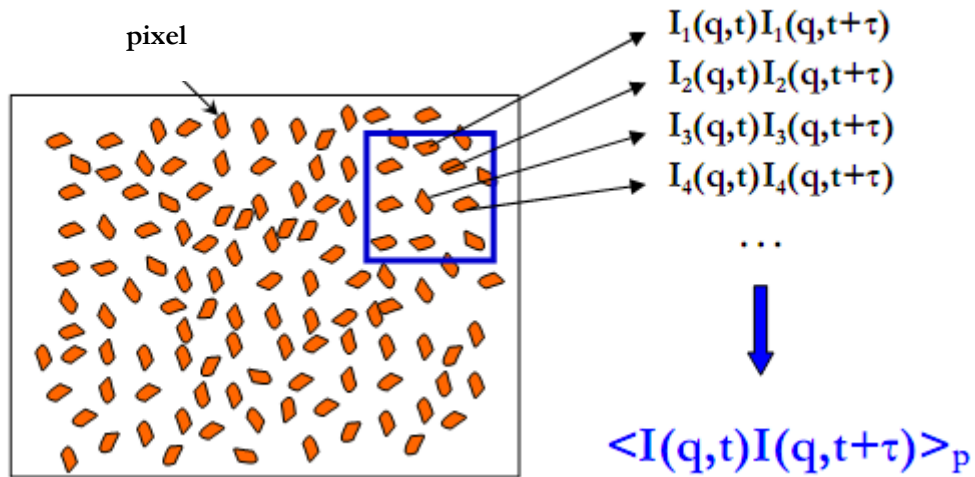
Figure 4.2: Schematic representation for calculating the autocorrelation function of the scattered intensity in a MSDLS experiment.

The use of asymmetric normalization in the degree of correlation $\left(\langle I_p(t) \rangle_p \langle I_p(t+\tau) \rangle_p \right)$ instead of $\left(\langle I_p(t) \rangle_p^2 \right)$ gives more reliable results when the intensity of the incident beam has long time fluctuations. For that reason we use a fiber to guide the laser beam to the sample (figure 4.1). The use of the fiber is very important in order to avoid the laser beam point instabilities which are very crucial in MSDLS setup. This instability comes from small fluctuations in the propagation direction of the laser beam. As long as the center of the speckle pattern is around the direction of the propagated beam and is recorded in the CCD camera, small changes in the propagation direction will change the position of the speckles in the speckle pattern arti-

ficially. Therefore the intensity of each pixel will change and leading to an artificial drop in the correlation function $c_1(t,\tau)$.

In MSDLS $c_1(t,\tau)$ provides the real ensemble average of the normalized autocorrelation function of the scattering field $\left(\left| C(q,t) \right|^2 = \dfrac{\left(\langle c_1(t,\tau) \rangle_t - 1 \right)}{f*} \right)$ where $\langle \ \ \rangle_p$ is a time average, typically of 10-100s, because each frame consists of 18000 pixels. Therefore $c_1(t,\tau)$ is a snapshot of the system dynamics and thus such method is very useful when we want to study systems with non-stationary dynamics.

4.3 – Results / Discussion

By increasing the volume fraction, moving to the glass regime the system becomes non-ergodic and ageing phenomena were observed. Both systems, the small and hard P2_41k and the bigger and softer P2_402k, show ageing phenomena with the slowest relaxation time to further increase with the waiting time. Below we discuss the Multispeckle Dynamic Light Scattering (MSDLS) data for each of these systems

The harder and smaller (P2_41k)

We will first start our discussion with the smaller particle and show how the dynamics are changing with time (ageing) and how such behavior is affected by concentration.

Figure 4.3 shows the angular dependence of P2_41k at c/c*=0.81. The system is in the glass regime but very close to liquid-glass coexistence, as has been explored experimentally from rheology (c/c* (liquid-glass) ~ 0.75-0.77). The correlation function shows two distinct relaxation processes, one in the range of 10^{-2} s and one very slow around 10-100 s. Here the angular dependence was taken at t_w= 244 s after rejuvenation. The correlation functions plotted be-

low, consist of three separate correlation functions, one taken from the fiber and two from the camera at different frame rates. The superposition was performed by simply merging all the correlation functions. A double stretched exponential fit was used to capture the two relaxations processes.
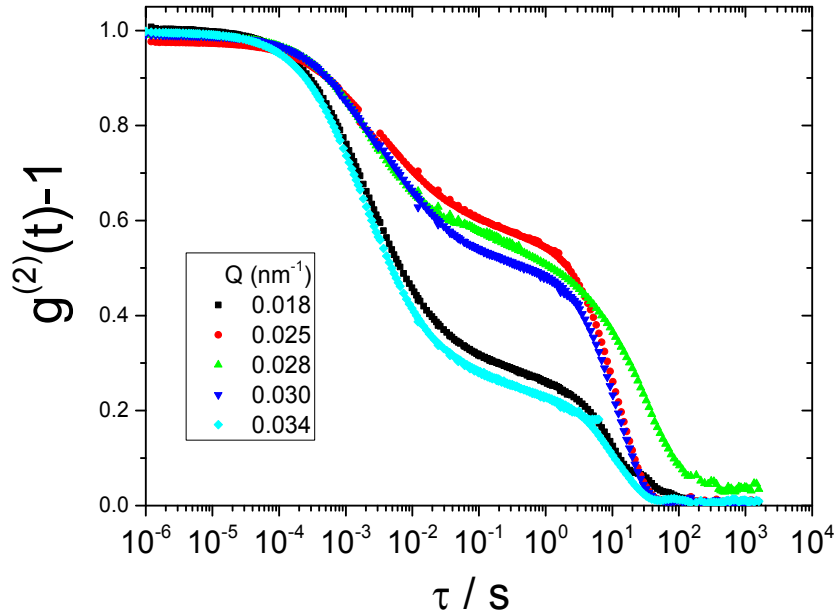

Figure 4.3: Angular dependence of the intermediate scattering function (ISF) for P2_41k at c/c*=0.81 before ageing.

By measuring the relaxation processes at different scattering angles, we extracted the diffusion coefficient $D(Q)$ for the slow and the fast process. Here we have to notice that from light scattering experiments performed in the liquid state, the $D(Q)$ is Q-dependent with $D(Q)\sim 1/S(Q)$. The peak of $S(Q)$ and therefore the minimum of $D(Q)$, is at $Q=0.025$ nm^{-1}, for the highest measured volume fraction (c/c*= 0.56). Both relaxation processes show a non-monotonic behavior with Q. Figure 4.4 show $D(Q)$ as a function of Q^2 for the fast and the slow process. The fast process, related with in cage diffusion (β relaxation) is plotted as $D_S(Q)/D_0$ in order to compared with the short-time self-diffusion in the dilute regime. As we can see in the figure below on the left, there is a strong Q-dependence, evidence that thermodynamics through the structure factor are affecting the dynamics of the system. Similar behavior we observe for the slowest process, $D_L(Q)/D_0$ (4.4 right). With closed symbols we indicate the average

relaxation time τ_{av} taking into account the stretching exponent factor β, $\tau_{av} = \left(\frac{\tau}{\beta}\right) * \Gamma\left(\frac{1}{\beta}\right)$, whereas the open symbols referred to the relaxation time, τ, only. Both measures exhibit a strong Q-dependence with the minimum taking place at slightly higher Q's compared to the short-time in-cage diffusion.
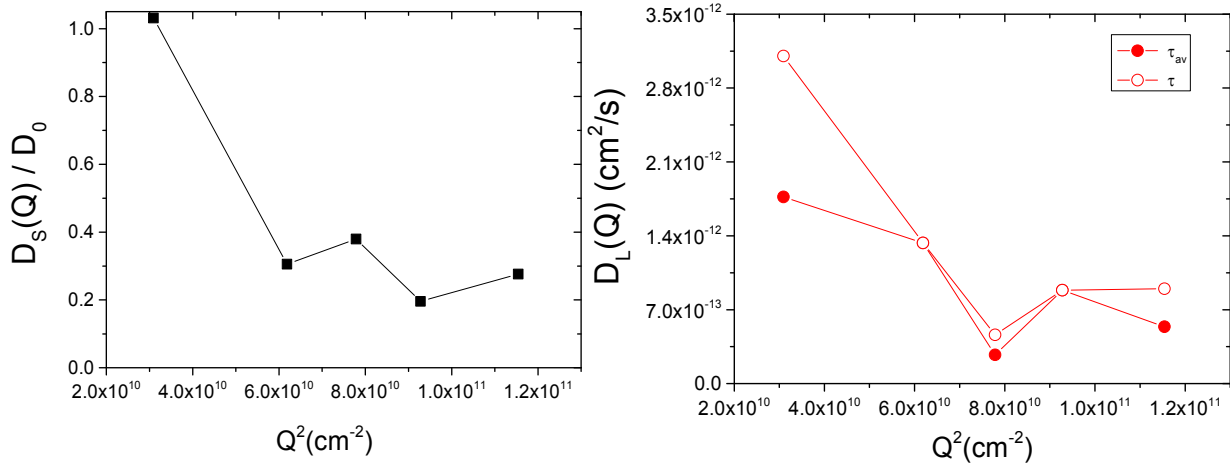

Figure 4.4 left: normalized short-time self-diffusion at different Q's and **(right)** long-time self-diffusion normalized with (open circles) and without (closed circles) the stretching factor β, from the correlations of figure 4.3

After the angular dependence, a time evolution of the degree of correlation ($c_I(t_w,\tau)$) at different delay times was measured. For a system in a steady state, the degree of correlation should be constant with waiting time. When $c_I(t_w,\tau)$ increases with time, the intermediate scattering function (or two time correlation function) $f(t_w,t_w+\tau)$ becomes slower, and vice versa. Figure 4.5 depicts the degree of correlation for P2_41k at c/c*=0.81 after rejuvenation. For the sake of clarity only 7 out of 116 delay times are shown. Our data cover a broad range of 11 decades in time, and we follow the slow dynamics over about 7 decades in relaxation times (figure 4.6). For the early times the degree of correlation exhibit an initial fast increase reaching a plateau at $t_w \sim 10^4$s resulting to a slowdown of the slow relaxation mode in $f(t_w,t_w+\tau)$ by about three decades, while the fast process linked to in-cage diffusion (cooperative nature) changes slightly. Surprisingly after $340*10^3$ s (~4 days) the $f(t_w,t_w+\tau)$ slows down (i.e. the relaxation becomes faster) and the system reaches a second and possibly final steady state. At the same time the fast process increases in amplitude while the fast relaxation becomes also slightly faster.
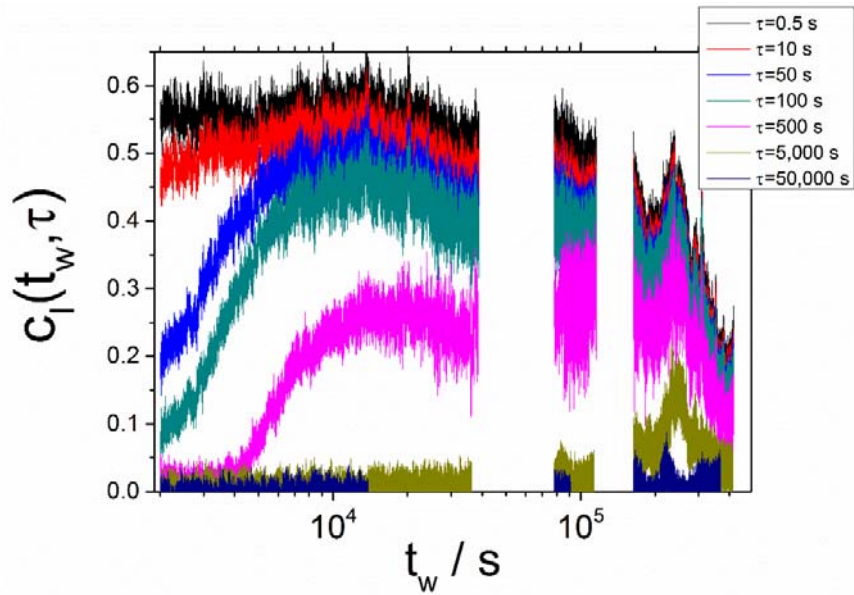
Figure 4.5: Degree of correlation at different delay times **for P2_41k at c/c*=0.81**

Moreover, there is an additional process in the correlation functions close to the glass-crystal re-entrant. Such an extra process was also revealed in the surfactant micelles examined by Imai et. al. (Imai, Kurimoto et al. 2012) (figure 4.6). The absence of non-ergodic plateau proves that the concentration fluctuations relax totally over this length scale via the observed two modes; the short and the long time self-diffusion.
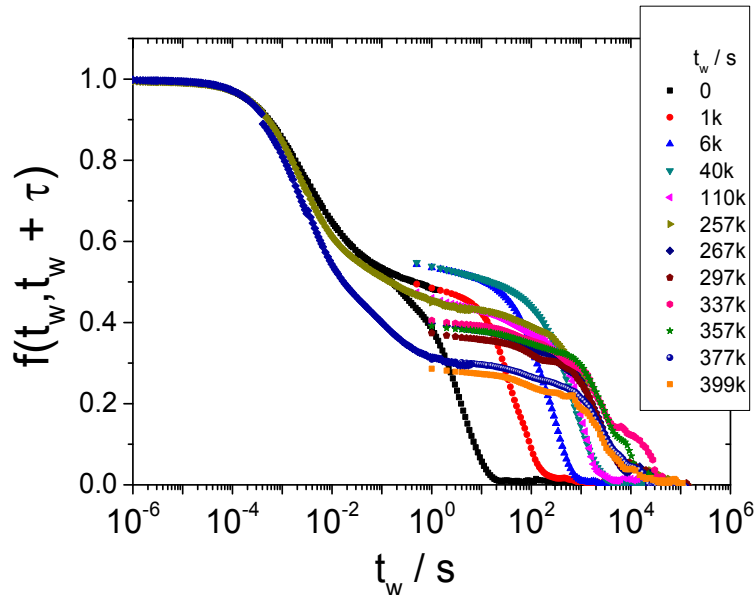
Figure 4.6: Two-time intermediate scattering function obtained from degree of correlation in fig. 4.5

We present in figure 4.7 the evolution of the slowest relaxation time at Q=0.025nm^{-1} extracted from the KWW fits to the ISF. An initial fast increase of the slow relaxation process is revealed for the first 30,000 s. Then there is a slower increase of the relaxation time until 3*10^{5}s followed by a sharp increase that reaches almost four times higher, with the maximum relaxation time around 330,000 s. Beyond this point the relaxation time speeds up and the system starts to crystallize. At 400k s the system is (almost) fully crystalline as it is depicted from the figure below (4.7 right). Such a behavior, has been reported recently by our group in star-polymers where the slowest process related to in-cage diffusion speeds-up due to creation, locally, of larger free volume via ordering of the stars.
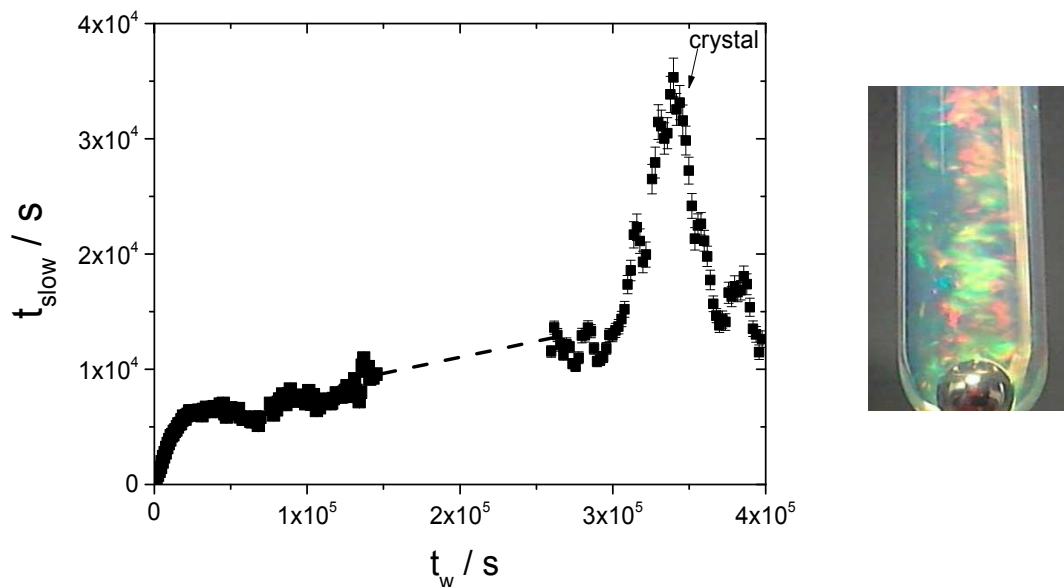
Figure 4.7 left: Age dependence of the slowest relaxation of P2_41k at c/c*=0.81 **right:** picture of the sample after the age dependence.

By further increasing the concentration at c/c*=0.94 the dynamics become slower and the system is strongly non-ergodic. The degree of correlation (figure 4.8) show an initial fast increase with t_w, i.e. the dynamics slow down. After 20,000 s the evolution of the dynamics essentially stops and a nearly stationary state is reached. Figure 4.9 left shows the two-time ISF obtained by averaging the c_I (figure 4.8) over a time window from 3s (for the youngest ages) to 2000 s (for the oldest samples), for various t_w. After approximately 9 days (7.7*10^5 s) the system seems to crystallize, exhibiting a small speed-up of the slowest relaxation. The sample

again crystallized as it is clearly seen in figure 4.9 (on the right) confirming the glass-crystal re-entrant transition. Here we have to notice that the kinetics of crystallization were very slow, with the relaxation essentially reaching the limit of the experimental setup ($\tau_{slow} > 10^5$ s) while the system is strongly non-ergodic with a plateau of about 0.9.
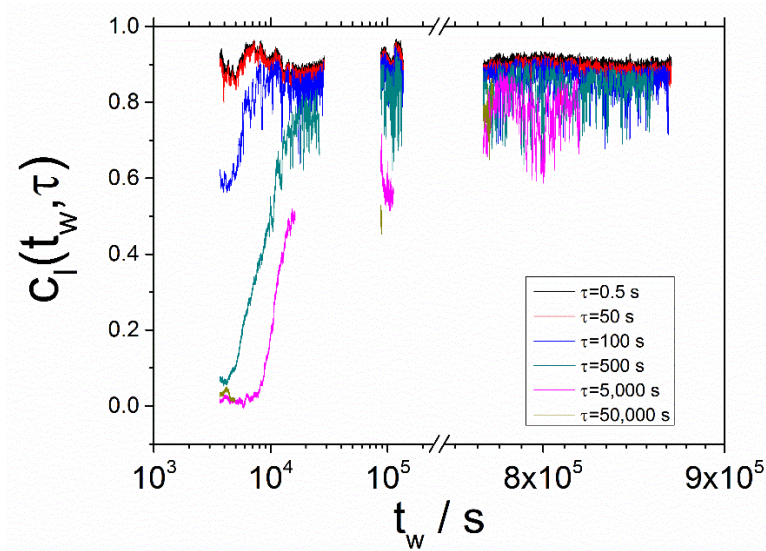
Figure 4.8: Degree of correlation at different delay times **for P2_41k at c/c*=0.81**
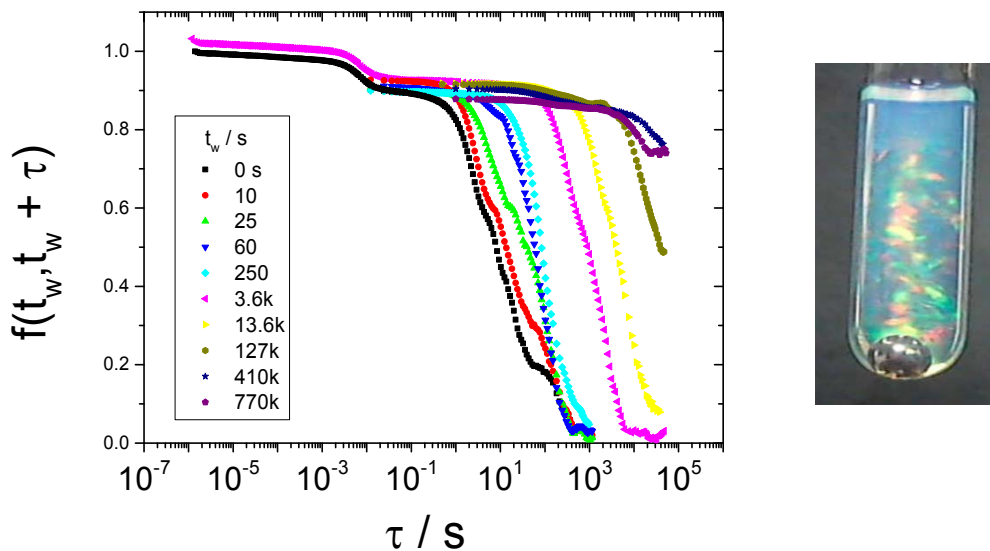
Figure 4.9: Two-time intermediate scattering function obtained from degree of correlation in fig. 4.8

At c/c*=1 the system is completely frozen with the dynamics being very slow and any attempt to calculate the two-time ISF after 50k s is almost impossible. The system remains strongly non-ergodic, with the slowest relaxation process out of our experimental window while even 50 days (4.3 million seconds) after rejuvenation (figure 4.10) there is no indication of crystallization.
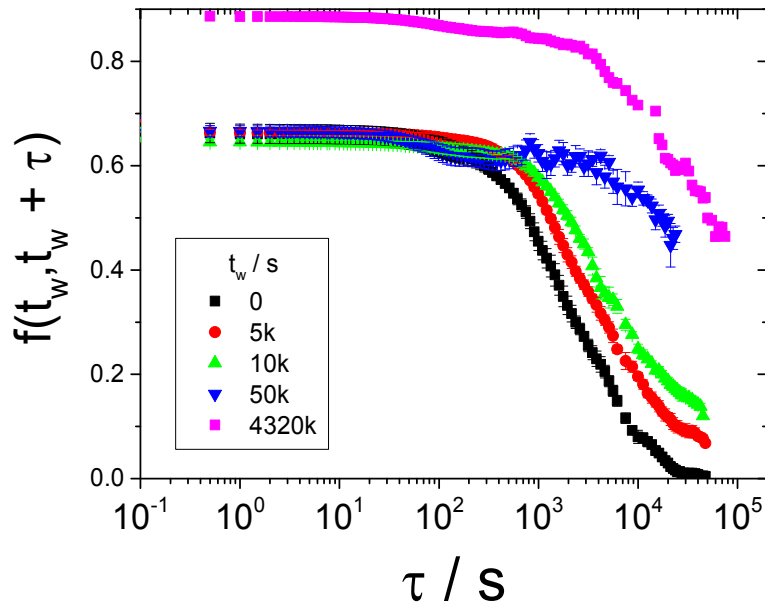
Figure 4.10: Two-time intermediate scattering for P2_41k at c/c*=1.

At these high volume fractions the system has strong internal stresses as it is also observed from rheological measurements (see chapter 5). The sample shows a typical glass like behavior without terminal relaxation. The residual stresses (figure 5.21) remaining on the sample after shear (in this case through rejuvenation) are significant with the system unable to fully relax. The amplitude of the slowest relaxation process is increased, indication of the significant slowing down of the in-cage diffusion and the absence of any out-of-cage diffusion.

The bigger and softer (P2_402k)

We next discuss the multispeckle measurements on the bigger and softer particle. Figure 4.11 shows the angular dependence of P2_402k at c/c*=0.94, after rejuvenating the sample with the same way as P2_41k. We observe two distinct relaxation processes. The fast, related with in-cage diffusion exhibits a Q-dependence, reminiscent of concentrated suspensions, with $D(Q)/D_0$ to decrease as we increase Q due to effect of thermodynamic interactions (S(Q)) and hydrodynamic (H(Q)) effects (figure 4.12). The slowest process has a rather Q-independent D(Q) , indicative of diffusive ultraslow dynamics commonly observed in many soft matter systems. (Cipelletti 2005).
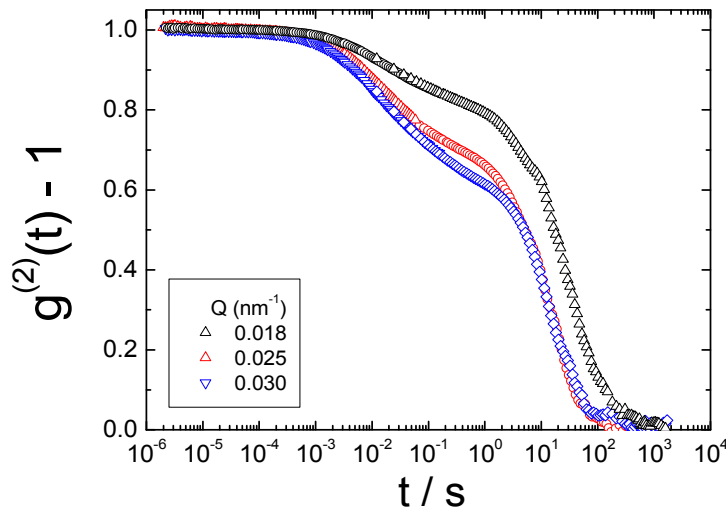
Figure 4.11: Angular dependence of the intermediate scattering function (ISF) for P2_402k at c/c*=0.94 before ageing.
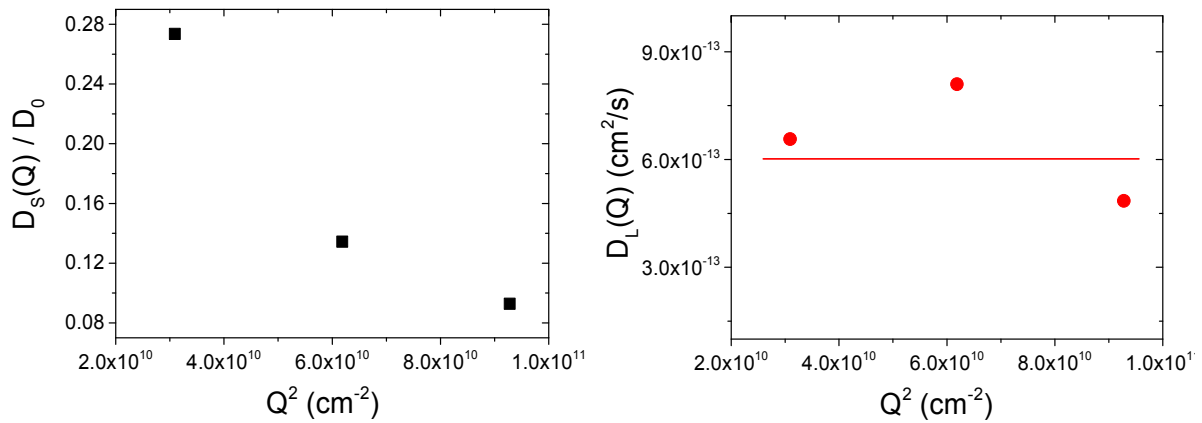
Figure 4.12: left: normalized short-time and **(right)** long-time self-diffusion at different Q's, from the correlations of figure 4.3

Figure 4.13 shows the two-time intermediate scattering function (ISF) for the rejuvenated sample. At t=0 the slowest relaxation process has a relaxation time $\tau \sim 100$ s, which increases three decades within one day of waiting time ($t_w \sim 10^5$ s). The relaxation time was out of our experimental window for almost a period of 27 days (~ 2.3 million seconds), when a speed-up of the slowest relaxation process started to reveal (see figures 4.13 and 4.14). Moreover the plateau between the two relaxation processes dropped to 0.2, indicating that the in cage diffusion become the dominant process and the cage on the average increase in size. After the speed-up the sample's dynamics continued to age, as we can observe from the relaxation process at t_w=2,301k s and 2,350k s, probably due to crystal restructuring. The speed-up is related with a glass-crystal re-entrant, similar to what has been observed for the smaller and harder particle.

Figure 4.13: Two-time intermediate scattering function obtained from degree of correlation at different delay times.

On the right of figure 4.14 we show the sample after the speed-up of the relaxation. For this specific system a mixture of FCC,HCP crystal was expected to be formed, similar to what has been observed in crystal phases in our light scattering experiments as well as confocal laser scanning microscopy experiments performed by Ohno et al. (Ohno, Morinaga et al. 2007).
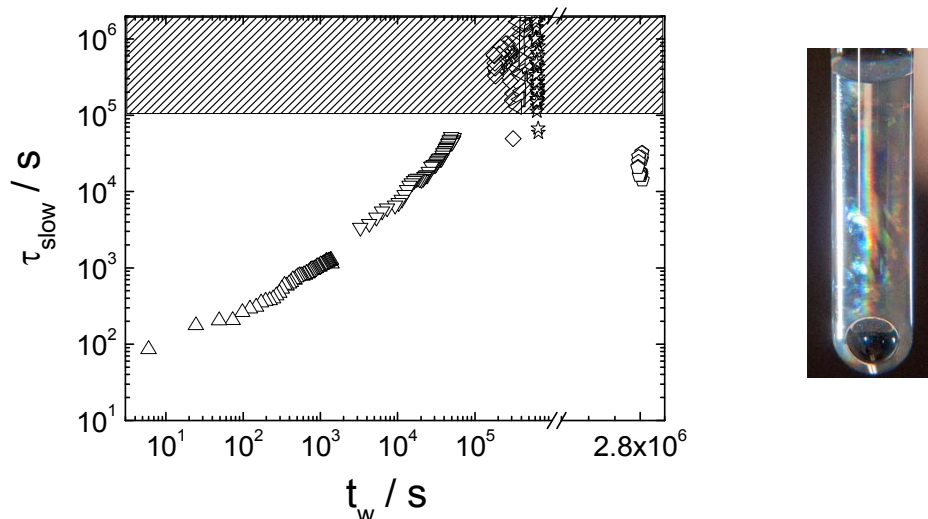
Figure 4.14: left: Age dependence of the slowest relaxation of P2_41k at c/c*=0.81 **right:** picture of the sample after the age dependence. The patterned area at $\tau > 10^5$ s is out of experimental window.

By increasing the effective volume fraction to $c/c^*=1.05$, a similar behavior was observed (figure 4.15). The sample is strongly non-ergodic with the slowest relaxation time progressively increasing by increasing the waiting time, while the non-ergodic plateau also increases. The slowest relaxation time increases non-monotonically with t_w; around $t_w \sim 35,000$ s (figure 4.16) it goes outside the stability limits of the measurement.
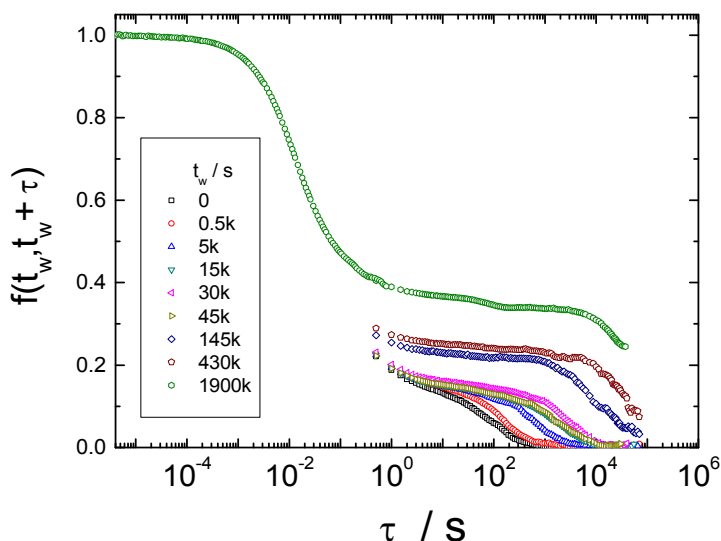
Figure 4.15: Two-time intermediate scattering function obtained from degree of correlation at different delay times.

After ~150k s, the relaxation time becomes extremely slow and we were unable to fully capture the correlation function. This extra low process remained out of our experimental window for 22 days, where an extra process revealed ~200 s, and the sample started crystallizing (figure 4.16). In the case of P2_402k the QR-values studied are higher and we directly observe the in-cage or out of cage self-diffusion. A possible explanation is that the in-cage diffusion becomes faster as the sample crystallizes, with the extra ultraslow process revealed, linked to a slow restructuring of the crystal. The appearance of asimilar additional process has been reported by Cipelletti et al. (Cipelletti and Ramos 2005) in soft systems.

123
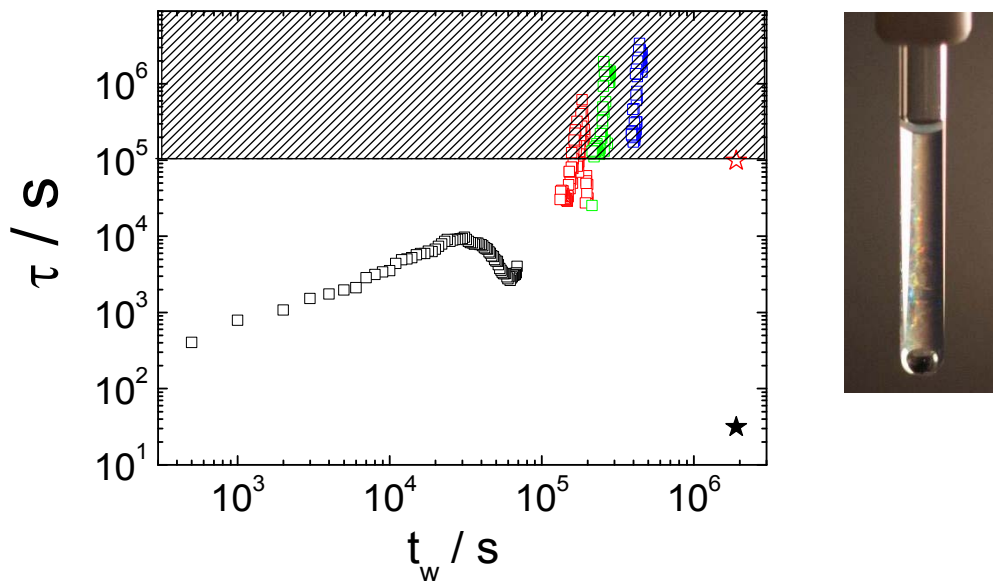
Figure 4.16: left: Age dependence of the slowest relaxation of P2_41k at c/c*=0.81 **right:** picture of the sample after the age dependence. The patterned area at $\tau > 10^5$ s is out of experimental window.

At the highest volume fraction measured in this system (c/c*=1.15), there is strong interpenetration with the sample kept trapped in a metastable glassy state while the system ages with waiting time (figure 4.17). Beyond t_w= 40k s the slowest relaxation time is getting out of our experimental window, with the system continuing ageing without any crystallization observed even after 26 days (~2.2 million s).
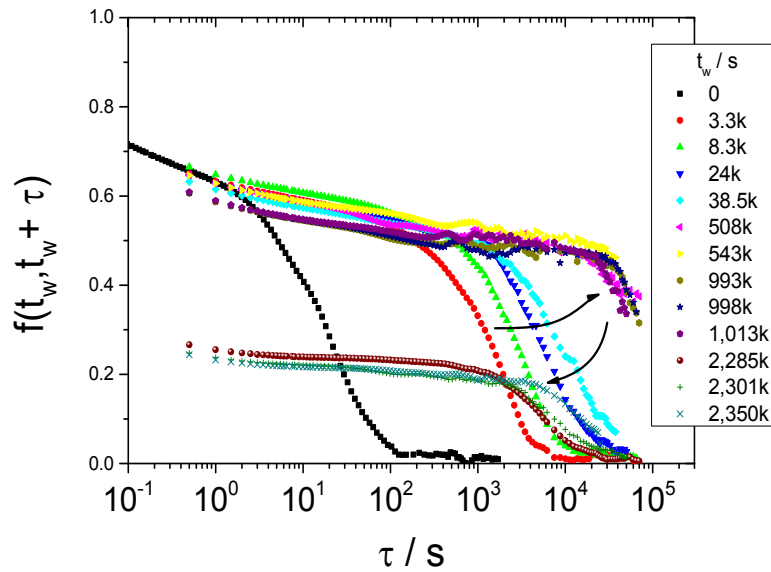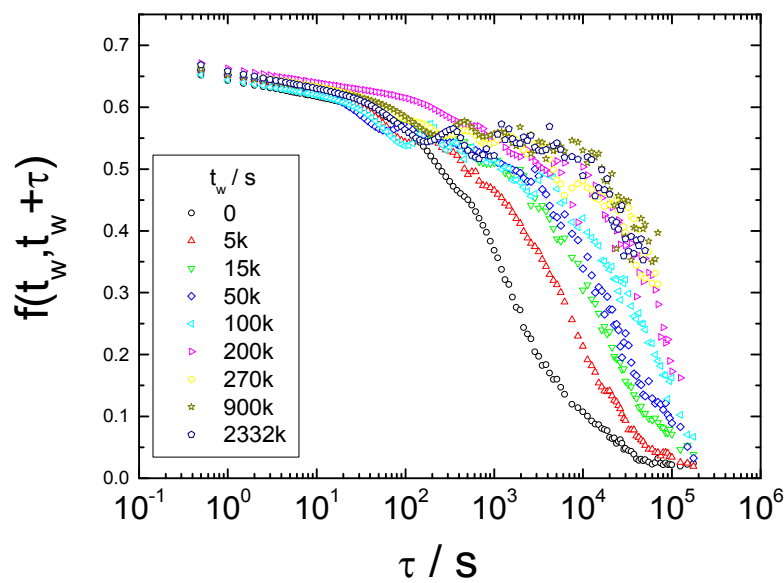
Figure 4.17: Two-time intermediate scattering function obtained from the degree of correlation at different waiting times, t_w.

Figure 4.18 show the D(Q), for the three systems studied from the liquid and well inside the glass regime. Top figure shows the smaller and harder particle, P2_41k. The data in the liquid regime (c/c*< 0.6) are from Bogri et al.[5] The middle figure shows data for the intermediate particle, P2_126k and the bottom figure presents data from the larger and softer P2_402k. The normalized volume fraction dependence of $D(Q)/D_0$ in the liquid regime for 126k and 402k were discussed in the previous chapter (chapter 3).

For P2_41k, D(Q) is extracted at the highest Q which is around the minimum of D(D) (Q=0.0268 nm^{-1}), due to limitation of the Q-range, since the particle is relatively small (R_H=130 nm). As we increase c/c*, D(Q) slows down, similar with hard spheres (red line) as it is predicted by Brady et al. through Accelerated Stokesian Dynamics (ASD) simulations (Banchio and Brady 2003). By continue increasing c/c* moving inside the glass regime, two relaxation modes were observed, The fast one, corresponds to short-time in-cage diffusion (red circle) and the slow process which corresponds to long-time out of cage diffusion. Even though at c/c*=0.81 the system is deep in the glass regime, $D(Q)/D_0$ has slightly higher value compared to the D(Q) in the liquid regime at c/c*=0.56. Such a discrepancy can be attributed to the slightly different measured Q between liquid (Q=0.0268 nm^{-1}) and glass regime (Q=0.025 nm^{-1}). The long D(Q) (red up triangle) is almost 5 decades slower compared to short D(Q), at t_w=0 s and becomes even slower as the sample ages. Similarly by increasing the concentration (c/c*=0.94) the system goes deeper in the glass regime, with the long $D(Q)/D_0$ reaching values as low as ~10^{-8}.

For the intermediate particle (P2_126k), the behavior is similar. The dynamics in the liquid regime slow down as we increase c/c* up to the crystal phase (c/c* (liquid-crystal) = 0.52), where we were not able to measure D(Q) any more due to strong scattering intensity from the crystal peaks. By moving into the glass regime, two modes were revealed: short-time self-diffusion, $D_S(Q)$, (black squares) and long-time self-diffusion, $D_L(Q)$, (triangles). Similarly with the previous system, by increasing t_w $D_L(Q)$ slows down significantly, reaching a pseudo steady state with $D(Q)/D_0$~10^{-7}.

---

[5] Kindly provided by Bogri et.al.

For the larger and softer P2_402k, $D_S(Q)$ in the liquid regime slows down with a smaller rate compared to the other particles, due to softer character (see chapter 3). Above c/c*=0.65 the system enters in the crystal phase with $D_S(Q)$ continuing to decrease with a similar trend. Here we were able to measure $D_S(Q)$ accurately in the crystal phase due to the high Q-limit (QR~11.5 for the highest measurable angle). In the glass regime two relaxation processes were observed: $D_S(Q)$ and $D_L(Q)$, with $D_L(Q)$ slowing down four orders of magnitude between t_w=0 s and t_w=53k s, going from $D(Q)/D_0$~10^{-4} to $D(Q)/D_0$~10^{-8}.
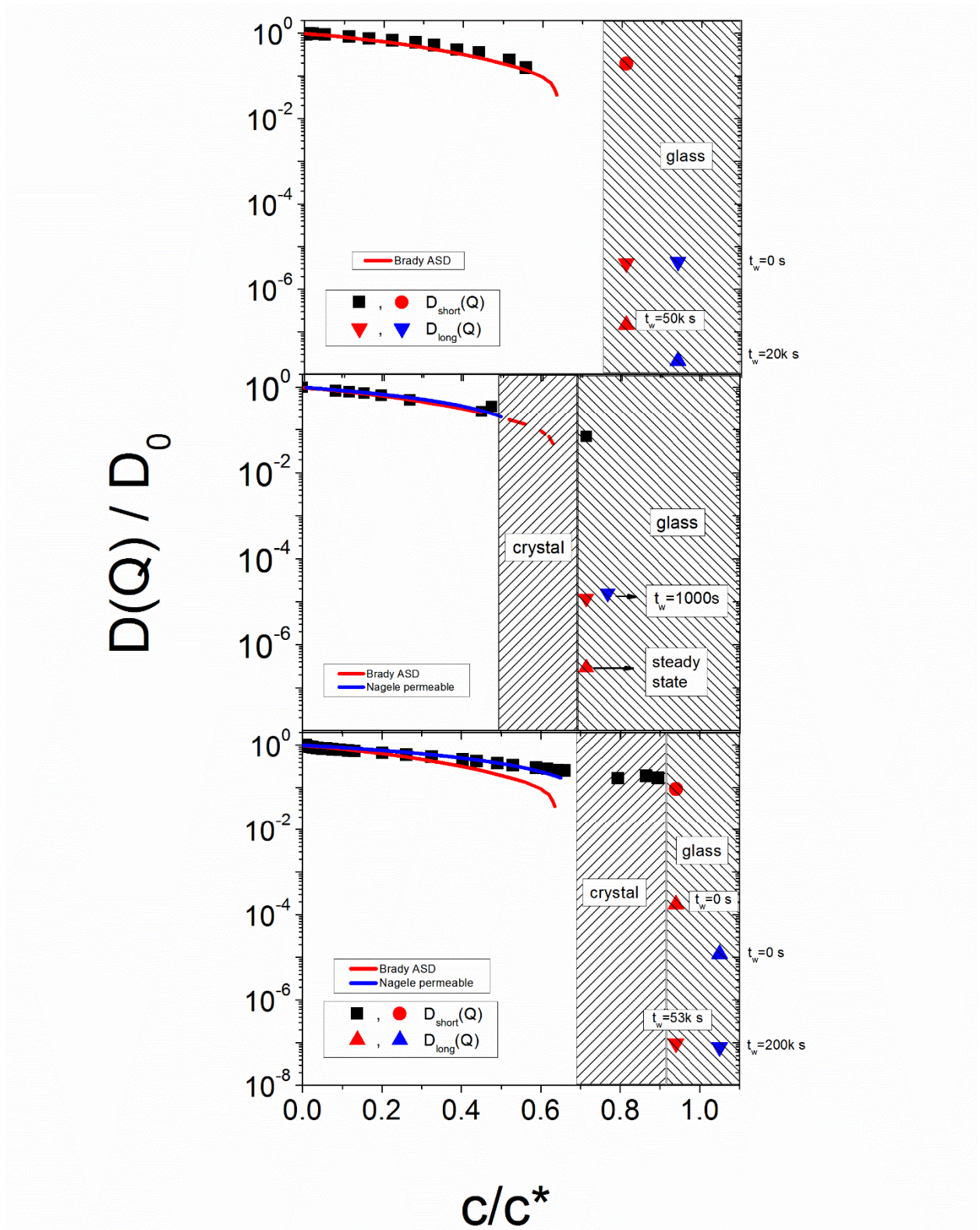
Figure 4.18: normalized D(Q) for all systems studied. From top to bottom: P2_41k, P2_126k and P2_402k. Lines correspond to hard (red line) and permeable (blue line) sphere theory.

4.4 – Conclusions

We have presented a clear experimental evidence for the crystallization of soft core-shell particles. Despite the strong difference in the softness and the absence of the crystal phase (through observation tests and rheology) in the case of the smaller particle (P2_41k), both systems showed a clear glass-crystal reentrant transition. In all cases crystallization occurred through a progressively ordering of the particles in the glassy state. The speed-up of the dynamics is due to the large free volume they exhibit in crustal phase, with the particles to diffuse easier. At very high volume fractions the system remained trapped in the metastable glassy state due to strong residual stresses and interpenetration.

4.5 - References

Banchio, A. J. and J. F. Brady (2003). "Accelerated Stokesian dynamics: Brownian motion." The Journal of Chemical Physics **118**(22): 10323-10332.

Cipelletti, L. and L. Ramos (2005). "Slow dynamics in glassy soft matter." Journal of Physics-Condensed Matter **17**(6): R253-R285.

Cipelletti, L. a. R. L. (2005). "Slow dynamics in glassy soft matter." **17**(6): R253.

Foffi, G., F. Sciortino, P. Tartaglia, E. Zaccarelli, F. L. Verso, L. Reatto, K. A. Dawson and C. N. Likos (2003). "Structural Arrest in Dense Star-Polymer Solutions." Physical Review Letters **90**(23): 238301.

Imai, M., M. Kurimoto, F. Matsuura, Y. Sakuma and T. Kawakatsu (2012). "Diffusion of surfactant micelles in fluid and crystal phases." Soft Matter **8**(38): 9892-9905.

Masri, D. E., G. Brambilla, M. Pierno, G. Petekidis, A. B. Schofield, L. Berthier and L. Cipelletti (2009). "Dynamic light scattering measurements in the activated regime of dense colloidal hard spheres." Journal of Statistical Mechanics: Theory and Experiment **2009**(07): P07015.

NorPix, I. Streampix: High speed digital video recording software and solutions for single or multiple cameras.

Ohno, K., T. Morinaga, S. Takeno, Y. Tsujii and T. Fukuda (2007). "Suspensions of Silica Particles Grafted with Concentrated Polymer Brush: Effects of Graft Chain Length on Brush Layer Thickness and Colloidal Crystallization." <u>Macromolecules</u> **40**(25): 9143-9150.

Pamvouxoglou, A. (2009). <u>Dynamics and rheology in suspensions and glasses of soft colloids</u> Materials Science and Technology.

Pusey, P. N. (2008). "Colloidal glasses." <u>Journal of Physics-Condensed Matter</u> **20**(49): 6.

Stiakakis, E., A. Wilk, J. Kohlbrecher, D. Vlassopoulos and G. Petekidis (2010). "Slow dynamics, aging, and crystallization of multiarm star glasses." <u>Physical Review E</u> **81**(2): 4.

Watzlawek, M., C. N. Likos and H. Löwen (1999). "Phase Diagram of Star Polymer Solutions." <u>Physical Review Letters</u> **82**(26): 5289-5292.

Zaccarelli, E., C. Valeriani, E. Sanz, W. C. K. Poon, M. E. Cates and P. N. Pusey (2009). "Crystallization of Hard-Sphere Glasses." <u>Physical Review Letters</u> **103**(13): 135704.
`

4. Slow dynamics, ageing and Glass-Crystal Re-entrant in soft colloids

Chapter 5 Rheology in Si-PMMA core-shell particles: Effect of Particle Softness

5.1 – Introduction

Soft particles in glassy regime exhibit similar behavior with hard spheres such as non-ergodicity and caged dynamics. However, while hard sphere colloids can interact through excluded volume effects, soft particles that interact through an effective soft repulsive potential at high volume fractions can compressed each other with the fuzziness of the surface to play important role for the repulsive forces. We can divide them into two categories: particles with polymer shell cross-linked on the core (polymeric or not) and particles with polymer chains that are grafted on the core surface. In the first case interpenetration between the particles is negligible and the shell is mainly deforming under external stimuli. For the core- grafted shell particles, interpenetration can be strong depending on the effective density of the chains in the outer part of the shell. For the former category star polymers(Vlassopoulos, Fytas et al. 2001, Petekidis, Gapinski et al. 2004) and star-like micelles (Laurati, Stellbrink et al. 2007) are good representatives whereas for non-penetreable particles, microgels used due to deformable and T-responsive shell (Senff, Richtering et al. 1998, Deike, Ballauff et al. 2001, Fuchs and Ballauff 2005, Fuchs and Ballauff 2005, Crassous, Siebenburger et al. 2008, Carrier and Petekidis 2009, Siebenburger, Fuchs et al. 2009). Both categories show transition to the glassy state, mostly at higher volume fractions than Hard Spheres due to deformability and/or penetrability of the shell.

Over the last decade, numerous publications have been reported on rheology of soft colloidal systems, with emphasis on the flow behavior (Carrier and Petekidis 2009, Divoux, Barentin et al. (2011), Rogers, Erwin et al. 2011), non-linearities through Large Amplitude Oscillatory Shear (LAOS) experiments (Rogers, Erwin et al. 2011, Poulos, Stellbrink et al. (2013)) and softness effects on linear viscoelasticity (Koumakis, Pamvouxoglou et al. 2012, Romeo, Imperiali et al. 2012, Crassous, Casal-Dujat et al. 2013).

For the case of colloidal spheres, Mode Coupling Theory (MCT) (Brader, Siebenburger et al. 2010) can predict the Linear Viscoelasticity of concentrated suspensions, giving details for the structural changes in the system. MCT does not include the activating hoping mechanism (Kobelev and Schweizer 2005) which experimentally has been detected in hard sphere glasses yet is the most successful rigorous model for hard sphere colloids. For the soft systems, also Soft Glassy Model (SGR) (Sollich, Lequeux et al. 1997, Sollich 1998) describes general aspects of the rheology for highly concentrated spheres.

Soft particle glasses share common features with hard sphere glasses such as non-ergodicity and caged dynamics. As we increase the volume fraction, hard spheres become amorphous with the dynamics to be frozen. In soft spherical systems such as microgels (Miller and Kauffman 1989), by continue increasing the volume fraction, the system moves to a jammed state where the particles are in contact and compressed interacting via soft elastic repulsions.

Here we are focusing on measuring and understanding the linear and nonlinear rheological properties of soft colloidal systems. The softness in the core-shell systems of this study can vary by changing the molecular weight of the chains that are attached on the silica core. The rheology and yielding behavior has been examined by linear (dynamic frequency sweeps), nonlinear (dynamic strain sweeps, LAOS, flow curves) and transient (start-up and relaxation) experiments.

....

5.2 – Systems, Techniques and Methods

5.2.1 – Materials

The core-shell particles used for this work are the same with the particles used for the light scattering experiments (chapters 3-4). We preferred to use the solvent mixture of Veratrole-DMF for P2_41k and P2_402k and Veratrole for P2_126k. The average boiling point of the solvent mixture is around 180 ^{0}C and for Veratrole 210 ^{0}C. By using these solvents we were able to measure up to 16h for the solvent mixture and 24h for Veratrole, using our homemade trap system. Table 1 shows the samples used for the rheological experiments.
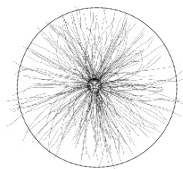
Sample name	R_H (nm)	Number of chains/ nm^2 (σ)	Number of chains/particle (f)	r_C / R_H	σ_{eff} outer blob	sketch
P2 41K	130 (Ver-DMF)	0.55	34500	1.00	0.138	
P2 126K	230 (Veratrole)	0.65	34500	0.62	0.052	
P2 402K	420 (Ver-DMF)	0.65	34500	0.305	0.016	

Table 1: Sample names and characteristics of the particles used for rheology

For all experiments performed in the three systems studied, we always started from the highest volume fraction and by dilution we were reaching the desired volume fraction. The highest volume fraction was reached after centrifugation at very high speeds (~8500*G) close to their RCP. Experiments for each sample were performed from a single batch, in order to secure the validity of the calculated volume fraction (c/c*). The mass fraction was calculated through thermogravimetric experiments (TGA), with accuracy of 10^{-2} mg.

The phase diagram of each sample was also determined by visual inspection. For P2_41k, we didn't observe any liquid-crystal coexistence, even though it exists as we have observed through MSDLS experiments (see chapter 4). The liquid-glass coexistence found to be between 0.75-0.81. For P2_126k the crystal –glass coexistence was at c/c*=0.7 and for P2_402k at c/c*= 0.94.

5.2.2 – Background – Rheology

Rheology is the study of deformation and flow of a material in response to an applied stress or strain. Simple solids store energy and provide a spring-like, elastic response, whereas simple liquids dissipate energy through viscous flow. For more complex viscoelastic materials, rheological measurements reveal both the solid and the liquid-like behavior depending on the time scale of internal relaxation processes.

When a force is applied to a volume of material (figure 5.1) then a deformation (D) occurs. If two plates (with area A) separated by simple liquid of thickness H, are moved relative to each other (at velocity V by a force F), Newton's law states that the shear stress (F/A) is proportional to the shear strain rate (V/H). The proportionality constant is known as the dynamic viscosity η
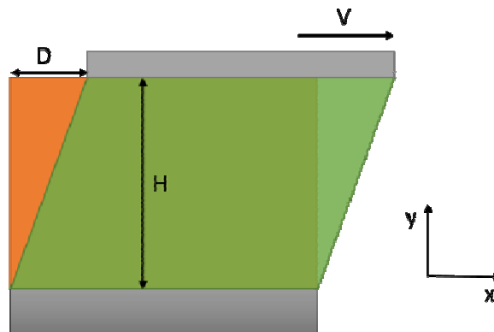
Figure 5.1: Schematic representation of a sample's deformation

In each geometry, the steady shear rate imposed on the fluid depends on a driving velocity and the dimensions of the geometry. For the cone-plate, which is used in these experiments, the shear rate $\dot{\gamma}$, is the velocity V (V= Ω*R) of the moving plate divided by the gap H , the height between the two plates , hence $\dot{\gamma} = V/H$. The shear stress σ is the force that a flowing liquid exerts on a surface per unit area of that surface, in the direction parallel to the flow. The shear viscosity η is then defined as

$$\eta = \sigma/\dot{\gamma}$$

In contrast for a solid-like fluid (Hookean) a shear stress applied to the surface results in an instantaneous deformation D (figure 2.4.1). Once a specific strain (deformed state) is reached there is no further movement, but the state reached persists as long as the stress is applied. The shear stress is then defined as

$$\sigma = G \cdot \gamma$$

here G is the shear modulus and γ the strain.

One way to characterize the rheological response of a system is to measure the rate of deformation (steady measurements) or to measure the shear moduli as a function of frequency (dynamic measurements). Another way to explore the rates of structural rearrangement within a complex dispersion, that does not significantly deform the fluid's microstructure, is to impose small-amplitude oscillatory shear. This kind of deformation can be achieved in a cone and plate geometry by rotating the one plate about it's own axis with an angular velocity that oscillates periodically in space $\Omega(t) = \Omega\cos(\omega t)$, where ω is the frequency of oscillation, in units of radians per second. The shear rate $\dot{\gamma}$ is a sinusoidal function of time $\dot{\gamma} = \Omega r / H$ and so is the shear strain $\gamma = \frac{\Omega_0 r}{\omega H}\sin(\omega t) = \gamma_0 \sin(\omega t)$. The ratio $\gamma_0 = \frac{\Omega_0 r}{\omega H}\sin(\omega t)$ is the strain amplitude. We usually use cone and plate geometry in order to have steady shear rate and strain throughout the sample.
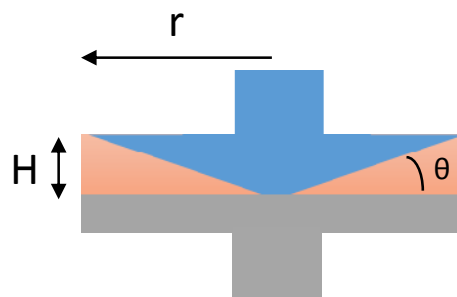
Figure 5.2: Cone and plate geometry

If the strain amplitude γ_o is small enough so that the dispersion structure is not disturbed by the deformation, then the stress measured during the oscillatory deformation is controlled by the rate of spontaneous rearrangements, or relaxations present in the dispersion in the quiescent or equilibrium state. The shear stress $\sigma(t)$ produced by a small amplitude deformation is proportional to the amplitude of the applied strain γ_o and is itself sinusoidally varying in time. In general, the sinusoidally varying stress can be represented as

$$\sigma(t) = \gamma_o[\, G'(\omega)\sin(\omega t) + G''(\omega)\cos(\omega t)\,]$$

where G' is the storage modulus and G'' the loss modulus. The storage modulus represents storage of elastic energy, while the loss modulus represents the viscous dissipation of that energy. When the ratio G'/G'' is high ($\gg 1$) the material has solid-like behavior but if G'/G'' is low ($\ll 1$) the material has liquid-like behavior. For soft material with a solid-like response the storage modulus is often nearly frequency independent. On the other hand on a liquid-like response, a simple Maxwell model often describe well the linear viscoelastic behavior with the frequency as $G' \sim \omega^2$, the loss modulus scales with the frequency as $G'' \sim \omega$, while the crossover frequency, ω_C, where $G'=G''$, signifies an internal long-time relaxation process in the system. The low frequency liquid-like region in which G' and G'' obey these power law is called the terminal regime (Ferry 1980).

Figure 5.3: Schematic representation of the loss modulus G' and storage modulus G'' for the systems which have solid-like and liquid-like behavior.

In order to quantify the effect of shear on a material, a dimensionless number is introduced, often used in colloidal systems and is a measure of t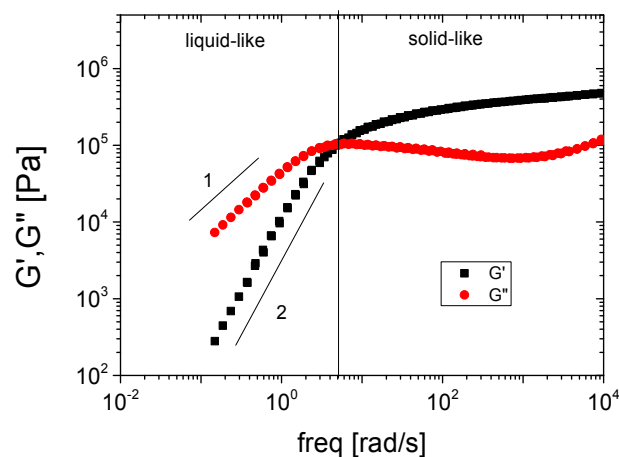he relative importance of the applied shear rate compared to the Brownian motion. The Peclet number, Pe, is defined as the shear rate $\dot{\gamma}$ multiplied by the Brownian time ($\tau_B = R^2/D_0$) i.e. the time needed for a particle to diffuse the distance of its own radius, where D_o is the free diffusion coefficient, $Pe = K_B T/6\pi\eta_s R^3$. Thus $Pe_0 = 6\pi\eta_s R^3\dot{\gamma}/K_B T$ is the free (bare) Peclet number, whereas when the φ-dependent D(φ) is used (often the short-time) we refer to the scaled (or dressed) Pe $Pe = R^2\dot{\gamma}/D(\phi)$. For Pe << 1, the Brownian diffusion is more important from the shear and the system can relax to its state at rest, even when it is sheared dominated. If Pe>>1, shear strongly affects the structure of the system before the latter can relax through Brownian diffusion.

5.2.3 – Experimental Setups

In the present work we used two rheometers: A Rheometrics Scientific (TA) strain-controlled ARES rheometer (with dual transducer with a measuring torque range 0.004-100 $gr \cdot cm$) and an Anton Paar MCR-501 stress control rheometer, with a very good strain control loop (applied torque range 0.01-100 $gr \cdot cm$). All the measurements were performed at 20 °C and 23 °C stabilized with a Peltier system in both rheometers.

To avoid evaporation during experiments, a homemade trap was used with excess of solvent vapors in order to saturate the atmosphere. Two different trap systems were constructed due to the difference in the motor and transducer position. For ARES rheometers (figure 5.4 left), the motor and transducer are separated with the transducer being at the top

part and the motor at the bottom of the plate. In this case the trap consists of two main pieces, a cylindrical aluminum piece which sits on the bottom plate and has a trough for putting in the sample solvent and a second piece which is fitted on the top plate. The two pieces are fitted in such way in order to avoid touching and at the same time providing a proper sealed and vapor saturated atmosphere. For measurements in Anton Paar stress controlled rheometer, both motor and transducer are placed at the top. An aluminum piece attached on the top plate, will increase the inertia of the tool and will decrease significantly the sensitivity when low torque values have to be measured. The trap consists only from one piece that is attached on the bottom plate. The gap between the plate and the trap is small enough in order to reduce as much as possible solvent evaporation. Furthermore the room temperature was kept constant, in order to avoid condensation of vapours on the cell.

For the experiments at P2_41k and P2_402k, we used homemade serrated plates due to strong slip. The slip was due to the solvent mixture with a refractive index matching the particle shell, which apparently reduces van Deer Walls forces between particles and the walls. All experiments were performed with cone and plate geometries with two different diameters 25 and 40 mm depending on the torque values.
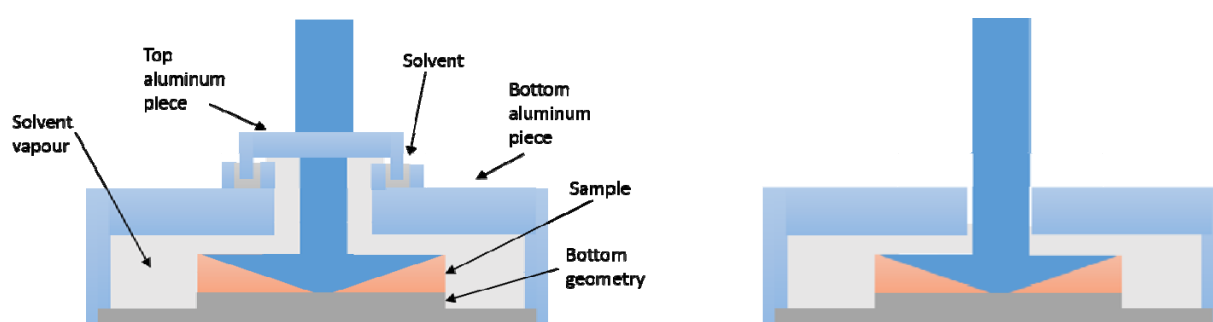

Figure 5.4: Representation of vapor saturation trap for ARES (left) and Anton Paar (right) rheometer.

Rejuvenation Protocols

The experiments for P2_41k and P2_402k were performed in Anton Paar stress-controlled rheometer. We impose a sinusoidal oscillation of ω= 1rad/s starting from 1000% strain down to

1%. Then we impose stress zero (σ = 0) and we monitored the value of the strain with time, which was always in the linear regime. The experiments of P2_126k were carried out in the ARES strain controlled rheometer. We performed a preshear at high rates ($\dot{\gamma} = 50\ s^{-1}$) for certain time (t=100 s). Then dynamic time sweep test with ω=1 rad/s and strain in the linear regime was used to follow the time evolution of the linear viscoelastic properties of the sample. If the values of G' and G" are constant, this suggests that the sample is at a steady state.

5.2.4 – FT Rheology

As the amplitude of the mechanical perturbation increases in oscillatory shear, non-linear effects become important. The shape of the stress oscillations can reveal a first indication of non-linear behavior (figure 5.5a). In the linear regime the shape should be perfectly sinusoidal and as the strain amplitude is increased the signal gets deformed. Stress vs strain (elastic Lissajous plots) (figure 5.5b) are useful also for understanding such non-linear effects. In the linear regime, if the stress response is purely elastic, the Lissajous plot should show a straight line whose slope determines the elastic modulus. If a response is purely viscous, then an ellipse should appear. In the case of a viscoelastic behavior, the shape should be a composition of the two, showing some sort of ellipsoid. LAOS measurements were performed with both rheometers and analyzed by Fourier Transformation of the stress signal.
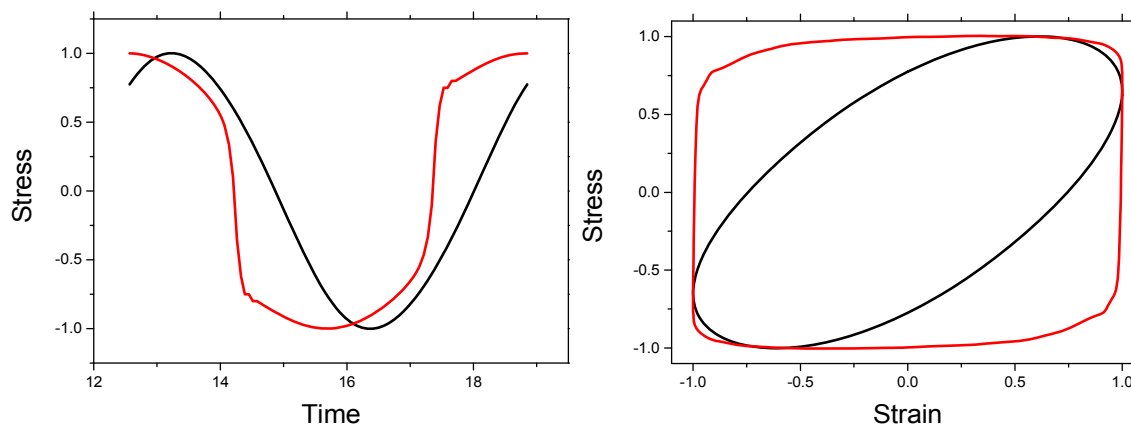
Figure 5.5: Shape of the stress oscillations extracted from a dynamic strain sweep with strain value below (black line) and above (red line) the critical yield strain. The units of both x and y axis are arbitrary downloaded directly from rheometer's output. **b)** Lissajous plot extracted from a dynamic strain sweep with strain value below (black line) and above (red line) the critical yield strain. The units of both x and y axis are arbitrary downloaded directly from rheometer's output.

5.3 – Linear Viscoelasticity

The simplest of the rheological characterization for the systems examined here is the dynamic frequency sweep tests. By imposing a deformation in the linear regime we can extract the elastic G' and viscous G'' components scanning at a large range of frequencies. Figure 5.6 reveals the elastic and viscous moduli for P2_41k for different volume fractions normalized with particle size (R_H) and thermal energy, in other words the Peclet number. These particle have dense polymer shell (35k chains/particle) with the molecular weight of each arm around 41 kg/mol and the overall size (R_H) of 130 nm. As has been reported earlier the hairs are expected to be fully stretched with the softness parameter $r_c/R_H=1$, indicating the whole particle to be in the Concentrated Brush Regime (CPB) (Ohno, Morinaga et al. 2006, Ohno, Morinaga et al. 2007).

140

From c/c* 1.20 down to 0.88 the system reveals an elastic response with G'>G" at all frequencies. The slope of G' is almost zero with a weak increase at high Peclet for the lower volume fractions. G" shows a minimum which moves in a non-monotonic way with respect to the volume fraction, as discussed below. The position at minimum of G" which is associated within MCT (Mason and Weitz 1995) with the transition between the in cage and out of cage relaxations, is a non-monotonic function of volume fraction. The smallest volume fraction (c/c*=0.75) shows a crossover point at Pe=0.06 where G'=G" and is becoming liquid-like (G">G') at lower Pe, although we do not get a typical Maxwell type response, probably due to low signal-to-noise.

Figure 5.6: Dynamic frequency sweeps for six different volume fractions for P2_41k in Veratrole-DMF solvent mixture. Solid symbols represent the elastic moduli, G' and open symbols the viscous moduli, G".

By increasing the softness (i.e. the attached chain molecular weight) using P2_126k in Veratrole solvent, the effective density on the outer part decreased 2.5 times. The grafted chains on the particles are not fully stretched and part of the shell has CPB to Semi-Dilute Polymer Brush regime (SDPB) (Ohno, Morinaga et al. 2006), with the chains near the end to have

141

conformation of a Gaussian coil. This fuzzy surfaces are more penetrable and the effective volume fraction is reached higher due to squeezing of the outer shell and chain interpenetration. Figure 5.7 depict the elastic and viscous moduli of P2_126k. Between 1.30<c/c*<1.15, G'>G'' and the slope of G' becomes smaller with increasing c/c*. At lower volume fractions G' tends to reach G'', with the terminal regime to be out of the experimental window.

Figure 5.7: Dynamic frequency sweeps for five different volume fractions for P2_126k in Veratrole solvent. Solid symbols represent the elastic moduli and open symbols the viscous moduli.

Further increase of the softness by using bigger particles (P2_402k) will decrease the effective density of the outer blob nine times with respect to P2_41k. Particles can interpenetrate more at these high volume fractions and the effective volume fraction is extended up to c/c*=1.66. Figure 5.8 shows the dynamic frequency sweeps for P2_402k in Veratrole-DMF solvent mixture. Values of G' are higher of G'' for all volume fractions. The slope of G' is small at different frequencies (Peclet). The G'' minimum moves to lower Peclet numbers as we decrease the volume fraction and remains constant below c/c*=1.47
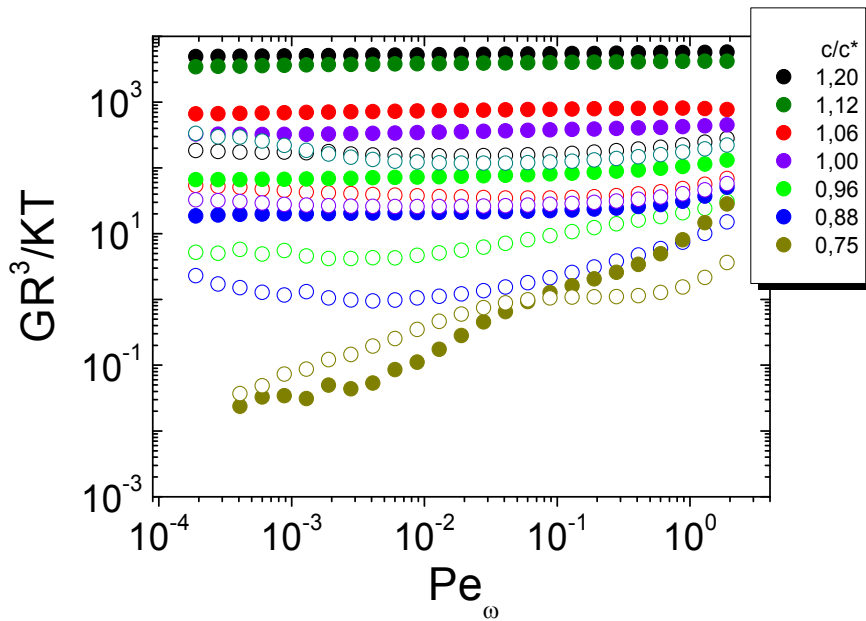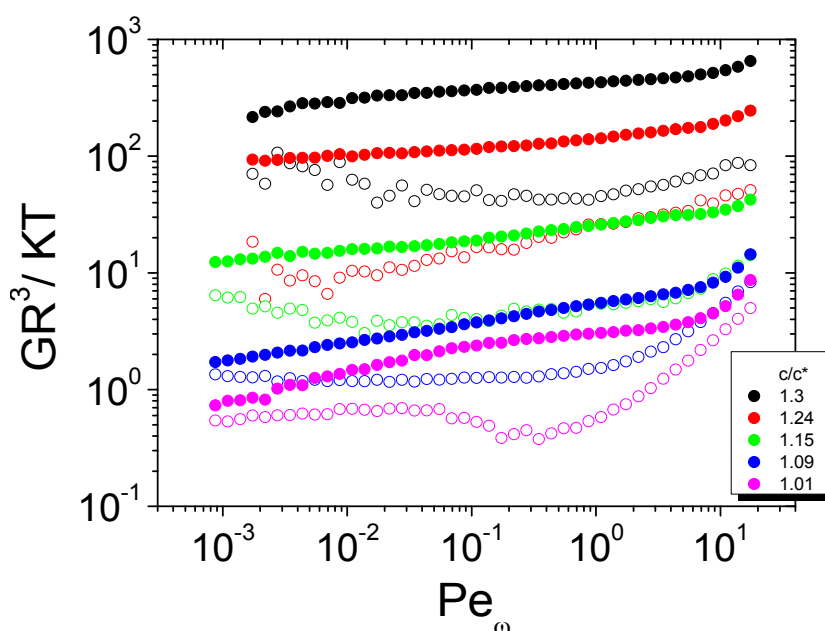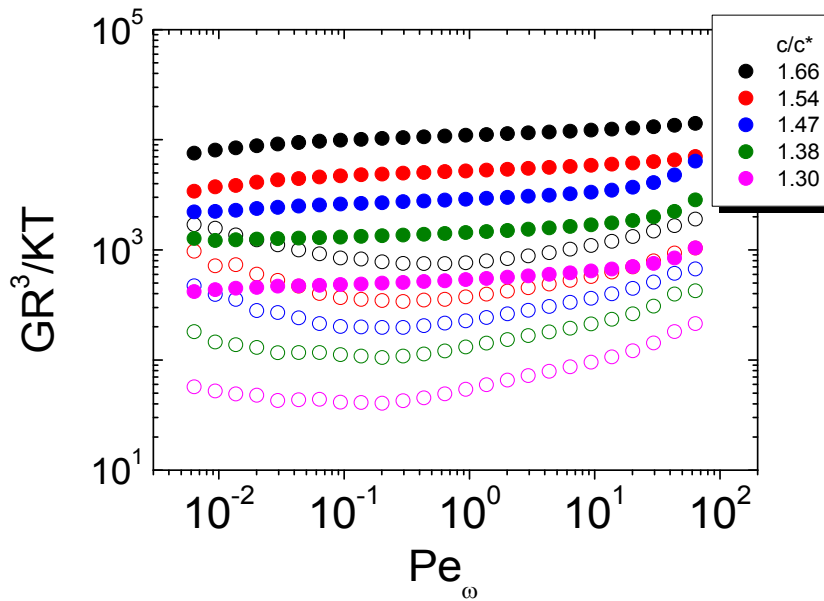
Figure 5.8: Dynamic frequency sweeps for six different volume fractions for P2_402k in Veratrole-DMF solvent mixture. Solid symbols represent the elastic moduli and open symbols the viscous moduli.

In figure 5.9a the normalized elastic moduli is shown while figure 5.9b shows the scaled relaxation time at the minimum of G" as a function of c/c* for all three systems in a log-log plot. In figure 5.9a the slope of G' with respect to the volume fraction maybe related with the interparticle potential (Paulin, Ackerson et al. 1996). For comparison we have plotted the slope of HS (Koumakis, Schofield et al. 2008) in the same diagram. Since the average distance between particles is related to the volume fraction and $G'|_{f_{high}} \sim \left(\dfrac{1}{r}\right)\left(\dfrac{\partial^2 U}{\partial r^2}\right)$, with G'~φ^m there is a predicted interparticle potential U ~ r^{-n} for m=1+n/3. For the smaller particles (P2_41k) the slope is m=22, similarly to the slope for P2_126k and P2_402k in the c/c* range of 1.1-1.3 and data superimpose. In all cases a two-step slope is observed. The change of the slope could be related with interpenetration/ or shrinkage, an effect that has been reported in several soft colloidal systems (Koumakis, Pamvouxoglou et al. 2012, Romeo, Imperiali et al. 2012). The slope of P2_126k at higher volume fractions is m=23 and is the same with the slope from P2_402k at lower c/c*. The frequency spectra are identical at the same volume fraction if we plot the

normalized elastic and viscous moduli as a function of Peclet. At higher volume fractions the slope of G' decreases, becoming m=12 (P2_402k). This difference in the trend of G' slopes at different particles can be connected with the absence of SDPB regime in the smaller particle, which behaves more as Hard Sphere.
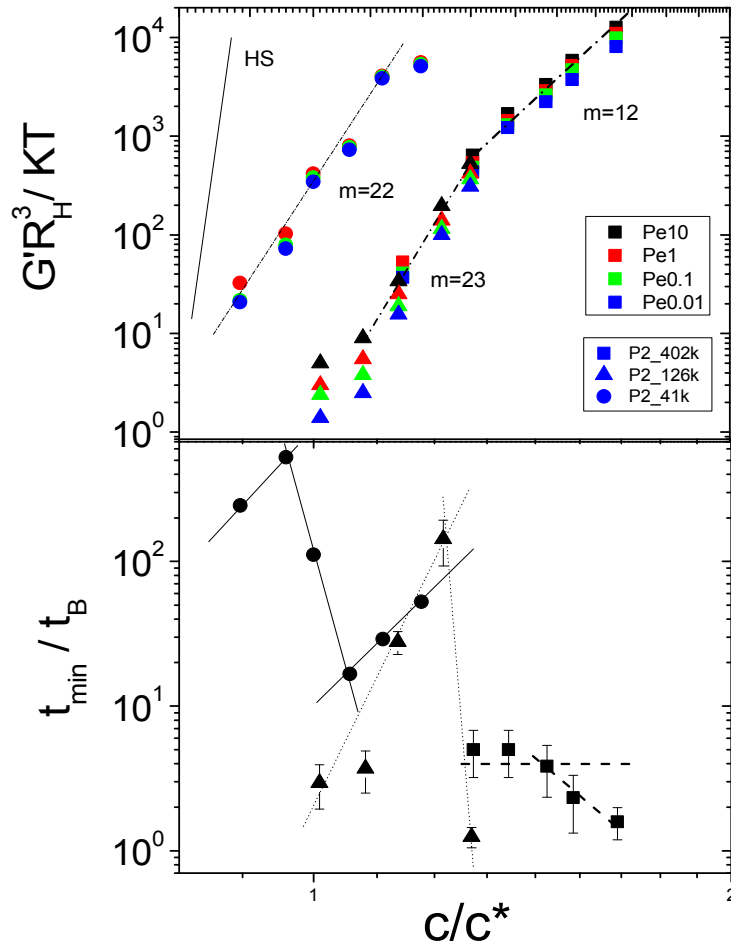
Figure 5.9: a) Values of scaled elastic moduli at different Peclet for the three systems studied as a function of the effective volume fraction. Dashed and dotted lines denote the slope of G' which reflects the interparticle potential and solid line the slope for HS. **b)** Values of the scaled relaxation time which, extracted from the minimum of G'' which is related to the transition from α to β relaxation, for the three systems.

The hard sphere systems examined by Petekidis et al. (Petekidis, Vlassopoulos et al. 2003), Koumakis et al. (Koumakis, Schofield et al. 2008, Koumakis, Pamvouxoglou et al. 2012) and Legrand et al.(Le Grand and Petekidis 2008) have yielded exponents of m_{HS} = 50. Systems

with softer interactions are known to exhibit smaller exponents. Star polymer examined by Ozon et al. (Ozon, Petekidis et al. 2006) have m_{stars} = 5.7 and soft core-shell particles of Deike et al. (Deike, Ballauff et al. 2001) and Senff et al.(Senff, Richtering et al. 1999) have m_{core} = 4-4.9 . In similar system Stieger et al. (Stieger, Pedersen et al. 2004) found an exponent of $m_{microgel}$ = 4.2 and $m_{microgel}$ = 8.3 by changing the cross-linking density . Also the nanoparticles of Rao et al. (Rao, Kobelev et al. 2006) which approach hard interactions exhibit m_{nano} = 17. In the work of Koumakis et al. (Koumakis, Schofield et al. 2008) is found in the shear-induced crystal state an exponent of $m_{HScrystall}$ =12-21 depending on the frequency. Thus our system behaves in between hard spheres and soft microgels due to the very big and dense polymeric corona. The P2_126k at low volume fractions may exhibit an exponent m = 8 which is close to the potential observed from Stieger et al. for highly cross-link microgels and hard interaction nanoparticles examined by Rao et al. , but more measurement are required to establish this trend.

The scaled relaxation time extracted from the minimum of G" in figure 5.9b is related with the transition from α (in-cage) to β (out-of-cage) relaxation (Segre, Behrend et al. 1995) , or the characteristic time for a particle to explore its cage. For the harder particle, P2_41k, as the volume fraction increases the relaxation time increases. Above c/c*=0.96 the relaxation time decrease and from c/c*=1.06 and above it rises again. The first maximum of the relaxation time at c/c*=0.96 can be attributed to the random close packing or jamming, reminiscent to what is reported on hard spheres approaching the glass transition (Segre, Behrend et al. 1995). The relaxation time becomes faster as we go above the glass transition, since the cage dimensions become smaller with increasing volume fraction. The additional increase of the relaxation time beyond c/c*=1.06 can be attributed to stronger particle interpenetration (or shrinkage).

For P2_126k we observe that the relaxation time becomes longer as we increase volume fraction up to c/c*=1.24 and then speeds up when entering a jamming state, similarly to P2_126k but at different absolute values of c/c*. This is probably due to different particle softness. For the bigger particle (P2_402k) the relaxation time remains constant possibly due to cancelation of effects from particles' shrinkage and is increased up to c/c*=1.47 and then becomes faster most probable due to jamming transition.

5.4 – Nonlinear Large Amplitude Oscillatory Shear (LAOS)

The nonlinear oscillatory response of P2_41k in Veratrole-DMF solvent mixture at various volume fractions and frequencies is shown in figure 5.10. Initially G' and G'' are constant up to 1-2 % strain, denoting the linear regime.

Figure 5.10: Dynamic strain sweep for P2_41k at six different effective volume fractions at 0.1 rad/s (a), 1 rad/s (b) and 10 rad/s (c). Arrows denote the yield strain defined as G'=G''

The crossover strain (γ_y at G'=G'') is the strain above which the sample shows a viscoelastic liquid-like behavior, although not necessarily that of a simple Newtonian fluid. G' and G'' plot

here were only the 1ˢᵗ harmonics of the stress, and higher harmonics are present in the nonlinear regime. The values of G' and G" decrease as we decrease the volume fraction. One measure of the yield strain is at G'=G".

Figure 5.11: Dynamic strain sweep for P2_126k at five different effective volume fractions at 0.1 rad/s (a), 1 rad/s (b) and 10 rad/s (c). Arrows denote the yield strain defined as G'=G"

This is indicated to a non-monotonic behavior with c/c*. The power-law dependence (straight lines in the figure 5.10) of both G' and G" at strains above the yield strain have roughly the same dependence with the hard spheres (Sollich 1998, Derec, Ducouret et al. 2003, Miyazaki, Wyss et al. 2006), with the slope of G' being almost twice that of G". At c/c*=0.88 for ω=1 rad/s and

strains γ>500% G" tends to a plateau (blue open symbols). This plateau indicates that the viscosity is constant independent of γ and therefore γ have reached a simple fluid response.

The plateau of G" at higher strains is more pronounced in P2_126k (figure 5.11), where it is observed for all volume fractions and frequencies. Especially at 10 rad/s we observe plateau of both moduli and at volume fractions above 1.14 G' and G" exhibit a weak increase of peak indicating weak shear-thickening. For such high volume fractions shells of the particles interpenetrate and grafted start being entangled. The particles are well entangled and interpenetrable in the outer shell. This causes an increase of the stress when the system is sheared at high strains (shear thickening) and the particles have to disentangle before flow. The linear regime extended up to 5% strain at all volume fractions and frequencies and the crossover point varies from 5 to 15%.In figure 5.12 we show G' and G" with increasing strain amplitude at different volume fractions and frequencies (P2_402k). The linear regime extended up to about 2% strain depending on frequency and volume fraction. The crossover yield point, γ_y is around 6-10% strain and is almost constant with volume fraction while it varies with frequency. Above the yield strain G">G' and both decrease linearly with strain. A two-step power law is observed with the slope changing around γ_0 = 100% strain. This change seem to take place at all frequencies but is more pronounced at 1 rad/s. Above this critical strain, the system is totally shear melted with both moduli reaching constant value, independent of strain amplitude.
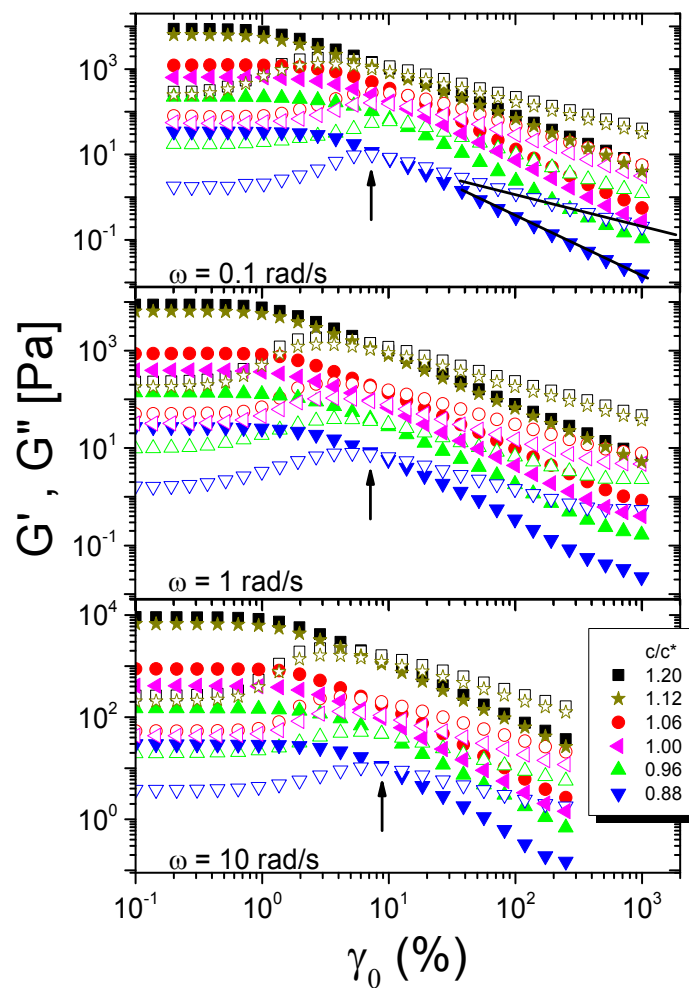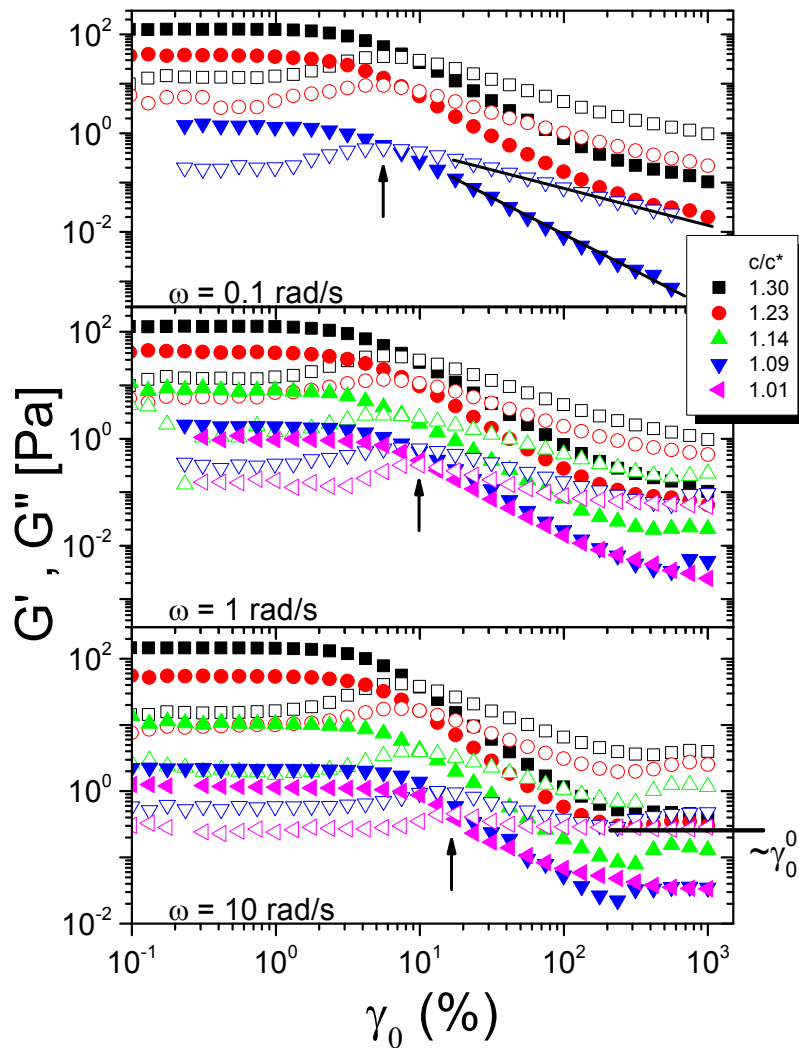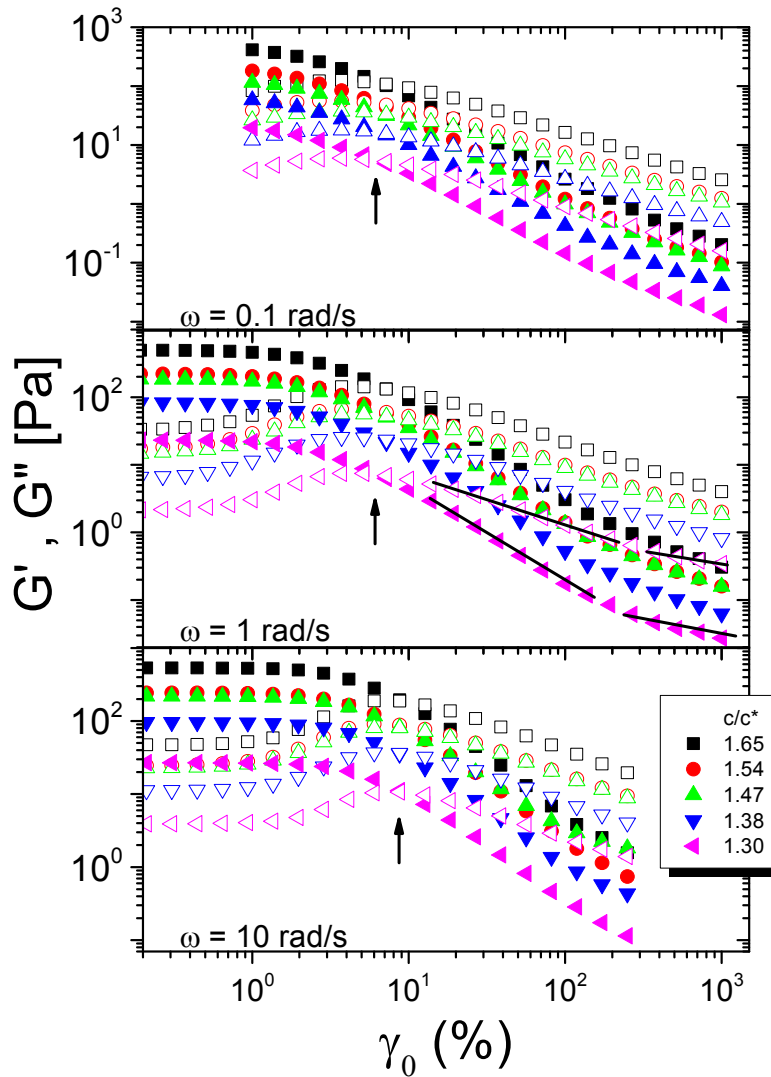
Figure 5.12: Dynamic strain sweep for P2_402k at six different effective volume fractions at 0.1 rad/s (a), 1 rad/s (b) and 10 rad/s (c). Arrows denote the yield strain defined as G'=G"

In figure 5.13 we show γ_y the crossover strain as a function of volume fraction and at different frequencies, for all particles used. For P2_41k at 0.1 rad/s γ_y exhibits a non-monotonic behavior similar to that reported for hard spheres (Koumakis, Schofield et al. 2008). Such a non-monotonic behavior has been predicted by activated hopping models in HS (Kobelev and Schweizer 2005). An explanation behind this non-monotonic behavior is the following: well inside the glass as the volume fraction increased the free volume per particle in the cage is decreased and diminishes at random close packing where the particles are in contact. Hence in

149

this regime increasing the volume fraction progressively allows for less cage distortion before particles collide with each other causing irreversible rearrangements, cage breaking and yielding (Koumakis, Pamvouxoglou et al. 2012). Similar behavior can be attributed to our system, since the hairy part is penetrable only in the outer layer, due to the high grafting density, with the chains attached on the core to be extremely stretched close to the core (Ohno, Morinaga et al. 2006). For the higher frequencies 1 and 10 rad/s, the yield strain decreases with increasing volume fraction with the particles colliding each other causing again cage braking and yielding.

Similar behavior we observe for P2_126k at 0.1 rad/s where the yield strain decreases from 14.5% at c/c*=1.01 to 9.6 % at c/c*=1.3. The difference with P2_126k is that the effective density of the outer blob is 2.5 times lower compared to P2_41k.   For higher frequency (1 rad/s) the yield strain has a non-monotonic behavior, decreasing as we increase the volume fraction up to 1.15 while beyond this point it shows a further increase. The first decrease could indicate a similar mechanism with 0.1 rad/s. The subsequent increase of the yield strain reflects the soft nature of interparticle potential and the elasticity of the polymeric outer shell, behavior that is reported in emulsions (Mason, Bibette et al. 1996) and star-like micelles or core-shell microgels (Koumakis, Pamvouxoglou et al. 2012). Same trend is also detected at 10 rad/s with yield strain to increase, for the same reasons.

For the larger particle (P2_402k) the yield strain is found to be independent of volume fraction and is ~9% at 0.1 rad/s and ~7% for 1 and 10 rad/s. This is probably due to very long grafted chains creating a fuzzy shell that allows strong interpenetration; note that the concentration where glassy behavior is found here (c/c*>1.3) is higher than in the previous harder particle.
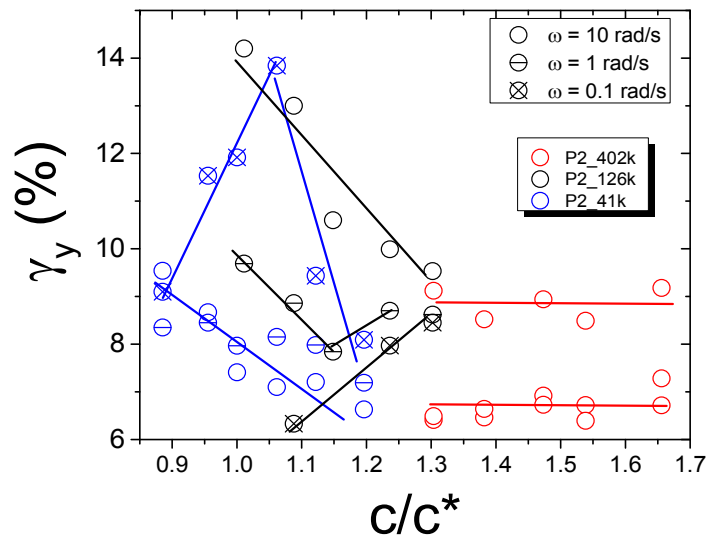
Figure 5.13: Crossover yield strain versus effective volume fraction c/c*, at different frequencies, taken from dynamic frequency sweeps (figure 5-7) for all systems studied.

Lissajous figures

A common plot in LAOS experiments is the stress as a function of strain in a Lissajous type figure. The shape of an oscillatory cycle in a stress-strain curve can provide information for the yielding and flow behavior within the period. In the linear regime, stress and strain have sinusoidal shape with the same frequency and the Lissajous figure is an ellipse. The aspect ratio of this ellipse reflects the ratio G'/G", the higher the asymmetry the higher the elastic component. Any deviation from the elliptical shape is an evidence of the existence of higher harmonic contribution in the stress in the nonlinear regime.
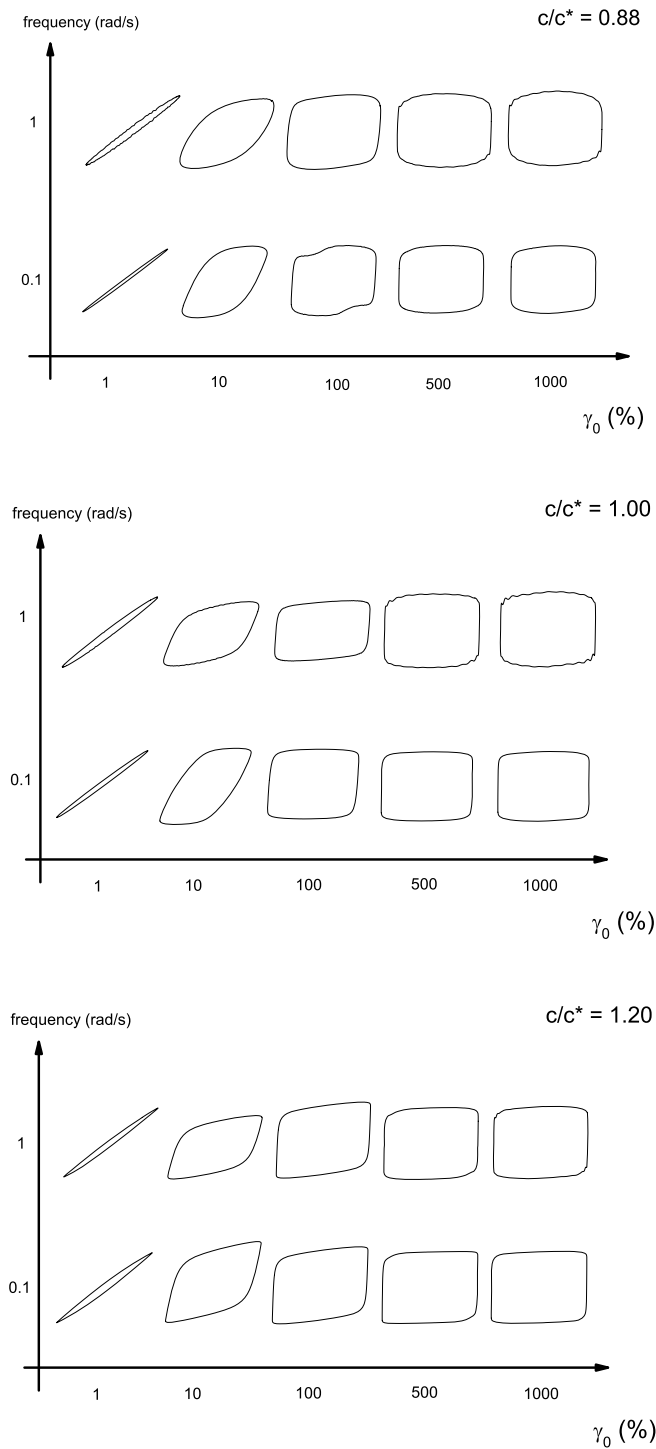
Figure 5.14: Pipkin type diagram of Lissajous figures for different stress vs strain and two different frequencies, 0.1 rad/s (Pe_0 = 0.00192) and 1 rad/s (Pe_0 = 0.0192) for three volume fractions of P2_41k: (a) c/c*0.88 , (b) c/c*=1 and (c) c/c*=1.2

152

Figure 5.14 depicts a Pipkin type diagram for P2_41k at different frequencies (0.1 and 1 rad/s) and strain amplitudes (1,10,100,500 and 1000%) for three volume fractions (c/c* 0.88,1.00 and 1.20) measured. At low strain amplitude (for example 1%) all samples respond linearly; the shape of the Lissajous curve is ellipse and the system is elastic. As we increase the strain close to the yield strain (γ_0=10%) obtained from DSS measurements, there is a transition from an elliptical shape to trapezoid which becomes more squared as strain amplitude increases. The nonlinear behavior is more pronounced at high strains (500% and 100%) where the Lissajous figures have sharp edges. In these figures we can distinguish two different regions: the first where the stress increases almost linearly with strain and the second where stress is nearly independent of the strain. The phenomenology of this behavior can be the following: at maximum strain the direction of the deformation starts to change and the stress increases linearly with strain, indicating an elastic response. At the point where strain exceeds a certain value, which corresponds to the yield point, the system undergoes plastic flow, with the stress almost independent of strain and thus the strain rate. This shape represents a typical elasto-plastic response at low Pe, as that seen in hard (Koumakis, Laurati et al. 2012) and soft spheres (Koumakis, Pamvouxoglou et al. 2012)

For the c/c*=0.88 , sample frequency of 0.1 rad/s and strain of 100% the Lissajous figure exhibits a characteristic shape of a rectangular with a double concave distortion after strain reversal suggested of a reduced stress at this regime within the period. This has been seen at high Pe in HS glasses and is attributed to stress reduction (due to fewer particle collisions) (Koumakis, Brady et al. 2013)

The Lissajous figures for the intermediate particle (P2_126k) show different behavior (figure 5.15). Here we show Pipkin diagram at two different volume fractions c/c*=1.30 and 1.09 at a constant frequency of 10 rad/s. At 10% strain in both volume fraction we have elliptical shape Lissajous curves with higher asymmetry in the case of c/c*=1.09. For the smaller volume fraction (c/c*=1.09) and strain of 50% we observe a clear stress overshoot, similar to what has been reported to soft systems (Carrier and Petekidis 2009, Renou, Stellbrink et al. 2010) as well as other systems (Ewoldt, Winter et al. 2010). This stress overshoot is shrinking in extend as

153

strain is increased at γ_0=500% and as shown is transformed to ripples detected passed the maximum strain. The shape of the Lissajous figure at 1000% strain is nearly circular with the viscous respond dominating. The shape of the curves at c/c*=1.30 at 500 and 100% have an elastic to plastic response with a small overshoot after strain reversal. The viscous Lissajous figures (stress versus shear rate) of the same samples can be also seen (5.15 bottom). What is more interesting is the self-intersection of the stress signal at 1.09 c/c* for 5 and 50 s^{-1} (50 and 500 % strain amplitude). The appearance of this kind of secondary loops has recently been explained as coming from a strong elastic non-linearity leading to an apparent negative local elastic modulus around zero strain (Ewoldt, Winter et al. 2010). More generally, this reflects the difference in the behaviour upon increasing the rate as zero strain is approached compared to that of decreasing rate in the quadrant following zero strain.
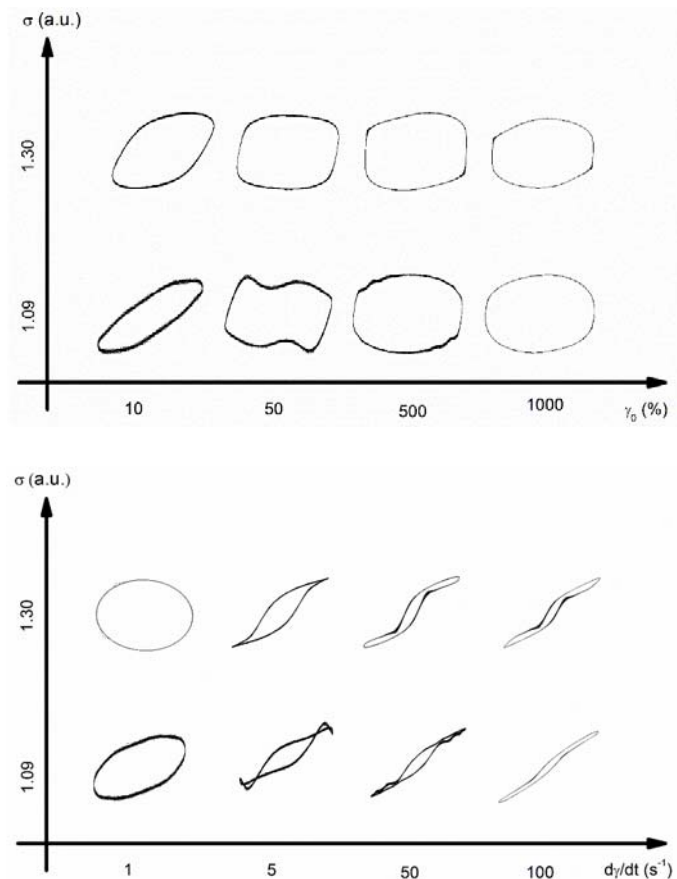
Figure 5.15 top: Pipkin type diagram stress vs strain **(top)** and stress vs rate **(bottom)**, at frequency 10 rad/s (Pe$_0$ = 1.74) and two volume fractions for P2_126k.

In figure 5.16 we show the Lissajous figures for P2_402k, the larger and softer particle, at different frequencies (0.1 and 1 rad/s), for various strain amplitudes and volume fractions (c/c* of 1.16, 1.38 and 1.66). The shape of the curves are similar with the smaller particles (P2_41k). At lower strains we have viscous elastic response with the curve being an ellipse.
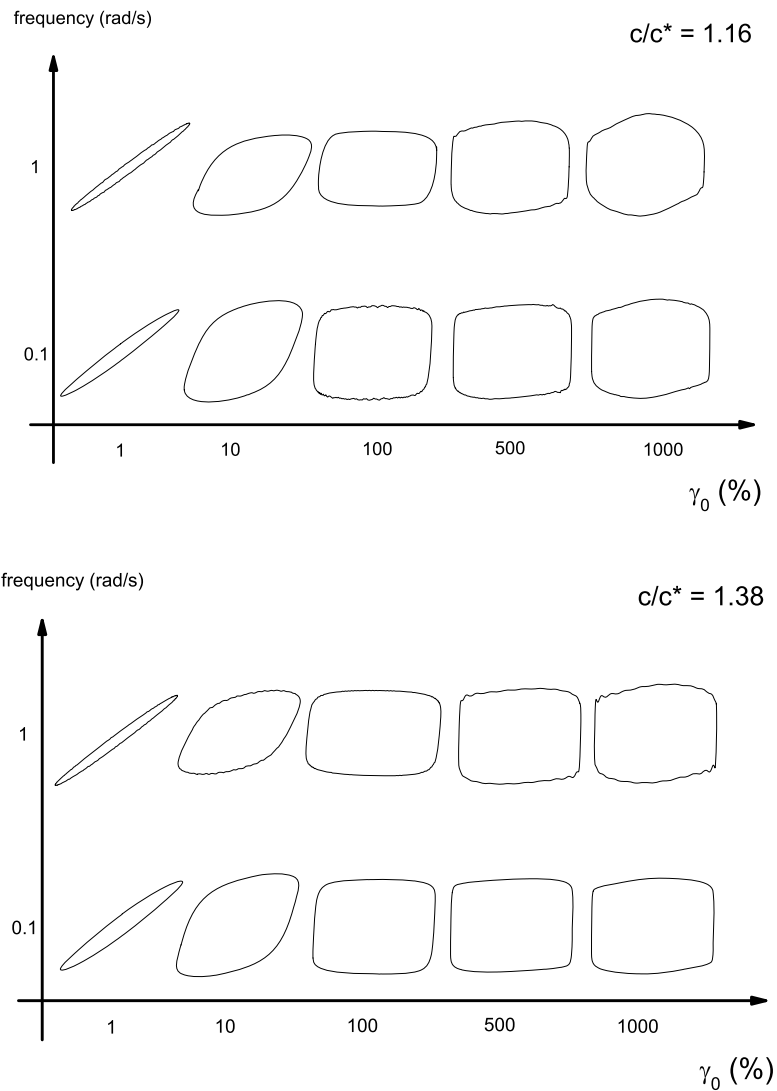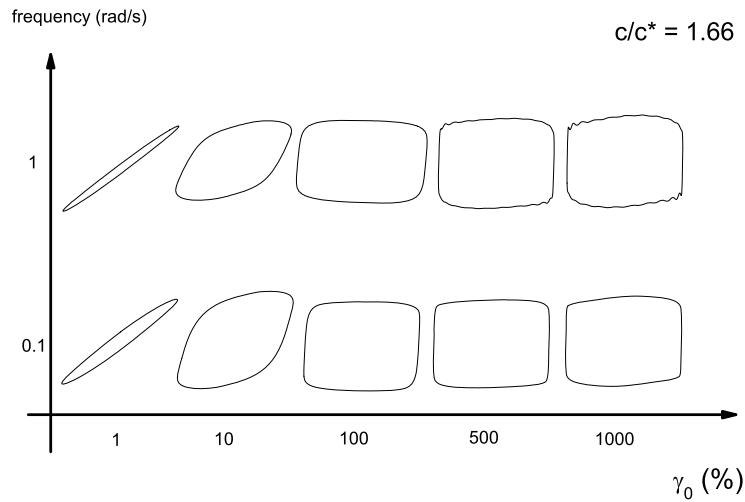
Figure 5.16: Pipkin type diagram (stress vs strain) showing strains of 1%, 10%, 100%, 500% and 1000% at different frequencies of 0.1 rad/s ($Pe_0 = 0.06364$) and 1 rad/s ($Pe_0 = 0.6364$) and volume fractions for P2_402k.

As we increase the strain at all volume fractions and frequencies the shape becomes more trapezoid and at the highest strain amplitude and frequencies the curves exhibit the double concave feature with decreased stress after strain reversal that has been mentioned above (figure 5.15). At c/c*=1.16 at 100% strain and ω= 0.1 rad/s we observe an ellipsoid with a double concave distortion caused by reduced stress after strain reversal. This stress reduction is more pronounced at the highest frequency ω=1 rad/s in agreement with the HS glass findings (Koumakis, Laurati et al. 2012) for the same reason discussed above. The same effect of the stress reduction is observed at the lowest volume fraction (c/c*=0.88) and 1000% strain in P2_41k.

5.5 - Steady measurements

5.5.1 – Flow curves

We now discuss the aspects of the nonlinear steady shear measurements in the three systems. In figure 5.17 we show flow curves (steady rate sweep tests), for the P2_41k in the solvent mixture. The experiments performed from high to low shear rates. The sample exhibits yield stress plateau at low rates and a sublinear increase of the slope at high rates.

The data can be well described by a Hershel-Bulkley model, $\sigma = \sigma_y + \eta(d\gamma/dt)^v$ with σ_y the yield stress determined at the low shear rate plateau and v an exponent defining the rate dependence of the stress at high rates. The dependence of the yield stress on the volume fraction will be discussed in figure 5.20. The slope of the exponent v varies from 0.4 to 0.48 with decreasing the volume fraction.

Figure 5.17 left: Flow curves showing the normalized stress response at various effective volume fractions. Lines represent the Hershel-Buckley fit to extract the slope at infinite rates n and the yield stress plateau σ_y at lower Pe, for P2_41k. **right:** Universal plot of the scaled shear stress as a function of the scaled shear rate at different c/c*. Line represents the best fit from Hershel-Buckley model.

In most of the experiments a rate independent high shear viscosity, is not reached. This slope close to 0.5 has been associated with the flow of soft deformable particles (Cloitre, Borrega et al. 2003, Meeker, Bonnecaze et al. 2004). By plotting the stress scaled by the yield, σ_y, and the rate by a characteristic rate we can attempt to superimpose all data in a universal curve.

Figure 5.17b shows the scaled shear stress as a function of the scaled shear rate. The shear rate was multiplied by a factor A in order to superimpose the data. Then they were fitted by a general Hershel-Buckley fit, $\sigma/\sigma_Y = 1 + A(d\gamma/dt)^\nu$, in order to calculate A and v. For the scaling we used as reference the highest volume fraction ($c/c^*=1.2$). As we decrease c/c^* A increases up to A=180. Bonnecaze et al. showed that in microgel suspensions $A \approx \eta_s/G_o$ where η_s is the solvent viscosity and G_o the shear modulus extracted from simulations. Since solvent viscosity is constant, we can assume that $A \sim G_o^{-1}$. The slope at high rates is constant and around 0.5, similar to what has been observed for similar soft systems (Miller and Kauffman 1989, Mours and Winter 1996, Tanaka and Young 2006).

Figure 5.18 left: Flow curves showing the normalized stress response at various effective volume fractions. Lines represent the Hershel-Buckley fit to extract the slope at infinite rates n and the yield stress plateau σ_y at lower Pe, for P2_126k **right:** Universal plot of the scaled shear stress as a function of the scaled shear rate at different c/c^*. Line represents the best fit from Hershel-Buckley model.

For P2_126k in Veratrole we observe a qualitatively similar behavior (figure 5.18). The data are fitted with Hershel-Bulkley model to extract the yield stress plateau at low shear rates. The slope of the exponent ν is higher compared to P2_41k and is from 0.76 to 0.78, close to unity. The scaled yield stress versus the scaled shear rate is shown in figure 5.18b. Here the Hershel-Buckley model fail to fit our experimental data. A discrepancy at intermediate shear is observed and the slope at high shear rates regime is around 0.7. A values has less volume fraction dependence compared to smaller (harder) particles.

For the bigger particles in the solvent mixture at high volume fraction a yield stress plateau is observed. Below $c/c^* = 1.38$ Hershel-Bulkley fit failed to fit the data at low rates. In order to extract the yield stress σ_y we used the value at the lowest shear rate measured. The exponent at high shear rates ν is in a range from 0.5 to 0.7 increasing with decreasing volume fraction. This trend is similar to hard spheres where the exponent is always higher than 0.5 and decreases with increasing φ (Koumakis, Schofield et al. 2008, Koumakis, Pamvouxoglou et al. 2012). The scaled shear stress is also plotted at different volume fraction in a universal plot. A values are close to values calculated for P2_126k.
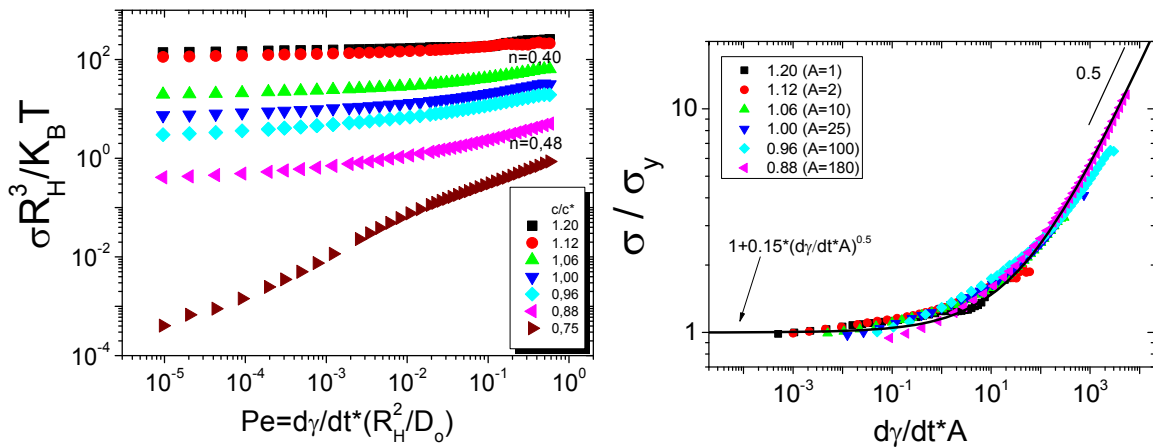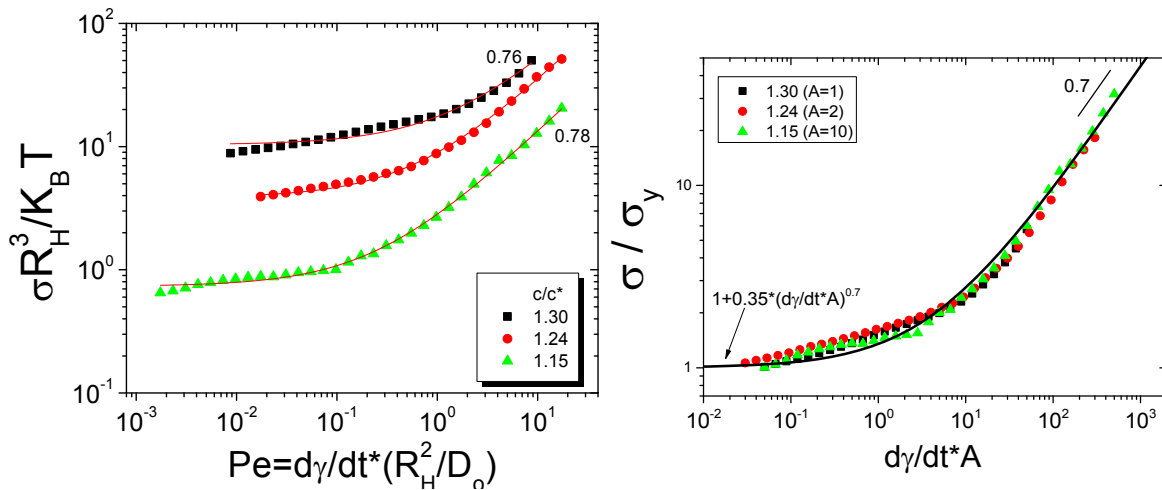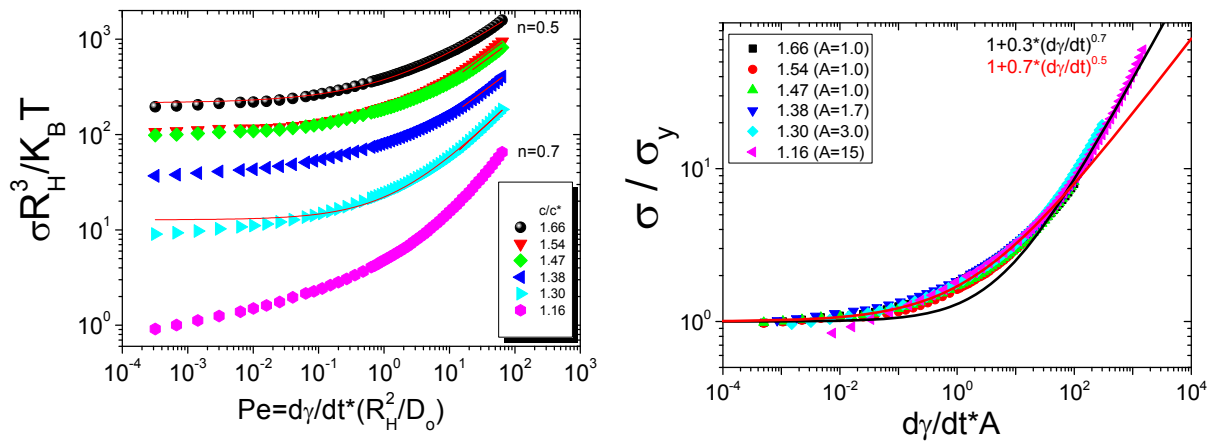

Figure 5.19 left: Flow curves showing the normalized stress response at various effective volume fractions. Lines represent the Hershel-Buckley fit to extract the slope at infinite rates n and the yield stress plateau σ_y at lower Pe, for P2_41k. Whenever the model fail to fit our experimental data we used for σ_y the value at the lowest Pe. **right:** Universal plot of the scaled shear stress as a function of the scaled shear rate at different c/c^*. Line represents the best fit from Hershel-Buckley model.

159

Similarly to the intermediate softness particles (P2_126k) the Hershel-Buckley model fails to fit our experimental data. For comparison we have plotted Hershel-Buckley fit having two different exponents 0.7 (black line) and 0.5 (red line) respectively. Both of the fits fail to superimpose the experimental data.

A summary of the yield stress at different volume fractions and particle sizes is presented in figure 5.20. The slope of the yield stress as a function of volume fraction is the same for all systems. There is a change in the slope of the yield stress at higher c/c* especially for the bigger particle (P2_402k) denoting the softer character of the particle. What is interesting is that P2_126k and P2_402k seem to have the same yield stress values at the same volume fraction range.
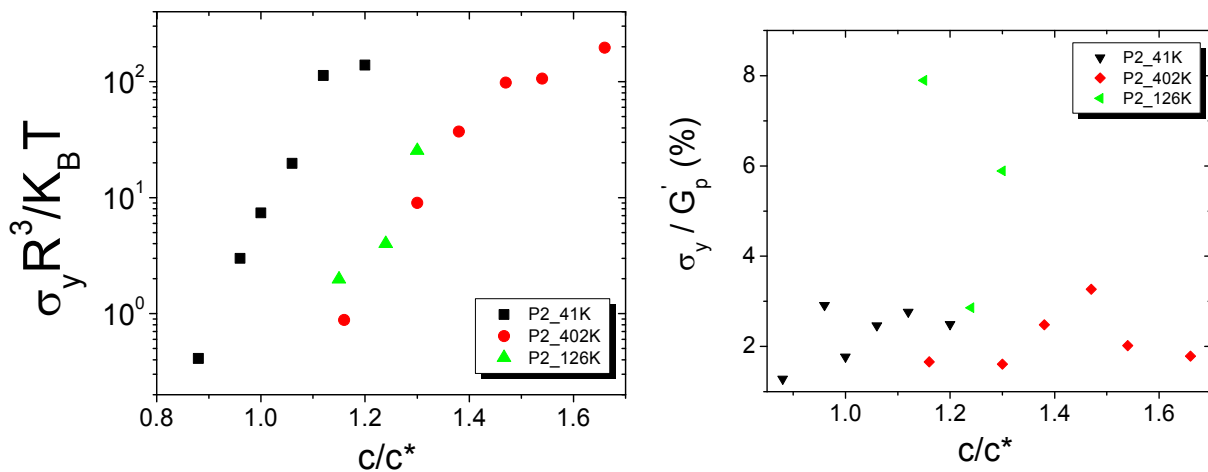
Figure 5.20 left: Scaled yield stress versus volume fraction for the three systems studied **right:** critical stain values extracted from yield stress and G'_p from plateau modulus

The common characteristic of these particles is the same grafting density and that both have Concentrated Polymer Brush (CPB) to Semi-Dilute Polymer Brush (SDPB) transition for the density profile of the polymer that is attached on the core. The small discrepancy for the slope of the yield stress at the highest volume fraction may be due to the partial squeeze/interpenetration, since at c/c*=1.3 we reach the maximum close packing fraction through high speed centrifugation at 8475g, with g being the gravity constant. Figure 5.20b

shows yield strain extracted from flow curves as: $\gamma_y = \sigma_y / G_p^l$, where G_p^l is the plateau modulus at Pe=1. In all cases the critical strain extracted from steady shear measurements is lower compared to yield strain from dynamic measurements.

5.5.2 – Transient Tests

<u>Start-up shear and relaxation after switch-off</u>

Transient response of complex yield stress materials involves complicated microscopic mechanisms when a sample is subjected to a start-up experiment where a constant shear rate is applied from rest and the system is taken from the solid to a flow (liquid-like) state. During such stress we monitor the stress response until steady state is reached. A typical start-up test consist of a regime where the stress σ is increasing almost linearly with time, reaches a maximum value denoted σ$_{peak}$ and then decreases towards it steady-state value. Such stress overshoot has been reported experimentally in a wide range of soft and other materials such as polymers (Boukany and Wang 2009), microgels (Divoux, Barentin et al. 2011, Koumakis, Pamvouxoglou et al. 2012) and colloid suspensions (Derec, Ducouret et al. 2003, Koumakis, Laurati et al. 2012). Generally the overshoot is less pronounced at low shear rates as Brownian motion relaxes any structural changes back to equilibrium not allowing large structural deformation and stress storing. When more complicated mechanisms are involved during start-up experiments, such as those of shell deformation or chains interpenetration and disentanglement, the HS picture might change. The stress relaxation after cessation of the step rate test, keeping constant the rate $\dot{\gamma}$ at zero shows the percentage of the elastic response prior to viscous component.

Figure 5.21 shows step rates and stress relaxation for the smaller and harder particle (P2_41k) at different rates and volume fractions after the initial stress increase. In contrast to the simpler start-up response of HS or other soft particles (Koumakis, Laurati et al. 2012, Koumakis,

Pamvouxoglou et al. 2012) here we observe an oscillating increase of stress with strain in all volume fractions and shear rates. The system seem to reach pseudo steady state only at the highest rate ($\dot{\gamma}$=1s^{-1}) and at 10,000 % strain. Divoux and co-workers, using carbopol particle suspensions, (Divoux, Tamarii et al. 2010) reported that fluidization can take more than 10^4 strain units to reach steady state at low shear rates and they attributed such low transition to steady state due to transient shear banding. Moreover in hard sphere glasses Ballesta et al. (Besseling, Isa et al. 2010, Ballesta, Petekidis et al. 2012) detected the appearance of shear banding at low rates when wall slip is eliminated. This might be a possible explanation, since we used serrated plates during the experiments to eliminate strong wall slip that is taking place with smoothed geometries. As we decrease the volume fraction the multiple stress overshoot curves on the start-up experiments are progressively weakening and at c/c*=0.88 we observe mainly a single overshoot with the plateau after the overshoot reaching higher stress values, especially at higher rates. The trend of the stress peaks is always the same with the stress to be higher as we increase the rate.

Figure 5.21: left) Step rate tests at different rates and six volume fractions (from c/c* 1.2-0.88) for P2_41k
right) Normalized stress relaxation curves after start-up tests. *Figure 5.21 continues on the next page*
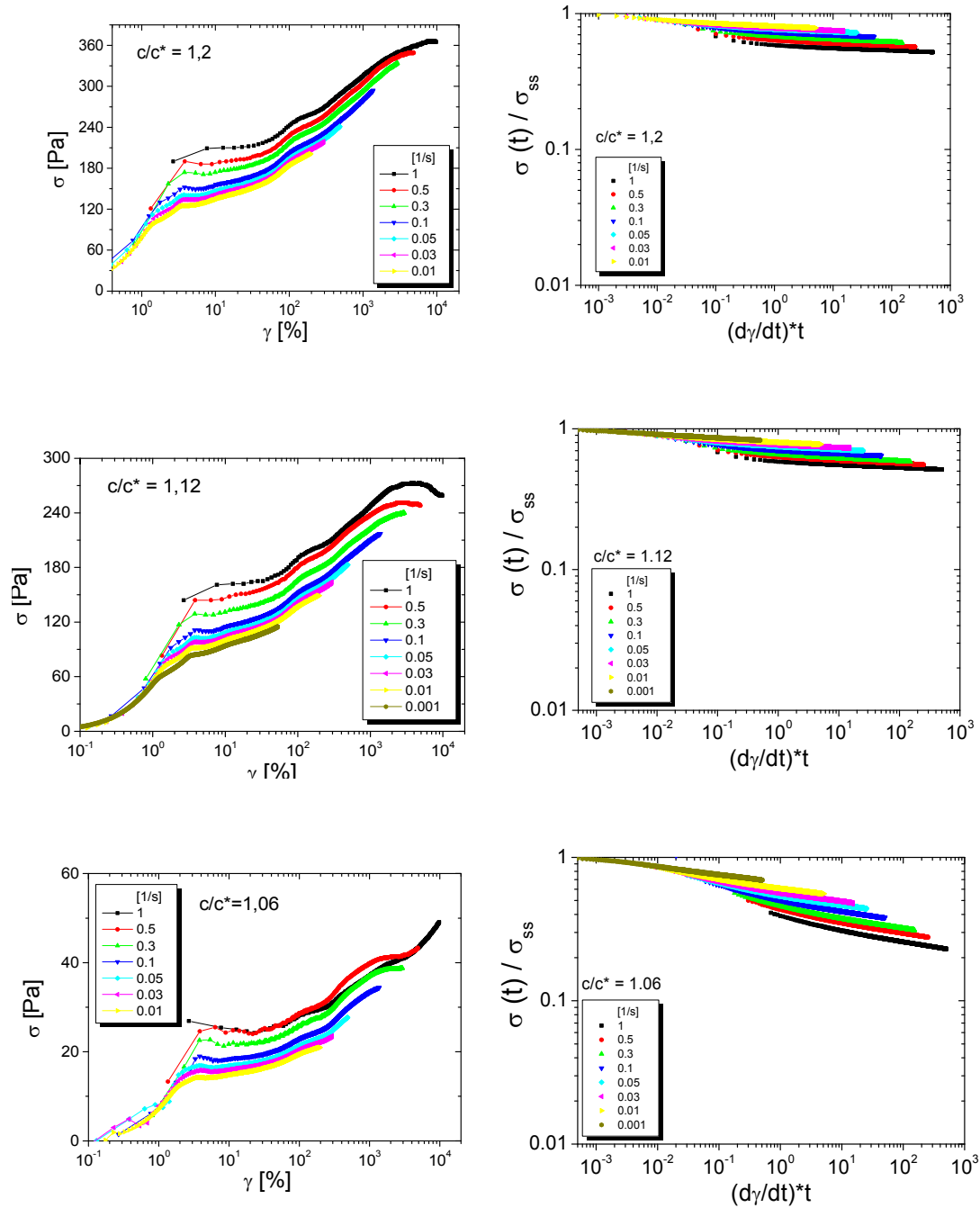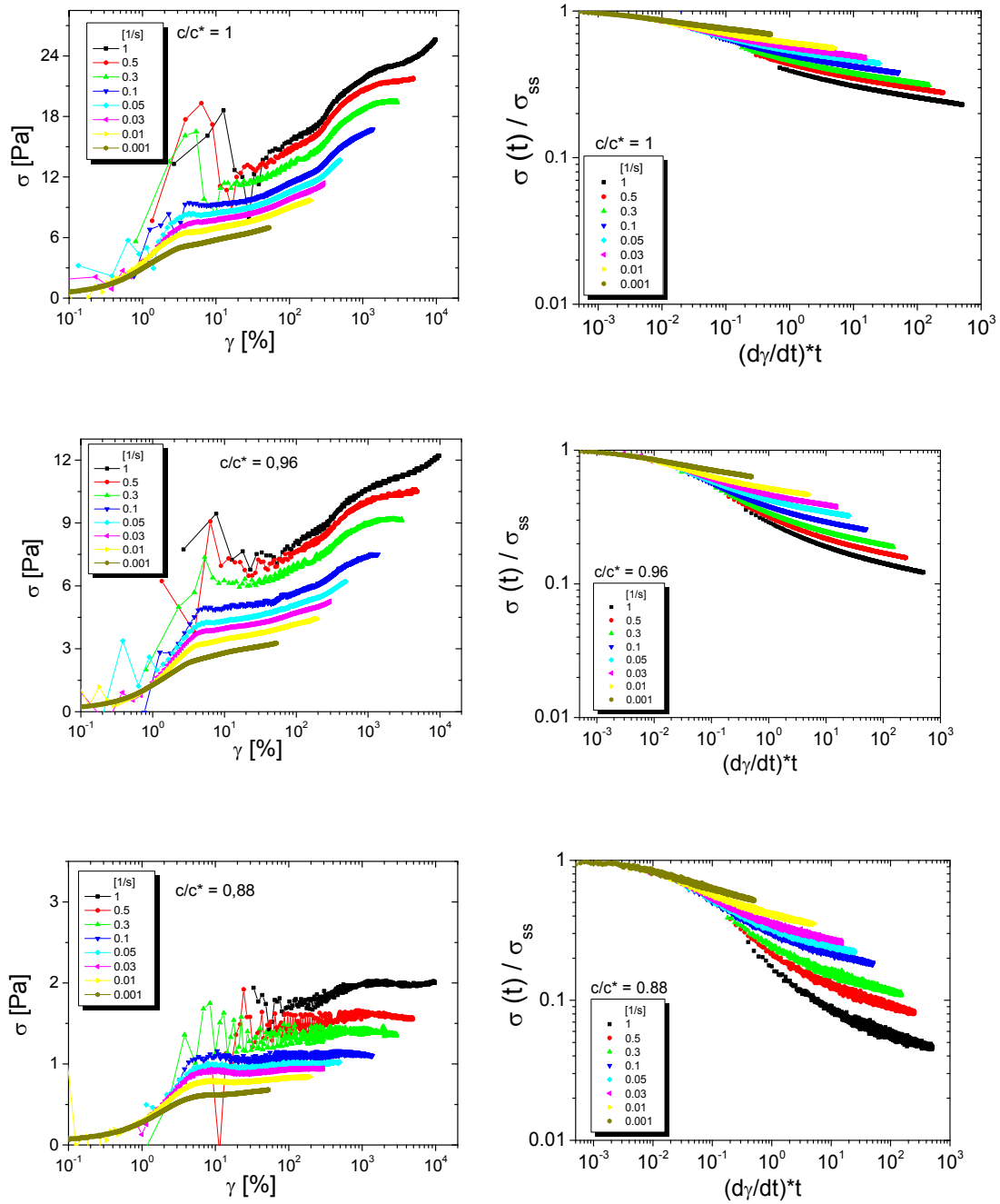
Figure 5.21: left) Step rate tests at different rates and six volume fractions (from c/c* 1.2-0.88) for P2_41k **right)** Normalized stress relaxation curves after start-up tests.

For an ergodic sample that has a fluid-like behavior at low volume fractions, one would eventually expect the relaxation to become zero as SGR model predicts. For non-ergodic systems, it is not clear whether the stresses will relax completely. Figure 5.21 on the right shows the relaxation curves at different rates and volume fractions, normalized by the stress just before the cessation of shear. We have used $\dot{\gamma}t$ in order to be equivalent to strain. In all cases we clearly see a speedup of relaxation with increasing shear rate, with the highest rates to show stronger initial decrease of the stress. With the decrease of c/c* the stress seem to relax faster and eventually fully relaxing to zero at the lowest volume fraction (c/c*=0.88). Therefore the residual stresses dropped one order of magnitude with decreasing c/c*. At high volume fractions the system manages to build in stresses only partially by 40%, at very long times ($\dot{\gamma}t\sim10^{3}$), showing a strong jammed state, where the particles are squeezed and with significant chain interpenetration. At lower rates ($\dot{\gamma}\sim10^{-3}$) the system cannot relax the stresses induced from start-up experiments more than 15%. On the other hand at the lowest volume fraction (c/c*=0.88) the stresses remaining on the system is less than 4%. The particles have more space to move since we are closer to liquid-glass transition ($c/c^{*}{}_{g}\sim0.82$). In general, soft-glassy rheology (SGR) model (Sollich, Lequeux et al. 1997) predicts asymptotic power-law that imply the relaxation of stresses to zero. Recent work by Ballauff et al. (Ballauff, Brader et al. 2013) reports that in colloidal glasses of both hard and soft particles, residual stresses can be persistent even at large times after the cessation of flow. Such finding is described by Mode Coupling Theory of ideal glasses, although there the residual stresses are lasting forever.

Figure 5.22 on the right depicts the critical strain at the peak of the stress overshoot at different Peclet and volume fractions. At constant volume fraction the critical strain increases with increasing the shear rate (Peclet), since the cage is deforming more at larger rates before it breaks, similar to hard spheres (Koumakis, Laurati et al. 2012). The maximum critical strain occurs at the lowest volume fractions and decreases as we increase c/c*. At Pe~10^{-3} we observe the critical strain to increase by decreasing the effective volume fraction, with values lower to the γ_y observed from DSS measurements where the yield strain decreases with increasing volume fraction.
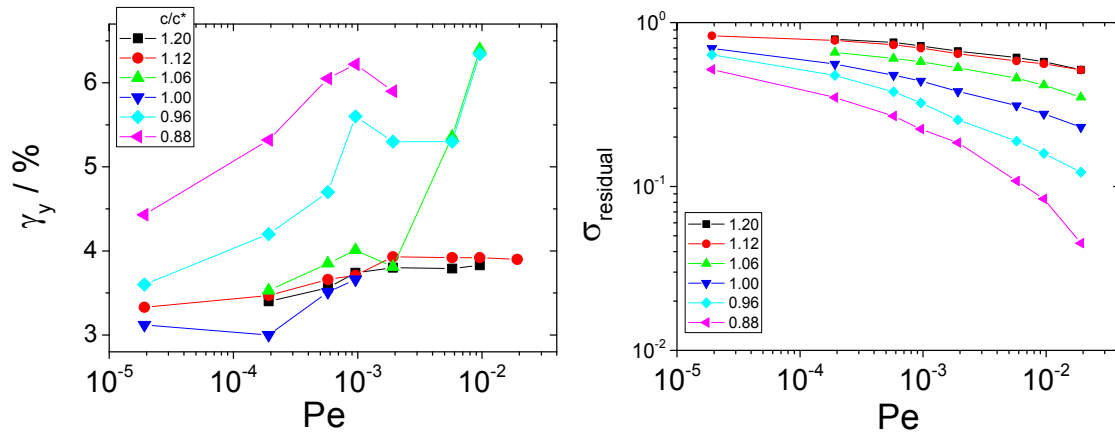
Figure 5.22 left: Critical strain as a function of Peclet and volume fraction for P2_41k **right:** residual stresses at different Pe and volume fractions.

Figure 5.22 on the left shows the values of the residual stress, $\sigma_{residual}$, at different Pe and volume fractions. The $\sigma_{residual}$ was calculated from the last point of the normalized stress relaxation curves after start-up tests. For c/c* higher than 0.88 $\sigma_{residual}$ decreases linearly with increasing Pe similar to hard spheres (Ballauff, Brader et al. 2013). At c/c*=0.88 the $\sigma_{residual}$ decreases significantly faster showing a two-step decay. The highest volume fractions have identical residual stresses at all Pe range, due to the fact that particles are closer to the maximum packing ($c/c^*_{RCP} \sim 1.2$) and therefore strongly interpenetrable.

For P2_126k the start-up experiments show different behavior (figure 5.23). In most of the cases we observe the linear regime, a stress overshoot and a plateau, which at high rates its value is higher from stress at peak. At low rates the stress overshoot is not symmetric and a shoulder appears after the stress peak. This shoulder is present in soft colloidal systems like star polymers and star-like micelles, where the particles have to disentangle before yielding (Petekidis, Vlassopoulos et al. 2003, Petekidis, Vlassopoulos et al. 2004, Koumakis, Pamvouxoglou et al. 2012). For c/c*=1 at high rates the stress overshoot diminishes and the system reaches steady state after a second yield point which appears at 500% strain.
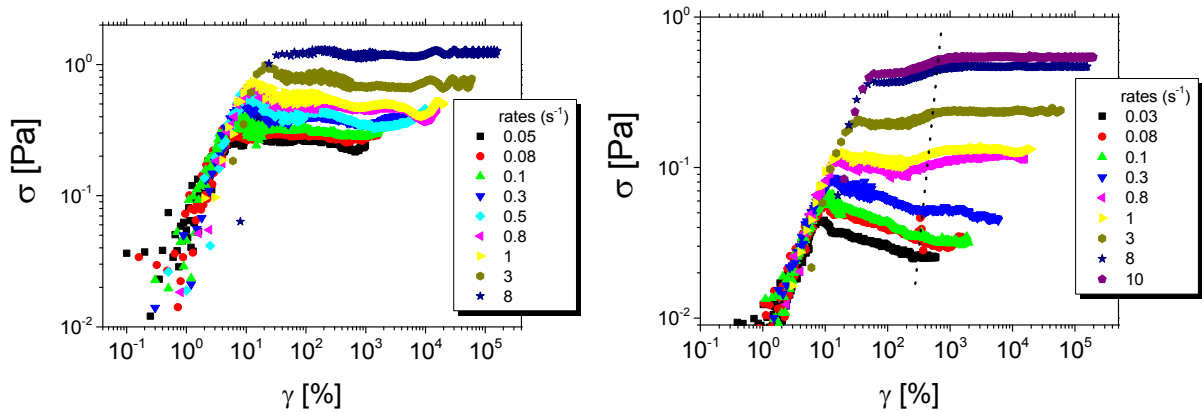
Figure 5.23: Step rate tests for different rates in two volume fractions (1.3 (left) and 1.01 (right)) for P2_126k.

In figure 5.24 on the left we show the yield strain, for the P2_126k, as a function of Pe and volume fraction. At constant volume fraction the critical strain increases as we increase Pe, indicating higher cage deformation at higher rates. The critical strain at the peak of the stress overshoot varies from 7% strain at low Pe (~0.03)up to 32% for the higher Pe (~10) at c/c*=1.01. This wide critical strain range should be related with structural distortion together with particle shape deformability. Note that again the critical strain observed from start-up experiments is higher compared to yield strain from oscillatory data which was about 8-14% strain.
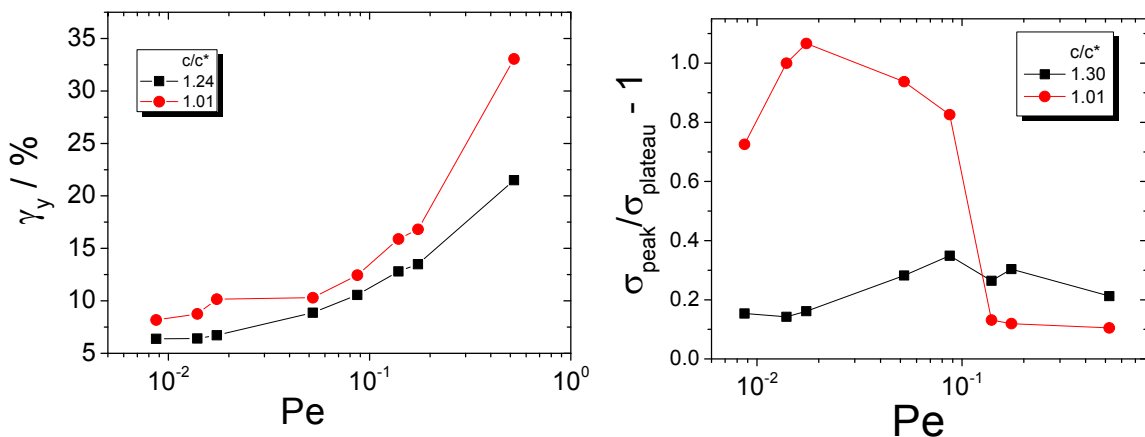
Figure 5.24 **left:** Yield strain as a function of Peclet and volume fraction for P2_126k **right:** Normalized amplitude of the step rate peak at different Peclet for c/c* 1.3 and 1.01

Figure 5.24 on the right shows the magnitude of the stress overshoot, $\sigma_{peak}/\sigma_{plateau}$ -1, where σ_{peak} is the stress at the peak and $\sigma_{plateau}$ the stress of the plateau after the stress overshoot. By plotting the strength of the stress overshoot as a function of the steady rate, we can probe the effect of Pe to the stress overshoot which is related to structural relaxations after shear induced cage distortion. At c/c*=1.30 there is weak Pe dependence. The cage is tight and the particles strongly interpenetrate with the system yielding upon small distortions. On the other hand at c/c*=1.01 a stronger overshoot is measured at intermediate Pe and non-monotonic trend is revealed: the strength of the overshoot first increases, reaching a maximum at Pe~ 0.03 and then decreases towards zero at higher Pe. Similar trend was observed recently in hard spheres by Koumakis et al. (Koumakis, Laurati et al. 2014). The decrease of the overshoot at high Pe is attributed to particle collision that become significant even long before the stress overshoot. In our case, an additional interplay between chain interpenetration and particle deformation due to soft and permeable character of the particles.

For the larger and softer particles (P2_402k) in figure 5.25, stress overshoot increases as we increase the rate, similar to other systems. The peak of the stress overshoot is not symmetric, with a shoulder appearing at strains beyond the critical strain at the peak, due to disentanglement of the grafted chains before the onset of steady state flow. However we also observe an additional peak around γ=100% at higher rates, possible attributed to transient cluster breaking, formed at high volume fractions due to chain interpenetration or phenomena such as shear instabilities and shear banding discussed above for the smaller particles . At higher volume fractions (c/c* 1.66-1.47) the stress keeps increasing beyond the peak, a behavior similar to P2_41k, but weaker in strength. At the lowest volume fractions (c/c* 1.38 and 1.30) the stress remains constant at higher strains, reaching a steady state.

Stress relaxation curves have the same behavior with the smaller particles (P2_41k), with the stress relaxing faster and to a lower plateau at higher rates. The stress relaxation reveals residual stresses that depend on the shear rate and c/c*. At the highest volume fraction, close to their maximum close packing, the system keeps a residual stress of around 80% which decreases

as we decrease c/c* down to 10%, having similar trend with the smaller and harder particle (P2_41k).
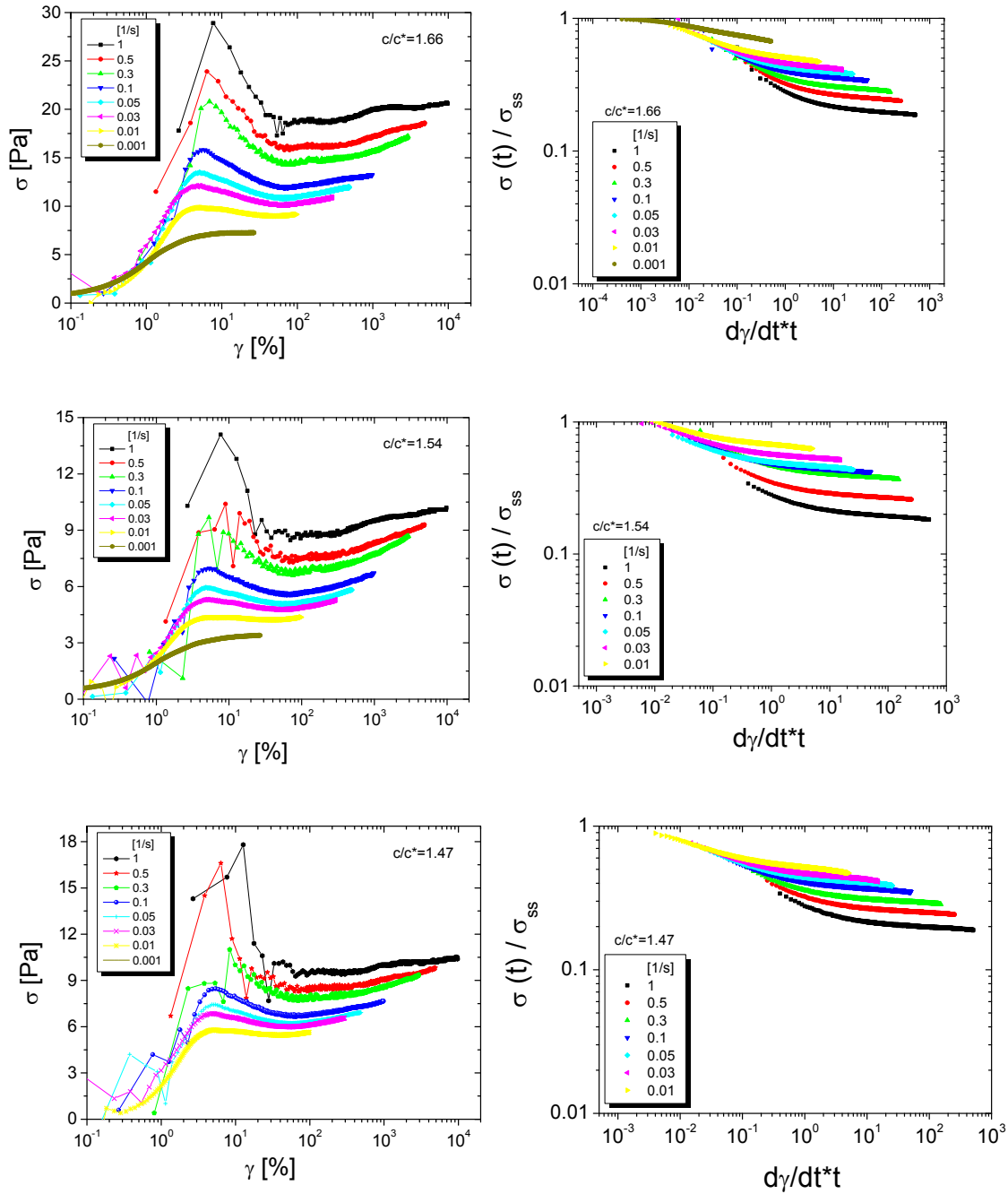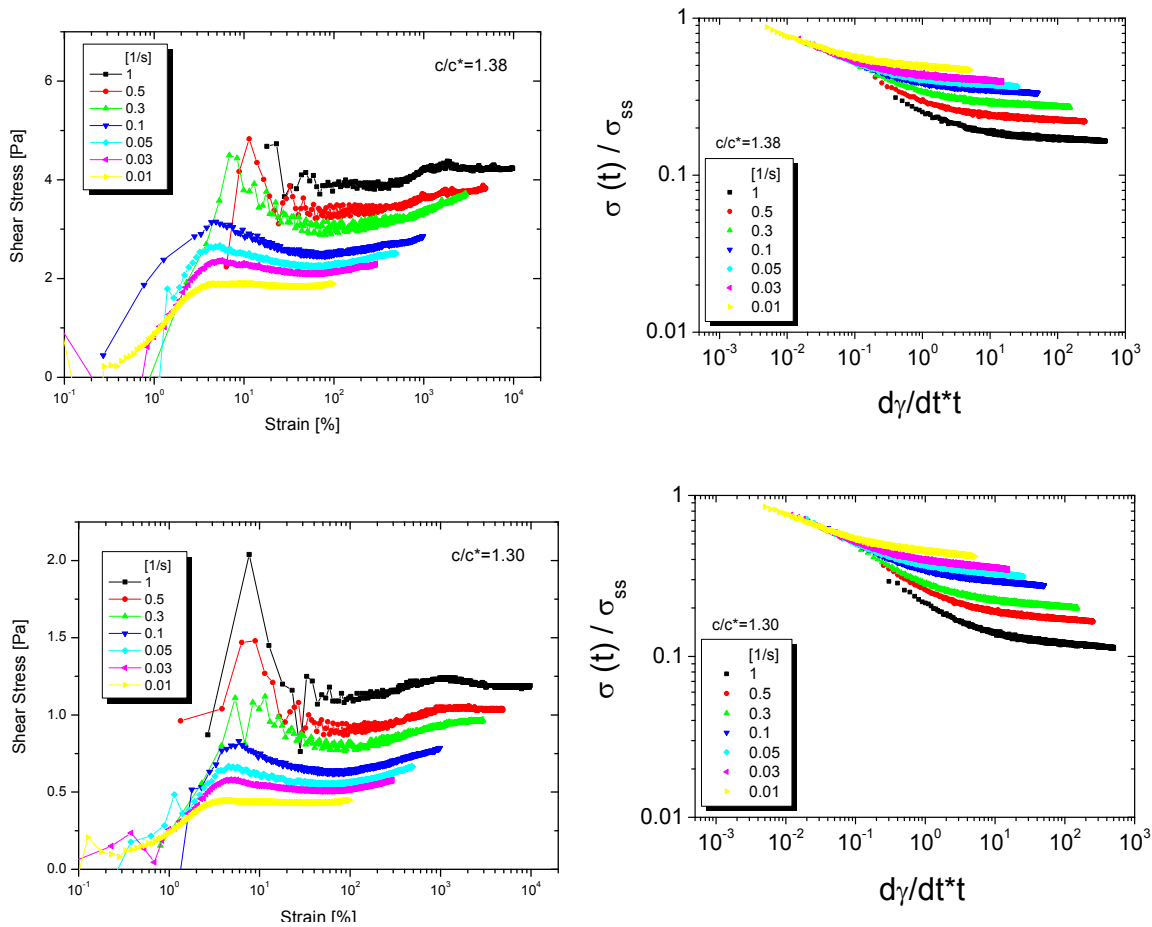
Figure 5.25: right) Step rate tests at different rates and five volume fractions (from c/c* 1.66-1.30) for P2_402k **right)** Normalized stress relaxation curves after start-up tests.

The critical strain values at the peak of the stress overshoot at different Peclet and volume fractions are shown in figure 5.26. The values γ_c range from 4 to 8 %. At constant volume fraction, critical strain increases as we increase Peclet, for the same reason discussed previously. For intermediate and low Peclet, γ_c is c/c* independent, similar to what has been reported for star-like micelles (Koumakis, Pamvouxoglou et al. 2012).

The strength of the stress overshoot in P2_402k is shown in figure 5.27. The stress overshoot increases with increasing the shear rate (Pe), reaching $\sigma_{peak}/\sigma_{plateau}-1 = 0.6$ (60%), but there is no concentration dependence due to strong interpenetration at these high volume

fractions (c/c* > 1.3). The strength of the stress overshoot is a combined result of shell deformation and the structural distortion of the cage, in contrast to HS where the stress overshoot is mainly due to cage deformation and has only an entropic character. For this soft particles, residual stresses are decreasing linearly with Pe (in log-log plot), but there is no volume fraction dependence probably due to strong interpenetration, like in the case of smaller (harder) particles (P2_41k in figure 5.22) at the higher volume fractions.
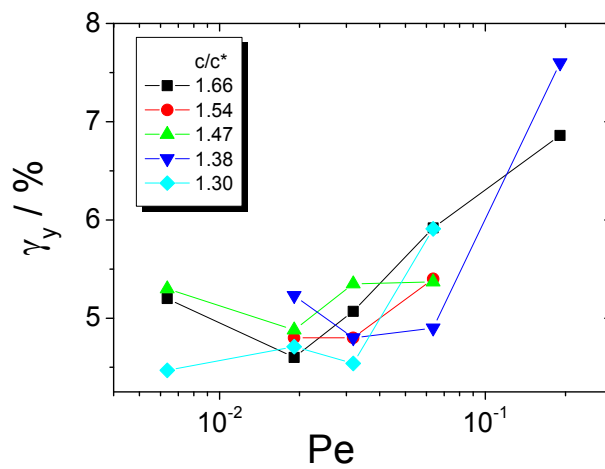
Figure 5.26: Yield strain as a function of Peclet and volume fraction for P2_402k
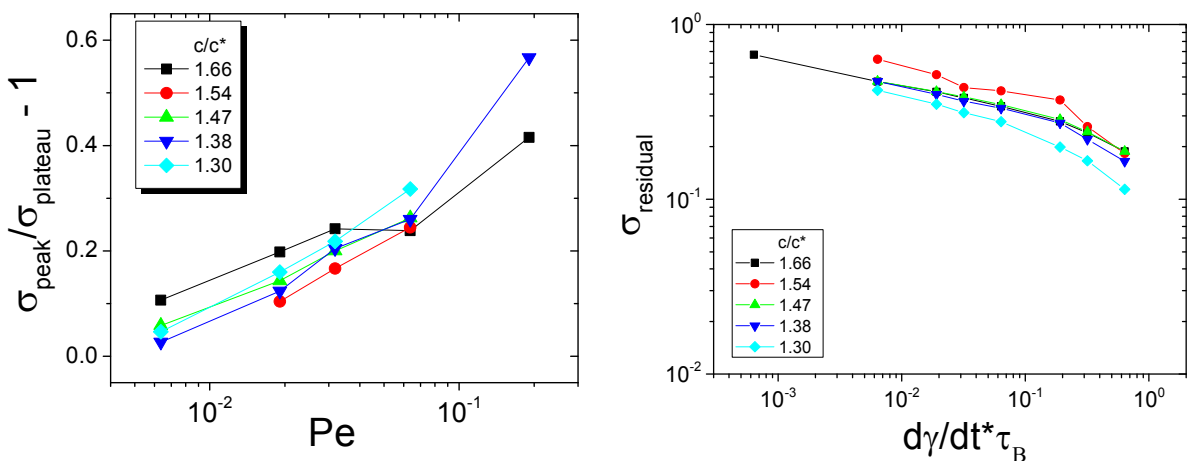
Figure 5.27 left: Critical strain as a function of Peclet and volume fraction for P2_41k **right:** residual stresses at different Pe and volume fractions.

5.6 – Conclusions

The effect of the particle's softness in glass regime of soft colloidal systems were studied in terms of rheological experiments in both linear and nonlinear regime. The effect of softness was elucidated by using three soft core-shell particles which have the same core size, surface density and only the molecular weight of the attached polymer chain is changed. The volume fraction was calculated simply by dividing the mass fraction with the overlap concentration $c^*(R_H)$ of its particle.

The dynamic frequency sweep test (DFS) show a typical glassy behavior with G'>G" at all frequencies and with G' being independent of frequency at all volume fractions and systems. From the plateau modulus, G' vs c/c* for the three systems was measured to calculate the interparticle potential, which is linked to particle softness. For the smaller and harder particle (P2_41k) G' was increasing linearly with c/c* with a slope of 22. At the highest volume fraction (c/c*=1.20) there is a slight decrease of the slope due to interpenetration. Similar behavior was observed for the intermediate particle (P2_126k) where G' increases with c/c* with a slope o 23, apart for the lower concentrations, where the slope is significantly lower, around 8. For the larger and softer particle (P2_402k) there is a clear two-step increase with slopes of 23 and 12 respectively. Interestingly the data of G' vs ɸ for P2_126k and 402k superimpose in the volume fraction range of 1.1 to 1.4 due to the softer outer shell that both particles have compared to the smaller and Harder P2_41k. A possible explanation to this superimpose is the appearance of the Concentrated to Semidilute Polymer brush (CPB to SDPB) transition, as it is predicted by Ohno et al. (Ohno, Morinaga et al. 2007). Apart from the interparticle potential, the transition from α to β relaxation was measured through the G" minimum. For P2_41k, two transitions where observed: one at c/c*~1 related to the glass transition where the particles are no longer able to move and a jamming transition at c/c*~1.1. Similar behavior was observed also for P2_126k, with a glass transition at c/c*=1.3, significantly higher from 41k due to softer particle character. For the larger and softer particle (P2_402k) t_{min} is constant and then speeds-up as we

172

continue increase c/c*. The constant t_{min} with c/c* is related to cancelation of effects from particles' shrinkage and increased confinement.

From dynamic strain sweep experiments, one can measure the yield strain, γ_y, the strain in which above the sample shows a viscoelastic liquid-like behavior, although not necessarily that of a Newtonian fluid. For the smaller and harder particle at 0.1 rad/s, γ_y shows non-monotonic behavior with c/c* due to decreasing of the free volume per particle, similar to what has been detected for hard spheres. At higher frequencies γ_y decreases with increasing c/c* due to colliding and cage breaking. For the intermediate particle, P2_126k, the behavior is similar with γ_y to decrease with c/c* for the same reason discussed above. The larger and softer particle has γ_y independent of c/c* and frequency due to strong interpenetration they exhibit at this high volume fractions (c/c* > 1.3). Through Lissajous figures we measure the response of the stress and strain within a period. This allows us to quantify the effect of the nonlinearities especially beyond the yield point. Lissajous figures for P2_41k have the same behavior with hard spheres with the systems to exhibit an elastic to plastic response as we increase the strain. By increasing the softness moving to P2_126k, Lissajous figures show different behavior. Beyond the elastic response, a clear stress overshoot is revealed, indicative of soft systems. The Lissajous for the larger particles (P2_402k) at the highest strain amplitudes exhibit a characteristic double concave shape with a decreased stress after strain reversal. When the system is sheared in one direction becomes highly anisotropic, allows flow with less stress when the shear is reversed to to fewer particle collisions.

In steady measurements and especially flow curves we discussed the effect of steady shear in the three systems. In all cases a characteristic yield stress plateau was revealed, indicative of the systems in the glass regime. We used a Hershel-Bulkley model to fit our data and extract the yield stress plateau value σ_y and the exponent v at high rates. By using the model proposed by Cloitre et al. (Seth, Mohan et al. 2011) we attempted to superimpose our data in a universal curve. For P2_41k all data superimposed quite well in a master curve with the slope at high rates being 0.5, similar to what has been predicted for soft systems. By increasing the softness moving to P2_126k and P2_402k, the model failed to superimpose the data, with the

slope at high rates to be significantly higher and around 0.7. The normalized yield stress is increasing with increasing c/c^* for all systems and for P2_126k and 402k, data superimpose evidence that the transition from CPB to SDPB might play a role.

In transient tests, start-up experiments together with stress relaxation tests were performed. For the smaller and harder particle (P2_41k) start-up tests show an oscillating increase of the stress in all volume fractions and shear rates. Possible explanation is the appearance of transient shear banding due to elimination of wall slip. The critical strain extracted from the stress at the peak shows Pe and c/c^* dependence similar to hard spheres. The residual stress $\sigma_{residual}$ measured from the stress relaxation tests performed after start-up, show an almost linear decrease with Pe and a decrease of its values with decreasing c/c^*. The softer character of P2_126k was revealed from the lack of volume fraction dependence of the critical strain as a function of Pe, similar to observations in soft systems. In the case of the larger particle (P2_402k) both the critical yield strain and the amplitude of the stress overshoot show no volume fraction dependence. Additionally the residual stresses $\sigma_{residual}$ are also c/c^* independent due to the strong interpenetration they exhibit at this high volume fractions. This is similar with P2_41k at the two highest volume fractions where $\sigma_{residual}$ is c/c^* independent.

5.7 – References

Ballauff, M., J. M. Brader, S. U. Egelhaaf, M. Fuchs, J. Horbach, N. Koumakis, M. Krüger, M. Laurati, K. J. Mutch, G. Petekidis, M. Siebenbürger, T. Voigtmann and J. Zausch (2013). "Residual Stresses in Glasses." Physical Review Letters **110**(21): 215701.

Ballesta, P., G. Petekidis, L. Isa, W. C. K. Poon and R. Besseling (2012). "Wall slip and flow of concentrated hard-sphere colloidal suspensions." Journal of Rheology **56**(5): 1005-1037.

Besseling, R., L. Isa, P. Ballesta, G. Petekidis, M. E. Cates and W. C. K. Poon (2010). "Shear Banding and Flow-Concentration Coupling in Colloidal Glasses." Physical Review Letters **105**(26): 268301.

Boukany, P. E. and S.-Q. Wang (2009). "Exploring the transition from wall slip to bulk shearing banding in well-entangled DNA solutions." Soft Matter **5**(4): 780-789.

Brader, J. M., M. Siebenburger, M. Ballauff, K. Reinheimer, M. Wilhelm, S. J. Frey, F. Weysser and M. Fuchs (2010). "Nonlinear response of dense colloidal suspensions under oscillatory shear: Mode-coupling theory and Fourier transform rheology experiments." Physical Review E **82**(6): 061401.

Carrier, V. and G. Petekidis (2009). "Nonlinear rheology of colloidal glasses of soft thermosensitive microgel particles." J. Rheology **53**.

Cloitre, M., R. Borrega, F. Monti and L. Leibler (2003). "Glassy Dynamics and Flow Properties of Soft Colloidal Pastes." Physical Review Letters **90**(6): 068303.

Crassous, J. J., L. Casal-Dujat, M. Medebach, M. Obiols-Rabasa, R. Vincent, F. Reinhold, V. Boyko, I. Willerich, A. Menzel, C. Moitzi, B. Reck and P. Schurtenberger (2013). "Structure and Dynamics of Soft Repulsive Colloidal Suspensions in the Vicinity of the Glass Transition." Langmuir **29**(33): 10346-10359.

Crassous, J. J., M. Siebenburger, M. Ballauff, M. Drechsler, D. Hajnal, O. Henrich and M. Fuchs (2008). "Shear stresses of colloidal dispersions at the glass transition in equilibrium and in flow." The Journal of Chemical Physics **128**(20): 204902-204916.

Deike, I., M. Ballauff, N. Willenbacher and A. Weiss (2001). "Rheology of thermosensitive latex particles including the high-frequency limit." Journal of Rheology **45**(3): 709-720.

Deike, I., M. Ballauff, N. Willenbacher and A. Weiss (2001). Rheology of thermosensitive latex particles including the high-frequency limit, SOR. **45:** 709-720.

Derec, C., G. Ducouret, A. Ajdari and F. Lequeux (2003). "Aging and nonlinear rheology in suspensions of polyethylene oxide-protected silica particles." Physical Review E **67**(6): 9.

Divoux, T., C. Barentin and S. Manneville (2011). "Stress overshoot in a simple yield stress fluid: An extensive study combining rheology and velocimetry." Soft Matter **7**(19): 9335-9349.

Divoux, T., D. Tamarii, C. Barentin and S. Manneville (2010). "Transient Shear Banding in a Simple Yield Stress Fluid." Physical Review Letters **104**(20): 208301.

Ewoldt, R., P. Winter, J. Maxey and G. McKinley (2010). "Large amplitude oscillatory shear of pseudoplastic and elastoviscoplastic materials." Rheologica Acta **49**(2): 191-212.

Ferry, J. D. (1980). Viscoelastic Properties of Polymers. University of Winscosin.

Fuchs, M. and M. Ballauff (2005). "Flow curves of dense colloidal dispersions: Schematic model analysis of the shear-dependent viscosity near the colloidal glass transition." The Journal of Chemical Physics **122**(9): 094707-094706.

Fuchs, M. and M. Ballauff (2005). "Nonlinear rheology of dense colloidal dispersions: A phenomenological model and its connection to mode coupling theory." Colloids and Surfaces A: Physicochemical and Engineering Aspects **270-271**: 232-238.

Kobelev, V. and K. S. Schweizer (2005). "Strain softening, yielding, and shear thinning in glassy colloidal suspensions." Phys Rev E Stat Nonlin Soft Matter Phys **71**(2 Pt 1): 021401.

Koumakis, N., J. F. Brady and G. Petekidis (2013). "Complex Oscillatory Yielding of Model Hard-Sphere Glasses." Physical Review Letters **110**(17): 178301.

Koumakis, N., M. Laurati, S. U. Egelhaaf, J. F. Brady and G. Petekidis (2012). "Yielding of Hard-Sphere Glasses during Start-Up Shear." Physical Review Letters **108**(9): 098303.

Koumakis, N., M. Laurati, A. R. Jacob, K. J. Mutch, A. B. Abdelali, A. B. Schofield, S. U. Egelhaaf, J. F. Brady and G. Petekidis (2014). "Start-up Shear of Concentrated Colloidal Hard Spheres: Stresses, Dynamics and Structure." in preparation.

Koumakis, N., A. Pamvouxoglou, A. S. Poulos and G. Petekidis (2012). "Direct comparison of the rheology of model hard and soft particle glasses." Soft Matter **8**(15): 4271-4284.

Koumakis, N., A. B. Schofield and G. Petekidis (2008). "Effects of shear induced crystallization on the rheology and ageing of hard sphere glasses." Soft Matter **4**(10): 2008-2018.

Laurati, M., J. Stellbrink, R. Lund, L. Willner, E. Zaccarelli and D. Richter (2007). "Asymmetric poly(ethylene-alt-propylene)-poly(ethylene oxide) micelles: A system with starlike morphology and interactions." Physical Review E **76**(4).

Le Grand, A. and G. Petekidis (2008). "Effects of particle softness on the rheology and yielding of colloidal glasses." Rheologica Acta **47**(5): 579-590.

Mason, T. G., J. Bibette and D. A. Weitz (1996). "Yielding and Flow of Monodisperse Emulsions." Journal of Colloid and Interface Science **179**(2): 439-448.

Mason, T. G. and D. A. Weitz (1995). "Linear Viscoelasticity of Colloidal Hard-Sphere Suspensions near the Glass-Transition." Physical Review Letters **75**(14): 2770-2773.

Meeker, S. P., R. T. Bonnecaze and M. Cloitre (2004). "Slip and flow in pastes of soft particles: Direct observation and rheology." Journal of Rheology **48**(6): 1295-1320.

Miller, F. A. and G. B. Kauffman (1989). "C. V. Raman and the discovery of the Raman effect." Journal of Chemical Education **66**(10): 795.

Miyazaki, K., H. M. Wyss, D. A. Weitz and D. R. Reichman (2006). "Nonlinear viscoelasticity of metastable complex fluids." Europhysics Letters **75**(6): 915-921.

Mours, M. and H. H. Winter (1996). "Relaxation patterns of nearly critical gels." Macromolecules **29**(22): 7221-7229.

Ohno, K., T. Morinaga, S. Takeno, Y. Tsujii and T. Fukuda (2006). Suspensions of Silica Particles Grafted with Concentrated Polymer Brush: A New Family of Colloidal Crystals. **39:** 1245-1249.

Ohno, K., T. Morinaga, S. Takeno, Y. Tsujii and T. Fukuda (2007). "Suspensions of Silica Particles Grafted with Concentrated Polymer Brush: Effects of Graft Chain Length on Brush Layer Thickness and Colloidal Crystallization." Macromolecules **40**(25): 9143-9150.

Ozon, F., G. Petekidis and D. Vlassopoulos (2006). "Signatures of nonergodicity transition in a soft colloidal system." Industrial & Engineering Chemistry Research **45**(21): 6946-6952.

Paulin, S. E., B. J. Ackerson and M. S. Wolfe (1996). "Equilibrium and shear induced nonequilibrium phase behavior of PMMA microgel spheres." Journal of Colloid and Interface Science **178**(1): 251-262.

Petekidis, G., J. Gapinski, P. Seymour, J. S. van Duijneveldt, D. Vlassopoulos and G. Fytas (2004). "Dynamics of core-shell particles in concentrated suspensions." Physical Review E **69**(4).

Petekidis, G., D. Vlassopoulos and P. N. Pusey (2003). "Yielding and flow of colloidal glasses." Faraday Discuss: 287-302.

Petekidis, G., D. Vlassopoulos and P. N. Pusey (2004). Yielding and flow of sheared colloidal glasses.

Poulos, A., J. Stellbrink and G. Petekidis (2013). "Flow of concentrated solutions of starlike micelles under large-amplitude oscillatory shear." Rheologica Acta **52**(8-9): 785-800.

Rao, R. B., V. L. Kobelev, Q. Li, J. A. Lewis and K. S. Schweizer (2006). Nonlinear Elasticity and Yielding of Nanoparticle Glasses. **22:** 2441-2443.

Renou, F., J. Stellbrink and G. Petekidis (2010). "Yielding processes in a colloidal glass of soft star-like micelles under large amplitude oscillatory shear (LAOS)." Journal of Rheology **54**(6): 1219-1242.

Rogers, S. A., B. M. Erwin, D. Vlassopoulos and M. Cloitre (2011). "Oscillatory yielding of a colloidal star glass." Journal of Rheology (1978-present) **55**(4): 733-752.

Rogers, S. A., B. M. Erwin, D. Vlassopoulos and M. Cloitre (2011). "A sequence of physical processes determined and quantified in LAOS: Application to a yield stress fluid." Journal of Rheology (1978-present) **55**(2): 435-458.

Romeo, G., L. Imperiali, J.-W. Kim, A. Fernández-Nieves and D. A. Weitz (2012). "Origin of de-swelling and dynamics of dense ionic microgel suspensions." The Journal of Chemical Physics **136**(12): -.

Segre, P. N., O. P. Behrend and P. N. Pusey (1995). "Short-time Brownian motion in colloidal suspensions: Experiment and simulation." Physical Review E **52**(5): 5070-5083.

Senff, H., W. Richtering, C. Norhausen, A. Weiss and M. Ballauff (1998). "Rheology of a Temperature Sensitive Core-Shell Latex." Langmuir **15**(1): 102-106.

Senff, H., W. Richtering, C. Norhausen, A. Weiss and M. Ballauff (1999). Rheology of a Temperature Sensitive Core-Shell Latex. **15:** 102-106.

Seth, J. R., L. Mohan, C. Locatelli-Champagne, M. Cloitre and R. T. Bonnecaze (2011). "A micromechanical model to predict the flow of soft particle glasses." Nature Materials **10**(11): 838-843.

Siebenburger, M., M. Fuchs, H. Winter and M. Ballauff (2009). "Viscoelasticity and shear flow of concentrated, noncrystallizing colloidal suspensions: Comparison with mode-coupling theory." Journal of Rheology **53**(3): 707-726.

Sollich, P. (1998). "Rheological constitutive equation for a model of soft glassy materials." Physical Review E **58**(1): 738-759.

Sollich, P., F. Lequeux, P. Hébraud and M. E. Cates (1997). "Rheology of Soft Glassy Materials." <u>Physical Review Letters</u> **78**(10): 2020-2023.

Stieger, M., J. S. Pedersen, P. Lindner and W. Richtering (2004). "Are thermoresponsive microgels model systems for concentrated colloidal suspensions? A rheology and small-angle neutron scattering study." <u>Langmuir</u> **20**(17): 7283-7292.

Tanaka, M. and R. J. Young (2006). "Review Polarised Raman spectroscopy for the study of molecular orientation distributions in polymers." <u>Journal of Materials Science</u> **41**(3): 963-991.

Vlassopoulos, D., G. Fytas, T. Pakula and J. Roovers (2001). "Multiarm star polymers dynamics." <u>J. Phys. : Condens. Matter</u> **13**: R855-R876.

General Conclusions and Future Work

Part 1: Laser-induced pattern formation in polydiene solutions

Conclusions:

Micro-Raman spectroscopy experiments of the irradiated samples have evidenced a series of chemical modifications between the material before and after irradiation. Swelling and Rheology experiments revealed a gel-like structure in the written material, which is due to cross-linking of the material. The relatively low swelling observed (40% polymer concentration) indicates a rather large crosslinks density, that can be estimated of the order of 20% or more, EPR spectroscopy detects a small number of long lived free radicals that are probably not directly involved in the chemical modification observed by Raman spectroscopy. The cross-linking needed (order of 10 percent, i.e 100 more than the detection threshold of EPR) to create the insoluble but swellable extracted material is expected to happen on a fast rate which makes it "invisible" by EPR (as it is the case in most photo-chemical processes). Observation of long-lived radicals does not exclude the presence of short lived ones that react to create the needed crosslinked. Moreover the observation of the free radicals when light is turned on is a proof of some type of light induced formation of radicals, and a hint in the direction of photo-induced chemistry. How direct the light action is on the chemical bonds remains to be clarified. But clearly a chemical process is at work, caused (more or less directly) by the red laser irradiation. In the second chapter I have reported of different experiments with different type of materials in order to further explore the offered possibilities and with the hope of identifying the necessary conditions for the different types

of patterning. The main results were, that antioxidant does not have much effect on the patterning, somewhat ruling out the importance of straight oxidation. Crosslinked networks were shown to be responsive to the light irradiation in a very similar way to the non crosslinked solution, therefore clearly indication the "locality" of the modification. The use of styrene containing co-polymers allowed extending the domain of "active" active materials. The co-polymeric nature allowed to dissolve n solvent where the pure polydiene are not soluble. SBR and SIS solutions were found to respond positively for hexane and negatively for ethyl acetate. SIS showed a spectacular case of patterning with induced transparency.

Outlook :

Despite progress, the precise light-dienes coupling remains elusive. Real time spectroscopy will probably prove helpful to establish the time scale of the chemical reaction. One such possibility is Raman scattering where the red beam used to as the "writing" source of light for the Raman scattering experiments. The self-guiding will help to gat mostly light from the written material. The specificity of the red light and the occurrence need to be further clarify Besides the special case of dienes based polymer in solution, this work may help to design novel type of light responsive material based on polymer solutions,. The change of refractive index will then relate to a change of concentration following a chemical or configurational change induced by light. Such systems have barely been studied, though there respond might be larger than bulk system like photorefractive resins and polymers.

Future Work:

So far we were not able to apply time resolved spectroscopy that will allow to follow the chemical changes and to correlate them with the refractive index changes, to establish

unequivocally the relation between the two. Real time µ-Raman should be our best hope to elucidate possible changes in-vivo and correlate with the formed pattern.

Moreover, an additional study of the pattern formation to more complex systems will give us the possibility to have a huge playground due to rich phase diagram they exhibit at different solvents and temperatures. Furthermore the effect of temperature to the pattern formation is of great interest. Preliminary results show that upon increasing temperature the kinetic of formation decreases, probably due to the increase of the mobility.

Part 2: Structure and dynamics in suspensions and glasses of soft colloids

Conclusions:

The effect of the particle's softness of soft colloidal particles in the liquid and glass regime were studied by light scattering and rheology. Here three soft core-shell particles with the same core size and surface density but different molecular weights (M_w=41kg/mol (**P2_41k**), M_w=126kg/mol (**P2_126k**) and M_w=402kg/mol (**P2_402k**)) of the attached polymer chain was used. The volume fraction was calculated in terms of the overlap concentration $c^*(R_H)$, with R_H being the hydrodynamic radius of the individual particle.

Structure and dynamics in concentrated suspensions were investigated through 3D dynamic light scattering experiments. We observed a rich phase diagram similar but wider compared to hard spheres. The structure properties show deviations from hard spheres, denoting the soft particle character. Specifically for the larger and softer P2_402k we observed a non-monotonic behaviour in the amplitude of S(Q) , evidence of particle retraction and possibly shrinkage of individual particles. The particles have long-range

repulsive interactions with Ξ/D_H to be 1.13 for the concentrations close to liquid-crystal coexistence. For the dynamic properties, the theory for permeable spheres seems to be the best candidate to describe the volume fraction dependence. By changing one parameter, the hydrodynamic penetration depth x, we were able to fit self-diffusion and cage (structural) diffusion as a function of the effective volume fraction. The packing fraction extracted from the limit of $D(Q_{min}) \rightarrow 0$ increases as we increase particle softness. For the intermediate particle (P2_126k) the apparent random packing is close to hard sphere one (c/c*(RCP)~0.67) and becomes 1.2 for P2_402k in toluene.

By further increasing the volume fraction, moving to the glass state, the system become strongly non-ergodic and ageing phenomena were observed. We have presented a clear experimental evidence for the crystallization of soft core-shell particles at highly concentrated glassy suspensions after long time. Despite the strong difference in the softness and the lack of observation of a liquid-crystal transition at lower volume fractions (through observation tests and rheology) for the smaller and harder particle (P2_41k), both systems showed a clear glass-crystal re-entrant transition. Crystallization occurred through a progressively ordering of the particles in the glassy state. The speed-up of the dynamics is due to increase of the local free volume that the system gains in crystal phase, where the particles may diffuse easier at local length-scales. At even higher volume fractions the system remained trapped in the metastable glassy state due to strong residual stresses and interpenetration.

The effect of the particle's softness of the mechanical properties of soft colloidal particles in the glassy state were studied in both the linear and nonlinear regime. Dynamic frequency sweep tests (DFS) showed a typical glassy behaviour with G'>G" at all frequencies and with G' being independent of frequency at all volume fractions and measured systems. From the plateau modulus, G' vs c/c* for the three systems was used to determine the interparticle potential, which is linked to particle softness. For all the systems studied, a similar slope was revealed, at intermediate c/c* around 22, with the slope to decreasing with increasing volume fraction due to interpenetration. Apart from the interparticle potential, the transition from α to β relaxation was deduced from the G" minimum. For the harder particle (P2_41k), two transitions where observed: one at c/c*~1 possibly related to the random close packing or jamming transition where the particles are no longer able to

move, reminiscent of hard sphere behaviour around the glass transition (φ=0.58) and one at higher volume fractions (c/c*~1.1) where possible linked to stronger particle interpenetration (or shrinkage). Similar behavior was observed also for P2_126k, with a jamming transition at c/c*=1.3, significantly higher than for 41k due to softer particle character. For the larger and softer particle (P2_402k) t_{min} is constant and then speeds-up as we continue to increase c/c*. The constant t_{min} with c/c* is related to cancelation of effects from particles' shrinkage, increased confinement and interpenetration.

From dynamic strain sweep experiments (DSS), one can measure the yield strain, $γ_y$, the strain which above the sample starts exhibit a liquid-like behavior, although not necessarily that of a simple Newtonian fluid. For the smaller and harder particle at 0.1 rad/s, $γ_y$ shows non-monotonic behavior with c/c* due to decreasing of the free volume per particle as random close packing is approached, similar to what has been detected for hard spheres. At higher frequencies $γ_y$ decreases with increasing c/c* due to particle colliding and cage breaking. For the intermediate particle, P2_126k, the behavior is similar with $γ_y$ exhibit a decreasing with c/c* for the same reason. The larger and softer particle exhibit a concentration and frequency independent $γ_y$, due to strong interpenetration they exhibit at this high volume fractions (c/c* > 1.3).

We also discussed the effect of steady shear in all three systems. In all cases a characteristic yield stress plateau was revealed at high volume fractions, indicative of the systems in the glass regime. We used a Hershel-Bulkley model to fit our data and extract the yield stress plateau value $σ_y$ and the exponent v at high rates. By using the model proposed by Cloitre et al. (Seth, Mohan et al. 2011) we attempted to superimpose our data in a universal curve. For P2_41k all data superimposed quite well in a master curve with the slope of the stress at high rates being about 0.5, similar to what has been predicted for soft microgels. By increasing the softness, however, moving to P2_126k and P2_402k, the model failed to predict a universal fit of the data, with the slope at high rates being around or higher than 0.7. The transition from Concentrated Polymer Brush (CPB) to Semi-Dilute Polymer Brush (SDPB) might play a role.

In transient tests, start-up experiments together with stress relaxation tests were performed. For the smaller and harder particle (P2_41k) start-up tests show an oscillating increase of the stress in all volume fractions and shear rates. Possible explanation is the

appearance of transient shear banding while wall slip was eliminated. The critical strain extracted from the stress at the peak shows a Peclet and volume fraction dependence similar to hard spheres. The residual stress $\sigma_{residual}$ measured with stress relaxation tests performed after start-up, show an almost linear decrease of the frozen stress with Peclet as well as a decrease with decreasing c/c*. The softer character of P2_126k was revealed from the lack of volume fraction dependence of the critical strain as a function of Pe, similar to observations in other soft systems. Similarly, in the case of the larger particles (P2_402k) both the critical yield strain and the amplitude of the stress overshoot show no volume fraction dependence. Additionally the residual stresses $\sigma_{residual}$ are also c/c* independent due to the strong interpenetration they exhibit at this high volume fractions. This is similar with P2_41k at the two highest volume fractions where $\sigma_{residual}$ is c/c* independent.

Future Work:

The study of the soft core-shell particles in the liquid regime could be continued towards understanding of the dynamics and especially the self-diffusion coefficient near the wall. It has been found that the dynamics of hard sphere particles slows down depending on the particle-wall distance. The effect of softness and solvent permeability is an additional parameter which will change dramatically the dynamics near the wall. Moving one step further the addition of small polymer chains attached on the wall will create an additional force, which depending on the chain molecular weight and grafting density could be attractive or repulsive.

In the glass regime, additional experiments should be performed in both systems in order to be able to determine D(Q) vs Q during aging and especially close to the re-entrant transition and investigate possible change of the slope D(Q) vs Q , which will reflect a different diffusion mechanism.

It would be very interested also to investigate how the single particle dynamics in such systems are affected by shear and what is the role of particle's softness. Light scattering echo (LS-echo) technique could give as the opportunity to elucidate the effect of

strain on the dynamics of the system. Moreover it will be very interesting to perform small angle light scattering experiments together with rheology (Rheo-SALS) to check the change of the scattering pattern upon shear and to extract information of the shear profile. Furthermore it would be interesting to investigate shear-induced ordering, at different concentrations and as a function of particle softness.